Yearbook

2017

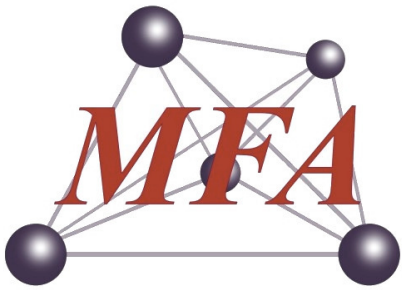

Institute of Technical Physics and Materials Science

http://www.mfa.kfki.hu/

Hungarian Academy of Sciences
Centre for Energy Research

Institute of Technical Physics and Materials Science

MTA EK MFA Yearbook 2017

Director: Prof. Béla Pécz

Address: Konkoly-Thege Miklós út 29-33,
H-1121 Budapest, Hungary
Postal: P.O.Box 49, H-1525 Budapest, Hungary
Phone: +36-1-392 2225
Fax: +36-1-392 2226
E-mail: info@mfa.kfki.hu
URL: http://www.mfa.kfki.hu/

Editor: Csaba S. Daróczi
Published by: MTA EK MFA, Budapest, Hungary, 2018

CONTENT

Content 3
Director's Foreword 5
General Information 7
Organization of MFA 7
Key Financial Figures of MFA 8
Publications and Citations of MFA 9
Prizes and distinctions 10
Highlights 12
Force feedback and tactile sensing for Robin Heart Surgical Robot 12
Corrosion resistance of nano-sized SiC-rich composite coatings produced by // 15
Events 17
Scientific Reports 19
Nanostructures Laboratory & 2D 'Lendület' Research Group 20
Catalytically active single oxygen sites in the basal plane of 2D MoS_2 crystals 21
Observation of large band gap modification in single-layer MoS_2 due to // 23
Interaction effects in a chaotic graphene quantum billiard 25
Atomic scale electronic properties of single layer $MoSe_2$ crystals grown on // 27
Novel graphene/Sn and graphene/SnO_x hybrid nanostructures: band gaps // 29
Changes in structural and pigmentary colours in response to cold stress // 31
Photonics Department 33
Detecting patchy nanoparticle assembly at the single-particle level 33
Magnetic flux simulation for the inspection of local thinning of ferromagnetic // 36
Development of optical metrology tool for in-line qualification thin films on // 38
Fabrication of Genetically Modified Bacterial Filament Coatings to Develop // 40
Investigation of wetting processes by the capillary bridge probe technique 41
Optical and structural characteriyation of Ge clusters embedded in ZrO_2 43
Ellipsometric and X-ray spectrometric investigation of fibrinogen protein layers 45
Vegard's-law-like dependence of the activation energy for blistering on the Si/Ge // 46
Porous Si degradation in physiological solution 47
Microtechnology Department 48
MEMS 51
Development of micro gas sensors 51
Conductivity type sensors for NH_3 and H_2S 53
Development and production of Near Infrared LEDs 54
BioMEMS 54
Polymer microfluidic systems for medical diagnostics 54
Characterisation of blood protein adsorption on modified PDMS surfaces 55
Fabrication of hybrid microfluidic system on transparent substrates 56
Cell and particle manipulation and screening in microfluidic systems 57
Modelling and characterisation of cell and molecule advection in // 57
Particle separation and trapping in micromagnetic separation (MMS) systems 58
Droplet generation and trapping for cell analytical two-phase microfluidic system 59
Concentration gradient generation for cell population analysis 60
SERS active periodic 3D structure for trapping and high sensitive // 61
Intelligent wound patch for online monitoring wound healing processes // 62
Precisely controlled Focused Ion Beam milling of solid state nanopore // 63

NEMS 64
Piezoelectric Nanowire Arrays for High Resolution Tactile Mapping 65
Spiral-Shaped Piezoelectric MEMS Cantilever Array for Fully Implantable // 69
Vibrational energy harvester powered sensor node 71
Thin Film Physics Department 73
TEM study of the as-deposited and annealed Ga_2O_3 films grown by // 74
Phase formation sequence in the Ti/InP system during thin film // 77
Effect of deposition parameters on cubic TiC and hexagonal Ti formation // 79
Structure and mechanical properties of hard yet fracture resistant W-B-C coatings // . 80
Dot patterning of CoPt films by RF plasma etching for high capacity // 82
Formation and properties of self-forming diffusion barrier layers 83
TEM study of nickel and copper silicides 84
Characterization of defect structure, mechanical properties and stability of // 85
New type functional alloy films 86
Graphene-ceramic composites for tribological application in aqueous // 87
New approaches in the development of Hypoallergenic implant material in // 89
Investigation of Biocompatible Glasses for Biomedical Applications 89
Development and characterization of multi-element doped hydroxyapatite // 91
Development of protective TiC/a:C thin films prepared by DC magnetron // 92
Effect of oxidization of Si_3N_4 particles on structure of sintered Si_3N_4 ceramics 94
Advanced ceramic and their composits for energy application 95
Effect of Si_3N_4 addition on the morphological and structural properties of the // 96
Adhesion model of graphene islands on metal substrates based on Moiré // 97
One-sample combinatory for high throughput TEM- and other analytical studies // . 100
Nanobiosensorics Group 102
Biophysical characteristics of proteins and living cells exposed to the green // 103
Green tea polyphenol tailors cell adhesivity of RGD displaying surfaces // 104
Label-free optical biosensor for on-line monitoring the integrated response // 106
Fabrication and characterization of ultrathin and spin-coated (thick) dextran // 108
Bacteria repellent layer made of flagellin 110
Receptor specific adhesion assay for the quantification of integrin–ligand // 111
Antibiotic-Induced Release of Small Extracellular Vesicles (Exosomes) // 113
Complex Systems Department 115
Effects of Heterogeneity in Power-Grid Network Models 116
Second-order freeriding on antisocial punishment restores the effectiveness of // 117
Study of the effect of prehistoric Human migration processes to the recent // 119
MFA Publications in 2017 121

DIRECTOR'S FOREWORD

As the director of MFA, it is my pleasure to welcome the reader. I recommend browsing the present yearbook which continues the series of the former ones and contains results achieved in 2017.

2017 was an extremely successful year for MFA from the point of projects gained and infrastructure renewed. Also the results of our colleagues were appreciated by different authorities and prize committees. However, we faced a strong 'brain drain' by the industry, which led to a situation that some of the Ph.D. students did not even finish their Ph.D., just changed for a job at some industries. This is completely new in our institute. The increasing load need of the industry coincides with the fact that the academic starting salaries are very low thus led to a situation in which the number of applicants for a Ph.D. position has decreased. As a director, I do my best to call the attention of the Academy of Sciences for this very serious problem. I am sure that our Academy should and could improve that situation with the help of the government.

In 2017, the most honourable event was the successful organization of the 15th Conference & Exhibition of the European Ceramic Society (ECerS2017) by co-workers of the institute. Inside the top organization board there were two colleagues, *Dr. Cs. Balázsi* and *Dr. K. Balázsi* as chair and co-chair. Number of participants was about 800, there were even two satellite courses organised in our research centre, one of them exactly in MFA.

We are extremely proud on numerous groups headed by young contemporaries, many of them honoured by financing agencies. One of such financed "Lendület" ("Momentum") research group was the Novel 2D materials group led by *Dr. Levente Tapasztó* (also running an ERC Starting Grant NanoFab2D), which got to the end of the contract period and, accordingly, was subjected to an official audit. In that procedure, the group has received "Outstanding" qualification from the Academy of Sciences, which also meant that the previous extra support became part of the institute's annual subvention. Another excellent young researcher, *Dr. Péter Nemes-*Incze returned from Germany applied for a "Lendület" project and his application was also awarded by the Academy of Sciences. He made the first steps in 2017 in order to form a new research group for Topological Nanostructures. Both of the above groups made successful investment into new equipment, namely, a high-vacuum, low-temperature STM arrived at the Nanostructures Laboratory.

The Institute works under the Quality assurance system ISO 9001: 2008. In this system, scientific publications are considered as products. Therefore, we make a sum-up of them each year. Fortunately, the scientific level of MFA's publications/impact has increased again and the researchers receive more and more independent citations year by year. I would like to congratulate here our colleague *Dr. Attila Szolnoki*, who

achieved the record number of independent citations in 2017 actually over 1200 citations. Cooperation with industrial partners has a growing importance in the life of MFA. Our researchers participated actively in development of robotic minimal invasive surgery tool by their tactile sensors and finished the ECSEL INCITE project with great success. We also participate actively in R&D processes with the participation of Hungarian industrial firms. MFA clearly wants to show that the research conducted by the institute also benefits for the society. Therefore, each year we organise an Open Day, when everyone can take a personal visit to the institute and listen talks on the latest activity and even visit some laboratories. MFA organises scientific seminar talks weekly and those lectures are also open to the public. We are proud for the one-week summer school for high-school students, when they also get a chance to work inside our laboratories. It is our mission to help them and orient them when they choose subjects for their university studies.

Renewal of our infrastructure ran successfully in 2017 as well. A new project in order to purchase a four-tube diffusion furnace for the clean room of our Microtechnology Department was awarded by NKFIH (National Research, Development and Innovation Office) and by the Ministry of National Economy. The complicated public tendering procedure is in progress. Another investment for a new dual beam (FIB+SEM) system is also in the tendering phase and will be covered by similar support of our ministry.

The tender for a new sputtering unit was already successfully carried out and the contract is signed. A large research project on renewable energy started in a consortium in the second half of 2017.

I congratulate to my colleagues: *Dr. Gábor Battistig*, was awarded by the Knight's Cross of Order of Merit of Hungary. *Dr. Zoltán Juhász* received the Hungarian Heritage Award. Very exceptionally 2017 was the second year in a row when the Physics Grand Prize of the Hungarian Academy of Sciences went to our institute, now to our *Dr. Attila Szolnoki*. *Dr. Gábor Battistig* and *Dr. Zsolt Endre Horváth* defended their Thesis for the Doctor of Academy (D.Sc.) title. We are also proud of those five Ph.D. students, who were supervised by colleagues at MFA and defended their thesis successfully in 2017 and got the Ph.D. degree from different universities. *Dr. Levente Tapasztó* became member of European Academy of Sciences and Arts, while *Dr. József Gyulai* (one of our former directors) was elected as member of Academia Europaea; both we also consider as a distinction for our institute.

I hope that the Readers of this yearbook will find further interesting details on the following pages. Here I note that the former MFA Yearbooks are available electronically at http://www.mfa.kfki.hu/hu/yearbook/

Budapest, April 10st, 2017

Dr. Béla Pécz, D.Sc., Director

GENERAL INFORMATION

Organization of MFA

Director	- ***Béla PÉCZ***

Scientific Departments	
Nanostructures Department	- *Levente TAPASZTÓ*
"Lendület" group - 2D Materials	- *Levente TAPASZTÓ*
"Lendület" group - Topological Nanostructures	- *Péter NEMES-INCZE*
Thin Film Physics Department	- *Katalin BALÁZSI*
Complex Systems Department	- *György SZABÓ*
Photonics Department	- *Péter PETRIK*
Microtechnology Department	- *Gábor BATTISTIG*
"Lendület" group - NanoBioSensorics	- *Róbert HORVÁTH*

Directly supervised functions	
Head of Scientific Advisory Council	- *János LÁBÁR*
Scientific secretary, projects and PR	- *Krisztina SZAKOLCZAI*
Quality control, MTMT, REAL admin	- *Andrea BOLGÁR*
Technical support	- *Károly BODNÁR*
Financial administration	- *Zsuzsa KELEMEN*
Informatics	- *Gergely TAMÁS*
Technology transfer (IPR)	- *Antal GASPARICS*

Key Financial Figures of MFA

The turnover realised by the institute (and in general by the members of the Hungarian academic research network) always reflect the national and international political and financial system. The domestic subsidies did not change in the last few years. There is a certain periodicity in the income of the institute based on the changes by the domestic grant management system, and also by the European Commission's research schemes (FP6, FP7 and now H2020). In late 2016 the Hungarian Ministry of Economics and also the National Office for Research and Development restarted the R&D programs aiming mainly the structural, investment and application based grants. It resulted in several large new infrastructure projects starting in 2017, in which our institute gained its share for material and sensor research.

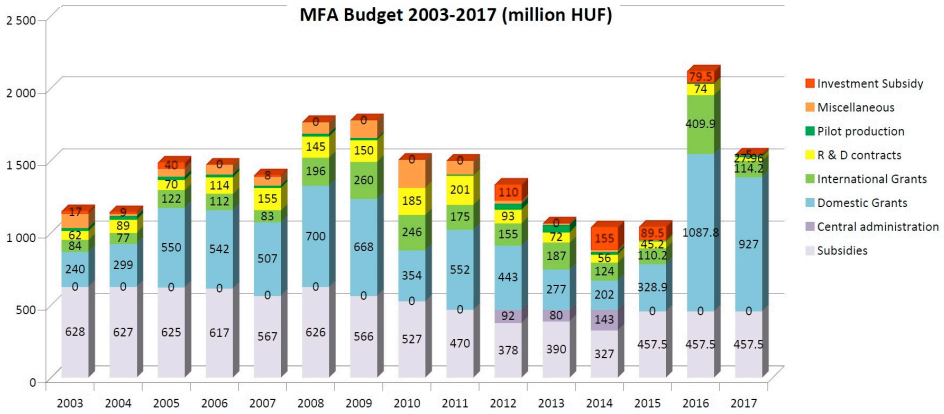

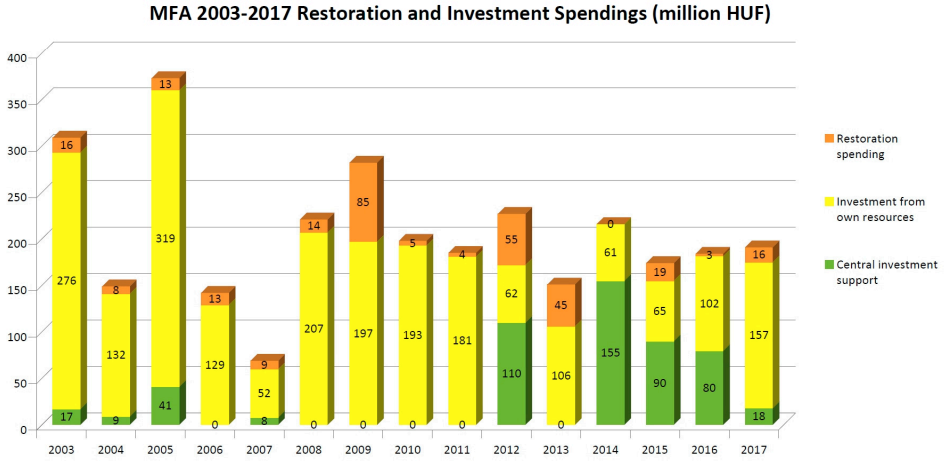

Since 2015 MFA is part of the Centre of Energy Research. Financial issues regarding our grants started in the Research Centre for Natural Science, following our reorganization were not closed, not till the beginning of 2018!
Although part of the financial data is now accessible via the Academy's reporting system (Köpeny) our operation is still not transparent, our financial status completely not plannable, totally unpredictable by our own grant administration group. We still do not have access to authentic budget and accounting; all the data for 2015-2017 are based upon our own estimates.
Despite all these, we can call 2017 a successful year. Scientific achievements were granted with new financial sources both from national and international authorities. By the end of the year our income reached the high value of 1.6 billion HUF. But the values can be misleading, part of the income in 2016 and in 2017 results from 3-4 years grants recieving all their financial support at the beginning of the project.

Publications and Citations of MFA

According to the Thomson-Reuters ISI "Web of Knowledge", and MTMT databases, the Institute has an average publication activity of ca. 100 scientific papers in IF journals a year. It seems however, that in 2017 our researchers published a little bit lower number of papers in journals with higher impact factor.

MFA and its predecessor's publications

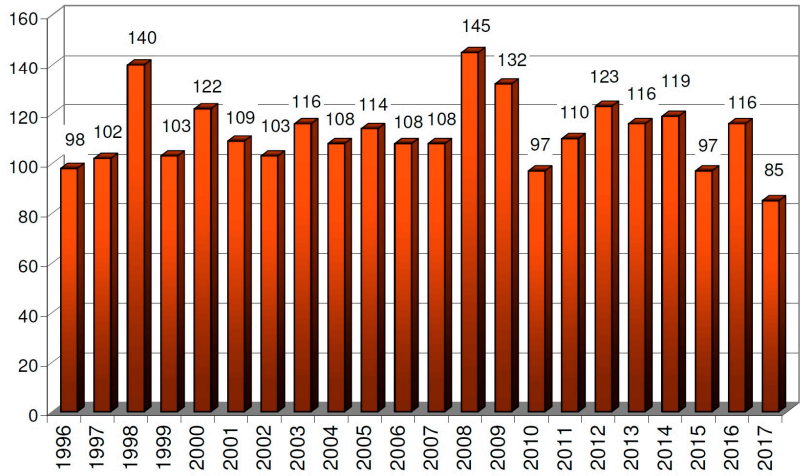

The complete 2017 publication list of MFA – with considerably more titles than listed by the ISI Web of Science and MTMT – is included at the end of this yearbook. A good measure of recognition of MFA's scientific activity is the h-index of 81.

MFA and its predecessor's citations

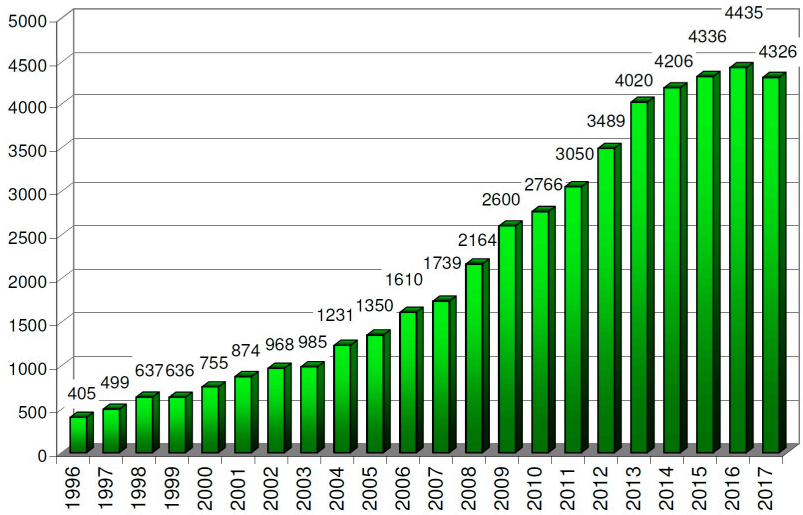

Prizes and Distinctions

BATTISTIG, Gábor — Knight's Cross of Order of Merit of Hungary

SZOLNOKI, Attila — Physics Grand prize of the Hungarian Academy of Sciences

JUHÁSZ, Zoltán — Hungarian Heritage Award

BALÁZSI, Katalin — Zoltán Gyulai Award

SZOLNOKI, Attila

Recognition for reviewer from Royal Society
Outstanding Reviewer from New J. Phys. IOP EPL
"Highlights 2016" -A compilation of the best papers published within the last year"

PÁLINKÁS, András

European Materials Research Society Young Scientist Award

MTA EK Young scientist prize

GERGELY, György

Ruby diploma (honorary diploma after 70 years of graduation) of the Technical University of Budapest

VANCSÓ, Péter

Academia Europaea Burgen Scholar Excellence Award

CORA, Ildikó

MFA Prize (Postdoctoral)

TAPASZTÓ, Orsolya

MFA Prize (Postdoctoral)

PISZTER, Gábor

MFA Prize (Ph.D. student)

BÍRÓ, Ferenc

MFA Prize (Ph.D. student)

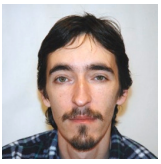

NAGY, Attila

MFA Prize (Excellent science support)

HIGHLIGHTS

Force feedback and tactile sensing for Robin Heart Surgical Robot

(Intelligent Catheters in Advanced Systems for Interventions, ENIAC INCITE 621278, NEMZ_12-1-2014-0005)

J. Radó, Cs. Dücső, P. Földesy, Kamil Rohr, Z. Nawrat, and P. Fürjes

Minimally invasive robotic surgery (MIS) offers several advantages for the patients, although the lack of sensory feedback for the surgeon is one of the main barriers in its progress and widespread application. Gathering immediate multi-parametric information about the physical and anatomic conditions of tissues is crucial for the operator to precisely control the robotic actions. “Smart” laparoscopes with integrated MEMS sensors can provide such feedback and to improve the safety of these interventions.
Our goal was to develop a novel smart laparoscope for surgery robots with integrated 3D force sensors inside the grasper and also on the tip of the device to measure the gripping strength and to provide tactile information about the different organs and tissues touched.

Force sensor chips for force feedback and tactile sensing applications

Piezo-resistive transduction principle is used to design and fabricate the 3D force chips. Accordingly, the piezoresistors were formed in the device layer of the SOI substrate wafer by ion implantations. Deformable membranes were formed by DRIE (deep reactive ion etching) process to minimize the lateral size of the chips. The SOI wafers provide uniform membrane thickness over the whole wafer. Anodic wafer bonding was applied to integrate the active Si to borosilicate glass for parallel formation of rigid substrate and ohmic contact between piezo-resistors embedded in the Si element and wire bonding pads on boron glass. The fabricated force sensor chips are shown in Fig. 1.

Electro-mechanical and system level integration

Two 3D MEMS force sensors were integrated in the laparoscopic head on a flex-PCB with dedicated preamplifiers and ADCs forming the pre-processing electronic circuitry. One sensor chip is on the tip of the lower jaw of the tweezers and the other one is inside the same element. The electrical connections were produced by wire bonding according to the architecture of the silicon-glass bonded structure. The MEMS force and tactile sensors were embedded in flexible polymer covering to ensure adequate mechanical stability and provide reliable force/load transfer to the silicon membrane. Fig. 2. shows the packaged sensor array on the flexible PCB.

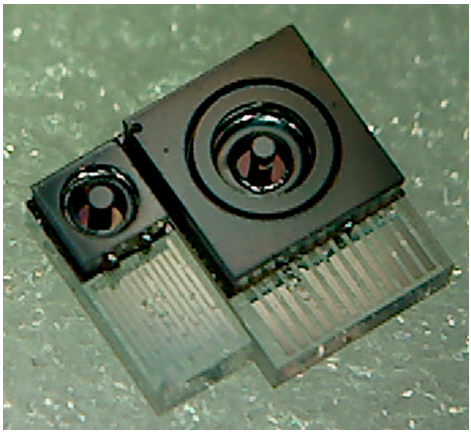

Figure 1 *Individual force sensor chips: 1×2.5mm^2 chips for head mounted tactile sensing (left) and 2×3mm^2 for gripping force detection (right).*

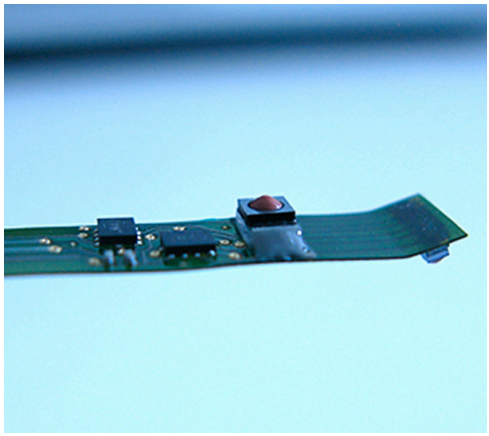

Figure 2 *The flexible PCB with the packaged sensor array containing the tip mounted tactile sensor and the force sensor dedicated for force feedback measurement inside the laparoscope tweezers.*

The laparoscope prototypes were printed by direct metal LASER sintering (DMLS) from EOS Stainless Steel GP1 medical grade stainless steel. For demonstration and to check the quality of the cast coverage, transparent silicone was used, whereas in the final prototypes black, medical grade colorant masterbatch was mixed in silicone to eliminate the effect of light on the noise, stability and accuracy of the piezoresistors in the MEMS chips.

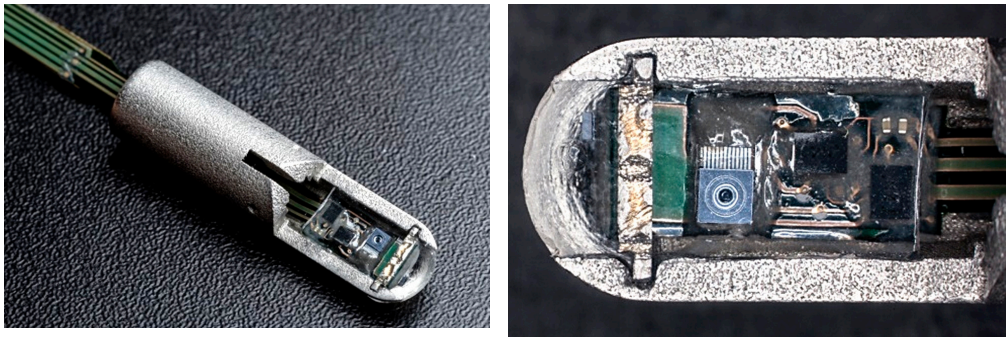

Figure 3 *The medical grade stainless steel laparoscopic tweezers with the integrated electronics covered in the (transparent) flexible biocompatible elastomer.*

The developed MIS tool was mounted on the robotic arm, and the robot control as well as the sensing capability were analysed using the force feedback. The fabricated stainless steel tweezers were integrated into the mechatronic system of the proposed smart laparoscope tool. The full functional laparoscopes are capable to drive the

tweezers by motor and transfer the electronic signals from the signal processing electronics to the I2C-CAN communication board.

RobinHeart Minimal Invasive Surgery robot with force / tactile feedback

The laparoscope was fixed on the arm of the ROBIN HEART surgery robot and connected to the manipulator via CAN BUS communication. Preliminary tests were accomplished to evaluate the force and tactile signals of the integrated sensors during interventions. The information was successfully applied to provide haptic feedback for the operator by a specific controller (Fig. 4). In the preliminary test the signals of both sensors were utilized to control the movement of the arm and the jaw of the gripper. When the laparoscope touches a surface and the emerging force in the tip tactile sensor reaches a pre-set value, an actuation routine stops the forward movement, regardless the actions of the operator with the manipulator head (Fig. 4.) Tactile measurements were also implemented on artificial and real animal tissues to prove the applicability of the device for biomechanical screening during MIS surgery.

Figure 4 *„Smart laparoscopes" integrated in the ROBIN HEART surgery robot systems.*

Summary

In this work the project partners demonstrated the design and manufacturing of the MEMS force sensors, the near-chip signal pre-processing and digital communication electronics, reliable electrical and mechanical packaging of all components and mainly the functional validation of the integrated sensor array system. The functionality of the electronics components were validated and the whole laparoscope mounted sensor system (including the electronics) was integrated with the robot control systems. By integration of this "smart" tool into the surgery robot system an advanced human-machine synergy was demonstrated applying two-directional haptic control. The first demonstration of force feedback in ROBIN HEART robotic surgery system was successfully achieved.

Corrosion resistance of nano-sized SiC-rich composite coatings produced by noble gas ion mixing [108]

A.S. Rácz, Zs. Kerner, A. Németh, P. Panjan, L. Péter, A. Sulyok, G. Vértesy, Zs. Zolnai, and M. Menyhárd

Silicon carbide (SiC) is a material that has attracted considerable interest for a long time, particularly due to its high temperature strength, thermal shock resistance, good thermal conductivity and its inertness to exposure in corrosive environments. In thin film form SiC is used in micro/nano-electromechanical system (M/NEMS) which are operating in harsh-environments e.g. automotive and aerospace applications such combustion processes or gas turbine control. Different methods can be used for producing SiC thin films e.g.: physical and chemical vapour deposition. However these methods need elevated temperature which might be disadvantageous by certain substrates. Ion beam mixing might also be used to overcome the high activation barrier of the compound formation since it creates far from equilibrium conditions, where the apparent activation barrier might be much lower.

We have applied noble gas Ar^+ and Xe^+ ion irradiation on different C/Si/C/Si/C/Si (substrate) multilayer structures (with individual layer thicknesses falling in the range of 10-20 nm). The irradiation took place at room temperature in the energy and fluence ranges of 40-120 keV and 1-6x10^{16} ion/cm^2, respectively. The effects of ion irradiation including the in-depth distribution of the SiC produced was determined by AES depth profiling. The thickness of the SiC-rich region was only some nanometers and it could be tailored by changing the layer structure and/or the ion irradiation conditions.

Fig. 1 presents the effect of the ion irradiation process on a 6x10^{16} Ar^+/cm^2, 40 keV irradiated sample.

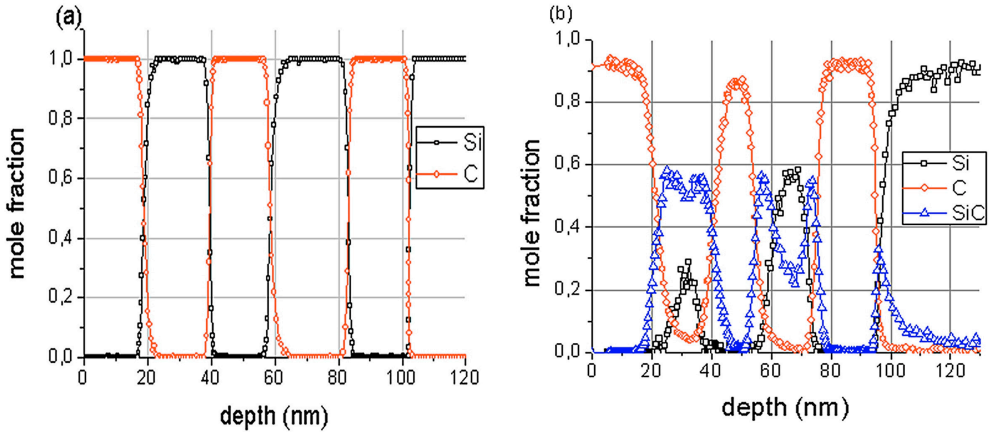

Figure 1 *AES depth profiles of the* ***(a)*** *pristine, and* ***(b)*** *irradiated (6x10^{16} Ar^+/cm^2, 40keV).*

An AES depth profile is also shown of a non-irradiated sample as a comparison (Fig. 1a). In this case all initial interfaces are sharp but due to irradiation serious

changes occur. The first Si layer (below the topmost C layer) practically disappears; it was consumed by the SiC production. On the other hand, only a part of the second Si layer was converted to SiC. This can be understood considering the projected range of the 40 keV Ar^+ being about 40 nm. The last carbon layer remained more or less untouched. Considering the shape of the SiC distribution e.g. at 50 and 70 nm one can conclude that the SiC is growing from the Si/C interface.

To check the corrosion resistance of the SiC rich layer potentiodynamic electrochemical test in 4M KOH solution were performed. The potentiodynamic corrosion test provides the quantitative characterization of the coating layer. The measured corrosion resistance of the SiC-rich layers was orders of magnitude better than that of pure silicon. To find the correlation between the amount of SiC and corrosion resistance a new quantity, the effective areal density, was introduced. Fig. 2 shows that a reasonable correlation between these two quantities has been established. In this way a connection between IBM and the corrosion resistance of the layer was given. Since the amount and distribution of SiC can be determined by TRIDYN simulation [G. Battistig, et al., J. Phys. D: Appl. Phys. 2016, 49, 185303-185311] one can predict the corrosion resistance for given sample and irradiation conditions. The method thus can be utilized to make tailored SiC coatings for e.g. sensors operating in harsh environments.

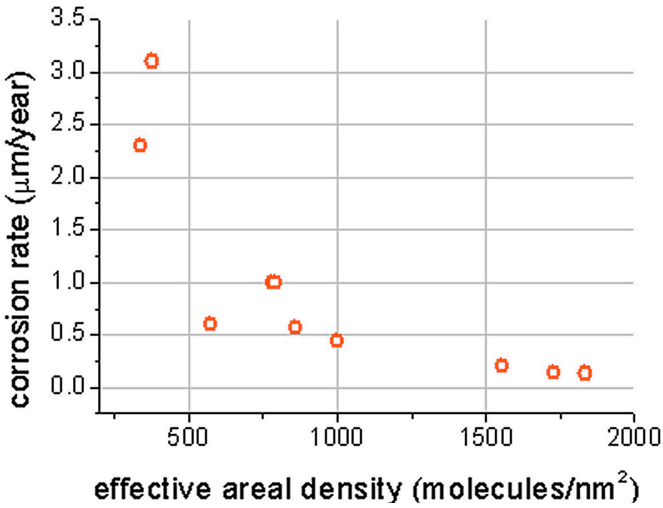

Figure 2 *Corrosion rate vs effective areal density.*

EVENTS

The 15th Conference & Exhibition of the European Ceramic Society (ECerS2017, www.ecers2017.eu) was held in Budapest, between 9 and 13 July 2017, truly one of the most important world ceramic events. For the first time, the Conference was organized jointly by two member societies namely the Hungarian Scientific Society of the Silicate Industry (SZTE) and the Turkish Ceramic Society (TCR).
Since the first ECerS Conference in 1989, the tremendous growth in interest and participation from ceramic communities has made the ECerS Conference a globally popular venue for scientists, artists, students and industrialists willing to have a direct access to one of the largest community of international experts of ceramic art, science and technology.

Opening Ceremony of ECers2017 conference, from left to right: Prof. Alpagut Kara (TCR, co-chair), Dr. Csaba Balázsi (MTA EK, chair), Mr. Moritz von Wintzleben (ECers president 2017-2019), Prof. Pavol Sajgalik (ECers president 2015-2017), Prof. Servet Turan (TCR, chair), Dr. Katalin Balázsi (MTA EK MFA, co-chair), Mr. István Asztalos (SZTE president).

Institute Director Dr. Béla Pécz co-chaired one of the ECerS2017 satellite events „New Frontiers on the Ceramic Characterization Techniques„ which covered measurement techniques, reliability, and problems associated with this testing method of ceramic materials with respect to different microscopic techniques. The further aim of the event was to visit the Centre for Energy Research, Institute for Technical Physics and Materials Science, which has been utilized as a microscopic laboratory for research and various industrial and medical applications of ceramics.

Our former director József Gyulai is not only ordinary member of the Hungarian Academy of Sciences, but was elected as member of Academia Europaea in 2017. He is shown giving his talk in the photo above.

Gábor Battistig, was awarded by the Knight's Cross of Order of Merit of Hungary on our National Holiday of 15th March.

SCIENTIFIC REPORTS

Nanostructures Laboratory & 2D 'Lendület' Research Group

Head: Dr. Levente TAPASZTÓ, Ph.D., senior research fellow

Research Staff

- Zsolt Endre HORVÁTH, D.Sc., Deputy Head of Laboratory
- Prof. László Péter BIRÓ, Corr. Member of the HAS
- Gergely DOBRIK, Ph.D.
- Krisztián KERTÉSZ, Ph.D.
- Antal Adolf KOÓS, Ph.D.
- Géza István MÁRK, Ph.D.
- Péter NEMES-INCZE, Ph.D.
- Zoltán OSVÁTH, Ph.D.
- Péter SÜLE, Ph.D.
- Péter VANCSÓ, Ph.D. (on leave)

Ph.D. students / Diploma workers

- Péter KUN, Ph.D. student
- Gábor Zsolt MAGDA, Ph.D. student
- András PÁLINKÁS, Ph.D. student
- János PETŐ, Ph.D. student
- Gábor PISZTER, Ph.D. student

Main expertise of the Nanostructures Laboratory lies in synthesis and atomic scale characterization of various nanostructures. In recent years, research efforts were focused on two-dimensional (2D) materials. Research areas cover synthesis of various 2D crystals, their characterization with atomic resolution, and nanoengineering. Furthermore, studying electronic properties thereof, and fabrication of proof of concept electronic devices based on 2D materials and their nanostructures. Most intensively invetigated materials are: graphene, dichaclogenide single layers of various transition metals, layered topological insulator crystals, as well as photonic nanoarchitectures of biological origin.

Important results from 2017:
- Demonstrated was that 2D $MoS_{2-x}O_x$ crystals synthesized by us, display a substantially increased catalyitic activity in hydrogen evolution reaction as compared with pure 2D MoS_2 phase. We have also shown that the increased catalytic activity can be attributed to the single atomic oxygen substitution sites.
- By atomic resolution STM measurements, interaction effects in chaotic quantum billiard of Dirac electrons within a graphene nanotriangle of 10 nm side length were observed.

Catalytically active single oxygen sites in the basal plane of 2D MoS_2 crystals

(ERC StG NanoFab2D 680263, Lendület LP2014-14)

J. Pető, P. Vancsó, T. Ollár (EK-FKL), P.B. Sorokin (MISis-Moscow), and L. Tapasztó

A major objective in catalysis is the atomic level identification and control of catalytically active sites for a specific reaction. Here we propose that this can be realized in molybdenum disulfide (MoS_2) through a simple oxidation process. In contrast to the generally accepted view of environmentally inert basal plane, we found that during ambient exposure oxygen gradually incorporates into the basal plane of two-dimensional (2D) MoS_2 crystals by replacing individual sulfur atoms. These O substitution sites were identified as single-atomic active reaction centers for H_2 evolution, extending the catalytic activity of MoS_2 crystals from edges over the entire basal plane. The substitutional oxidation of 2D MoS_2 crystals provides a novel chemical engineering method of unprecedented control to design highly efficient 2D electrocatalysts with a high density of single-atomic active basal plane sites.

We have investigated the catalytic activity of 2D $MoS_{2-x}O_x$ crystals for the electrochemical hydrogen evolution reaction (HER). Polarization curves (I-E) on both $MoS_{2-x}O_x$ and MoS_2 single layers were measured. This way, catalytic activity of the very same flake both with and without O substitution sites in the basal plane manifested itself, as revealed by STM characterization.

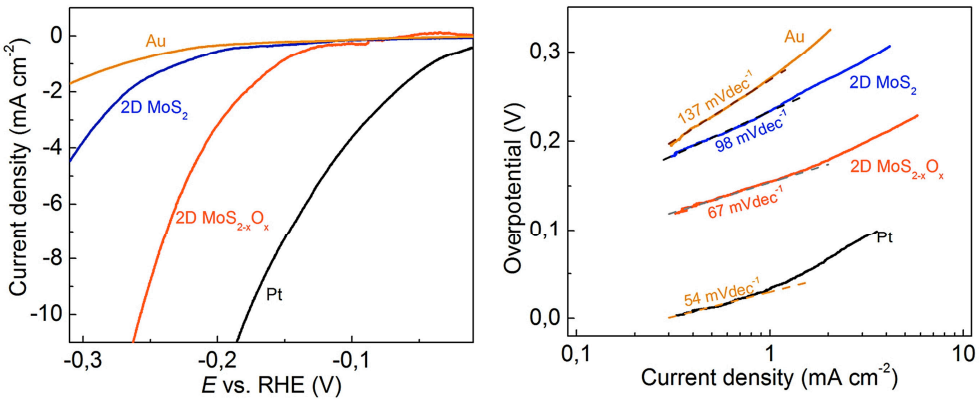

Figure 1 *Catalytic activity of 2D $MoS_{2-x}O_x$ in the hydrogen evolution reaction (HER). Linear sweep voltammograms (a) and the corresponding Tafel plots (b) for: Au substrate, MoS_2 single layer, $MoS_{2-x}O_x$ single layer, and Pt substrate, revealing the significantly higher catalytic activity of the 2D oxy-sulfide phase as compared to the pure MoS_2 phase, attributed to the novel catalytically active oxygen substitutional sites incorporated into the basal plane during the ambient exposure.*

Measured polarization curves and the corresponding Tafel plots shown in Fig. 1 evidence a highly increased catalytic HER activity of the 2D $MoS_{2-x}O_x$ solid solution

crystals, as compared to the reduced pure 2D MoS_2 phase. Consequently, this enhanced catalytic activity can be clearly related to the presence of substitutional O sites. STM measurements following the catalysis confirmed that structural integrity of the 2D $MoS_{2-x}O_x$ crystals was preserved even after several hundreds of cycles. Our DFT calculations in accordance with the literature show that the mid-gap states characteristic to S vacancies that are proposed to play an important role in catalytic activity are absent for oxygen substitution sites (Fig. 2). In this light, it might seem surprising that O substitution sites still display a similar or even higher catalytic activity as S vacancies. A possible explanation is that a different mechanism is responsible for enhancing the catalytic activity of the O saturated vacancies. The Bader charge analysis (Fig. 2) reveals a strong acceptor type behavior of the O substitution sites, implying a local negative charge surplus of about - 0.88 *e*. This, combined with the experimentally measured overall n-doping of the flakes imply the presence of highly localized negative charges on the O substitution sites, which, through electrostatic interaction, can enhance binding of protons. Furthermore, after the charge transfer, neutral hydrogen atoms are less attracted to the O sites, facilitating their release for the subsequent recombination step to H_2.

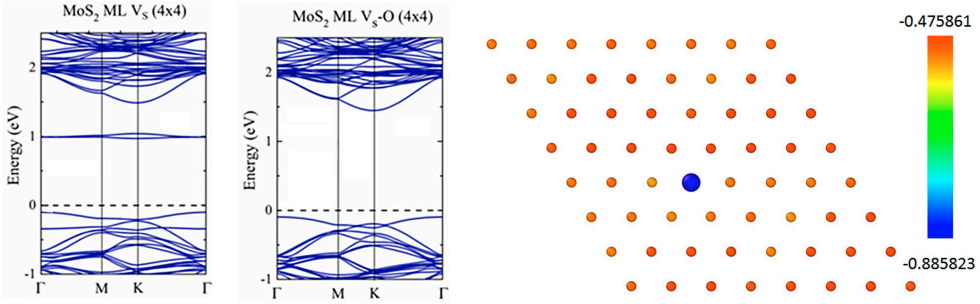

Figure 2 *Calculated DFT band structure of the, sulfur vacancy site MoS_2-V_S, and oxygen substitution site MoS_2-V_S-O. Bader charge analysis of the $Mo_{64}S_{127}O$ surface revealing the electron acceptor nature of the O substitution site characterized by -0.88e excess negative charge.*

Understanding catalytic processes is a highly challenging task, in big part due to the complexity of the systems experimentally investigated being in strong contrast to the idealized theoretical models. 2D $MoS_{2-x}O_x$ provides an ideal model system for understanding atomic level relations between active sites and catalytic HER activity, as it is characterized by a single type of active site. The site with experimentally known atomic structure, while edges and previously investigated more disordered MoS_2 structures can host a variety of active sites with complex atomic configurations and often little experimental insight into their precise atomic nature. These findings clearly evidence that the substitutional oxidation process of the MoS_2 basal plane reported here can open new routes for engineering 2D electro-catalysts with single oxygen atom active sites of a much higher site density than previously achieved for individual hetero-atom catalysts.

Observation of large band gap modification in single-layer MoS_2 due to formation of nanobubbles

(Lendület LP2014, ERC StG NanoFab2D 680263, OTKA K 108753, Korea-Hungary Joint Laboratory)

J. Pető, G. Dobrik, P. Nemes-Incze, G. Kukucska, J. Koltai (ELTE), and L. Tapasztó

The family of transition metal dichalcogenides has received much research interest in the last few years owing to unique properties when stripped to only one layer. Some of the members exhibit semiconductor behavior with a direct bandgap (MoS_2, $MoSe_2$, WS_2 etc.), which makes them particularly useful in electronic and optoelectronic applications. In case of direct band gap materials, as there is no need for a simultaneous photon-electron-phonon interaction, quantum efficiency can increase even by a factor of 10^4. In order to fully exploit the potential of these materials in future applications however, it is necessary to find ways to tune the bandgap. One of the promising methods to accomplish this task is engineering the band gap by applying mechanical strain to the 2D crystal structure. This allows us to make a fully reversible change of the band gap that leaves chemical composition intact. DFT calculations predict a band gap decrease of 0.2 eV for 1% strain. The method can be effective if the application of considerable strain is possible. Our investigations revealed that highly strained areas naturally occur within MoS_2 single layers upon van der Waals interaction with substrates. The contamination trapped at the interface is squeezed into nanoscale bubbles by the van der Waals forces. The pressure in such nanobubbles can reach high values, which imparts a significant mechanical strain to the MoS_2 monolayer.

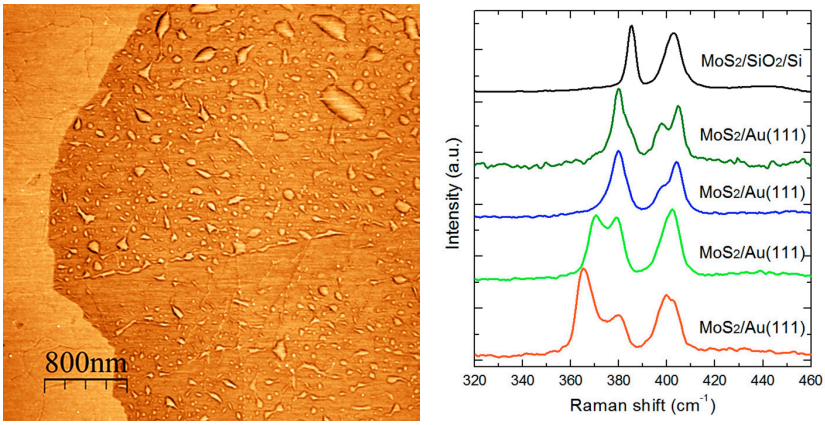

Figure 1 *AFM (phase) image of nanobubbles within the MoS_2 single layer exfoliated onto Au (111) substrate. Raman measurements display strong shifts og the MoS_2 main peaks that can be attributed to the large (1 - 5%) mechanical strain within the bubbles.*

We have also investigated the MoS_2 nanobubbles by Scanning Tunneling Microscopy. The diameter of the bubbles is typically in the 10-300 nm range with an aspect ratio (h/R) of 0.5 - 1.5. An example can be seen in Fig. 2.

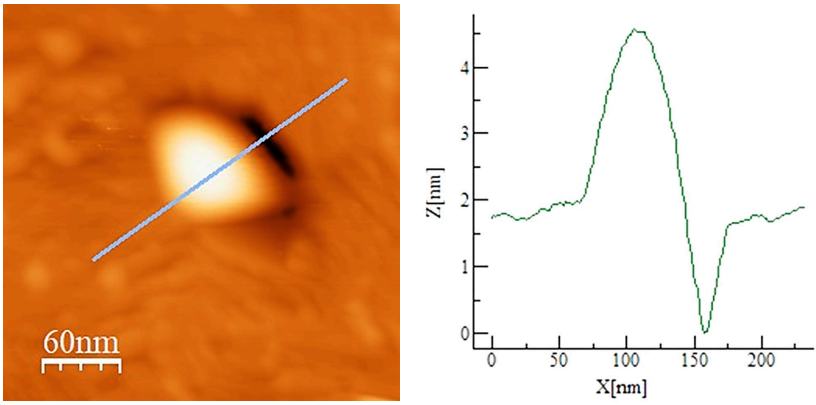

Figure 2 *STM image of a nanobuble formed in the MoS_2 monolayer on Au (111) substrate (left). A line profile can be seen in the image and its plot shows the size of the bubble to be 75 nm in diameter with the top of the bubble reaching a 2.5 nm height.*

In order to test the theoretically predicted and significant decrease of band gap upon strain, we performed Tunneling Spectroscopy measurements on the nanobubbles where deformation of the lattice was significant.

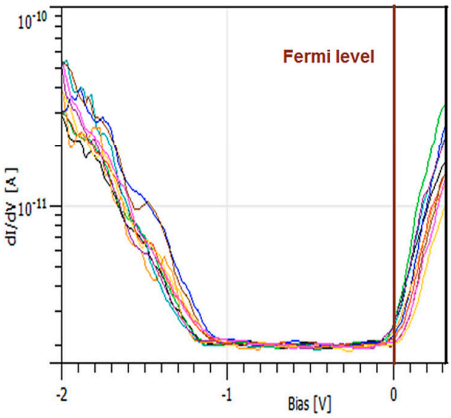

Figure 3 *Tunneling spectra at the center of a nanobubble displaying a band gap is only 1-1.1 eV, and the Fermi level shifted out of the gap into the edge of the conduction band.*

While the intrinsic bandgap of the strain-free MoS_2 monolayer is about 2 eV, the nanobubble shows only a 1-1.1 eV band gap. Thus the band gap is decreased due to strain by about 0.9 eV. Our experimental findings clearly evidence that strain engineering is a very powerful tool also for engineering the band gap of transition metal dichalcogenides.

Interaction effects in a chaotic graphene quantum billiard

(EU FP7 GraNaRip 334377, OTKA K 119532)

I. Hagymási (Wigner FK), P. Vancsó, A. Pálinkás, and Z. Osváth

The appearance of two-dimensional materials like graphene has renewed the interest in the properties of quantum dots and quantum billiards made of these materials. Here we examined a quadrilateral shaped graphene quantum dot, which is a truncated triangle having three zigzag and one armchair edges (see Fig. 1a). This peculiar shape resembles the theoretically well-studied Sinai billiard. In this joint experimental and theoretical study we use scanning tunneling microscopy (STM) and perform theoretical calculations to understand the experimental results. Our main finding is that the electron-electron interaction must be taken into account to reproduce the STM images and the local density of states (LDOS) measurements, which highlight the important role of the interactions in quantum dots in graphene even at room temperature.

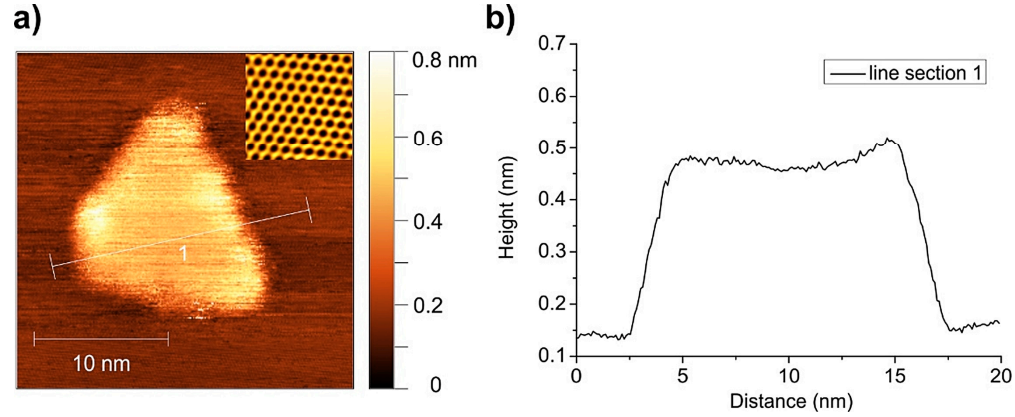

Figure 1 ***(a):*** *STM image of the investigated graphene quantum dot. Tunneling parameters:U = 200 mV, and I = 1 nA. The atomic resolution inset image shows the crystallographic orientation in the dot.* ***(b):*** *Height profile taken along the line section 1 in (a), showing monolayer thickness.*

Graphene grown by chemical vapor deposition (CVD) onto electropolished copper foil was transferred onto a highly oriented pyrolytic graphite (HOPG) substrate using thermal release tape. Graphene nanostructures were obtained by annealing the graphene/HOPG sample at 650 °C for two hours in an argon atmosphere. STM and scanning tunneling spectroscopy (STS) measurements were performed using a DI Nanoscope E operating under ambient conditions. Atomic resolution images on the dot (inset of Fig. 1a) reveal that the nanostructure has three zigzag edges and one armchair edge.

In Fig. 2 (first row), we can see different superstructure patterns within the quantum dot measured at various voltages. The well-known $(\sqrt{3}\times\sqrt{3})R30°$ superstructure (marked by white circles) appears in addition to the atomic structure.

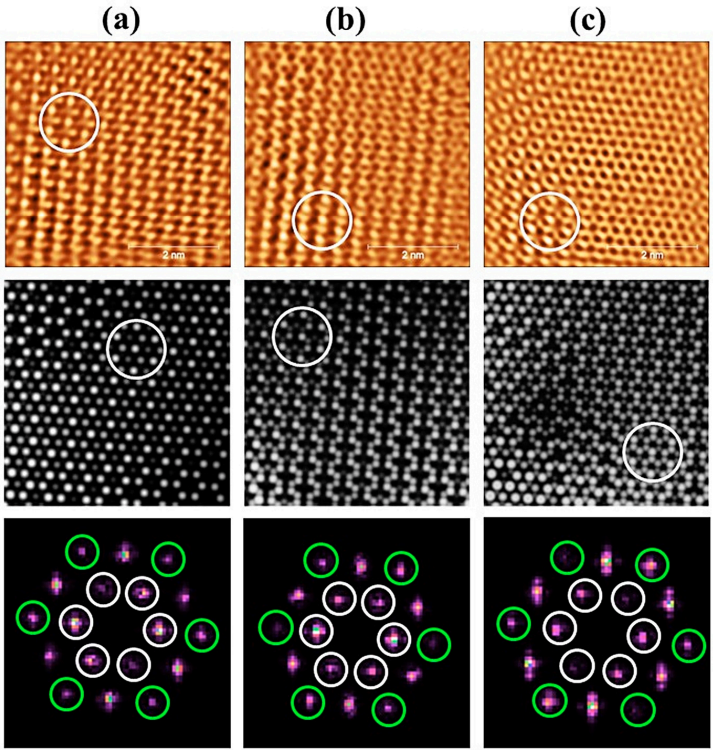

Figure 2 *Topographic STM images within the quantum dot. Each column corresponds to a different voltage where the measurement was done:* ***(a)****,* ***(b)****, and* ***(c)*** *belong to U = 100, 25, and -50 mV, respectively. The first row shows the measured images, the second one contains the simulated images, while the third row displays the Fourier spectra of the measured images. The spots inside the white circles in the Fourier spectra are the components of the (√3×√3)R30° superstructure, while the green circled spots are their overtones. The noncircled spots correspond to the periodicity of the atomic lattice.*

Additionally, stripes parallel to the armchair edge and rings are observed in the measured STM images. In order to simulate these distinct STM images, a finite electron-electron interaction was considered. STM images were simulated with the simple Tersoff-Hamann approximation and by using calculated LDOS of the interacting system. Taking into account the electron-electron interaction, we can quantitatively reproduce the measured STM images, including the (√3×√3)R30° superstructure, the stripes, and the rings at different voltages (Fig. 2, second row). Fourier spectra of the measured images (Fig. 2, third row) show that the Fourier components of the (√3×√3)R30° superstructure are always present (inner hexagon, white circles). Moreover, their harmonics (marked with green circles) appear with various amplitudes, which results in the formation of different, more complex patterns in the topography images. The emergence of the harmonics measured by STM is attributed to Umklapp scattering processes, which serve as a further evidence for the presence of electron-electron interaction in our system.

Atomic scale electronic properties of single layer $MoSe_2$ crystals grown on graphite

(János Bolyai Research Scholarship, ERC StG NanoFab2D 680263)

A. A. Koós, Z. Osváth, A. Pálinkás, G. Dobrik, K. Kertész, L. P. Biró, and L. Tapasztó

Unique properties of 2D materials like graphene and transition metal dichalcogenides offer unprecedented opportunities in a wide range of applications, for example designing better electronic devices, faster sensors, more efficient catalysts or optoelectronic devices. The combination of layered materials in hybrid nanostructures allows us to further improve applicability of these materials. For example, hybrids of graphene with zero-gap character and semiconducting $MoSe_2$ are expected to become building blocks of next generation high performance nanoelectronic devices. In order to understand properties of graphene-$MoSe_2$ hybrids, the $MoSe_2$ sheets were grown by chemical vapour deposition (CVD) on highly ordered pyrolytic graphite (HOPG). The hetero-structures formed were investigated with Scanning Tunneling Microscopy (STM) and Scanning Tunneling Spectroscopy (STS) at atomic resolution.

The $MoSe_2$ flakes grown on HOPG follow the crystallographic orientation of the substrate (Fig. 1a). It was found that the apparent height of the flake edges was higher than the apparent thickness of the flake, which indicates that the electronic properties at edges are different (Fig. 1b). In order to exclude artifacts due to contamination of the edges during the CVD growth, we formed freshly cut edges by nanolithography, and found that the apparent height increase was the same.

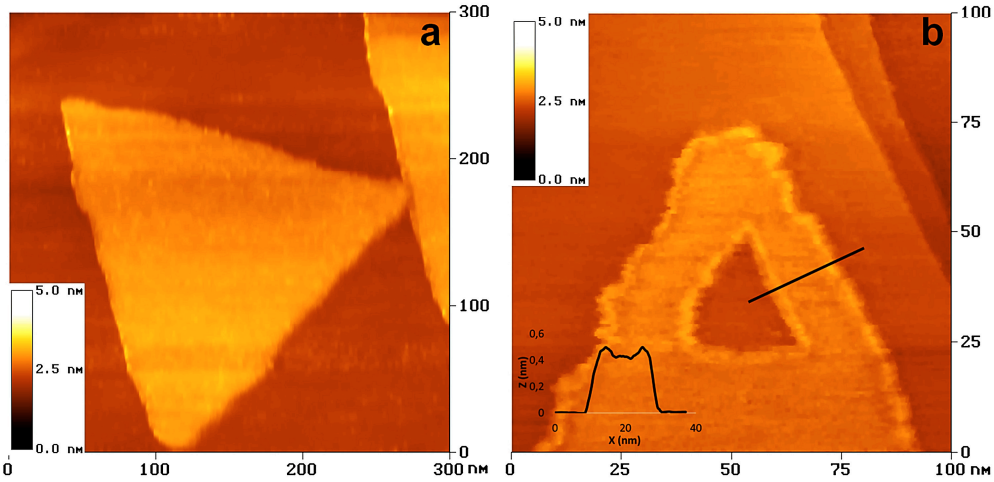

Figure 1 ***a)*** *STM image of a $MoSe_2$ flake grown on HOPG.* ***b)*** *Higher resolution STM image of a $MoSe_2$ crystal with a cut made by nanolithography. Inset: Height profile along the black line.*

We have investigated the effect of tunneling current and voltage on the quality of STM images. We found that at negative voltages it was possible to highlight the grain

boundaries between $MoSe_2$ single crystals. Interestingly, number of visible defects strongly depended on STM imaging voltage (Fig. 2a-c). This suggests that defect-localized electronic states of certain energy are present. From tunneling spectroscopy measurements, it became obvious that at a defect site the conduction band slightly decreased at defects and a localized defect induced midgap states to appear at about -600 meV (Fig. 2d). Consequently, defects become visible only when imaging at negative bias voltages are below -600 meV, in accordance with topographic images. These effects must be considered during the design of 2D $MoSe_2$-based nanoelectronic devices.

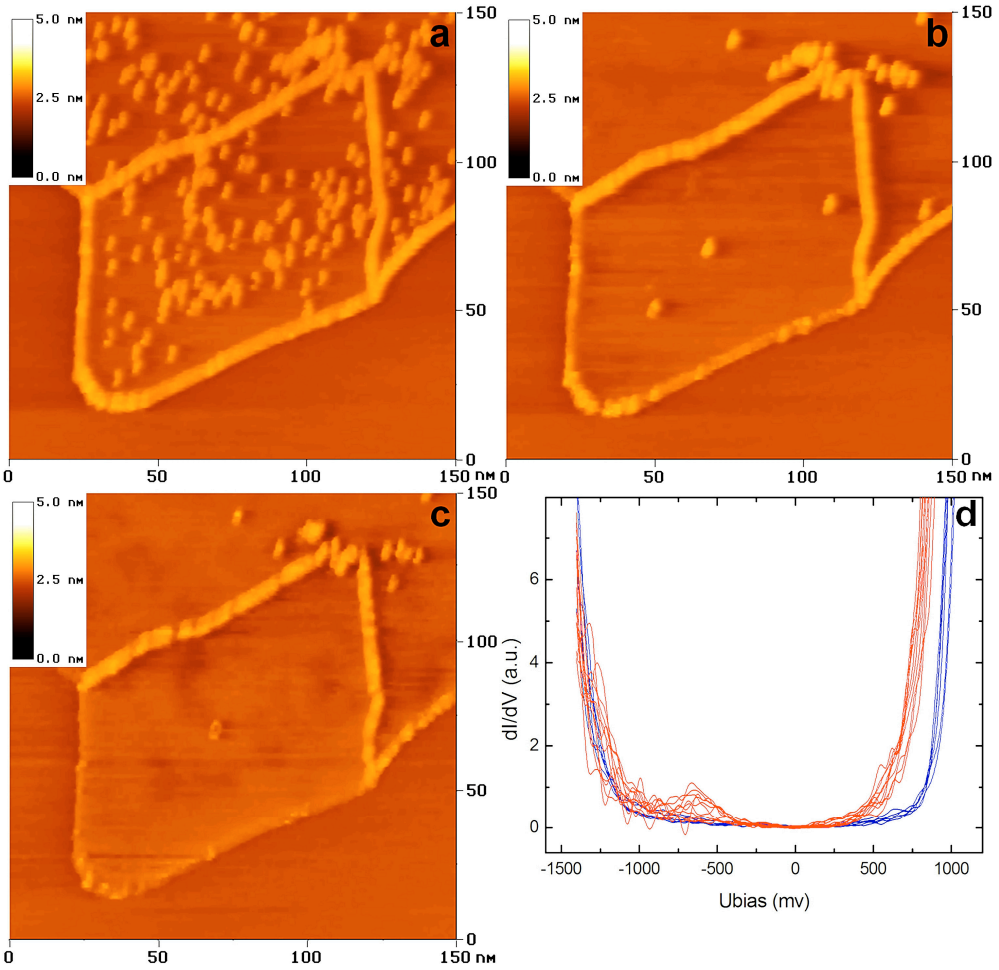

Figure 2 a-c) *Effect of bias voltage on the visibility of $MoSe_2$ defects. The images were recorded at 200 pA. The voltage was selected -1V* ***(a)****, -0.5 V* ***(b)*** *and -0.1 V* ***(c)****, respectively.* ***(d):*** *STS recorded above $MoSe_2$ flake (blue) and defects (red).*

In conclusion, CVD offers the opportunity to produce high quality graphene-2D MoSe2 heterostructures, their structure and properties, however, should be carefully investigated when developing reliable applications.

Novel graphene/Sn and graphene/SnO_x hybrid nanostructures: band gaps revealed by scanning probe measurements

(EU FP7 GraNaRip 334377, OTKA K 119532, TÉT_12_SK-1-2013-0018)

A. Pálinkás, Gy. Molnár, G. Zs. Magda, C. Hwang (KRISS, Korea), L. Tapasztó, P. Samuely (IEP SAS Slovakia), P. Szabó (IEP SAS Slovakia), and Z. Osváth

Graphene has attracted substantial research interest due to its outstanding properties. Hybrid nanostructures integrating graphene with metallic or semiconducting nanoparticles (NPs) could potentially display versatile and tunable properties, as well as novel or enhanced functionalities arising from the synergy between the properties of graphene and those of NPs. In this work, graphene covered Sn and SnO_x nanoparticles were synthesized and characterized by AFM, and STM/STS. We showed that metallic Sn NPs induce electrostatic doping by transferring electrons to graphene. We also demonstrated that the graphene cover layer prevented oxidation of tin NPs. Graphene/SnO_x hybrid nanostructures were also prepared and the electronic band gap of SnO_x NPs was measured by STS.

Tin was evaporated (7 nm) onto highly oriented pyrolytic graphite (HOPG) surface. Due to the low wetting properties, the evaporated tin film self-organized into nanoparticles. The NPs were covered with CVD-grown graphene, the transfer was done using thermal release tape method. Later the sample was annealed in electric furnace at 500 °C for 30 min in Ar atmosphere. The graphene-covered tin NPs were tested by STM and STS in ambient conditions both before and after annealing. The STM image in Fig. 1a shows graphene covered closely spaced Sn NPs.

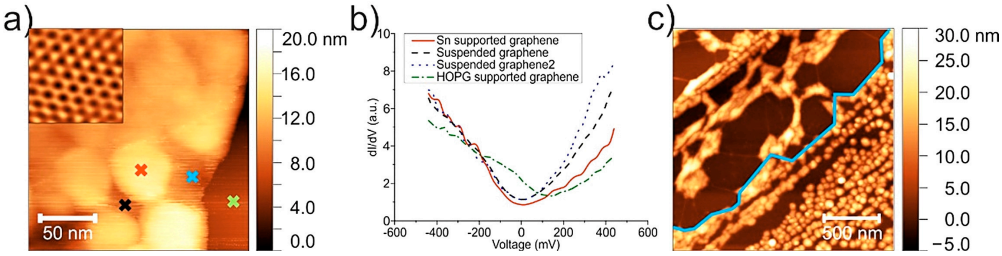

Figure 1 ***(a):*** *STM topography image of graphene covered Sn NPs. The inset shows an atomic resolution image of the Sn supported graphene.* ***(b):*** *dI/dV spectra measured at the positions marked with colored symbols in a) as follows: Sn supported graphene (red), suspended graphene (black, blue), graphene on HOPG (green).* ***(c):*** *AFM Topography image of a partially graphene covered area after annealing at 500 °C. The edge of the graphene is marked with blue line.*

STS measurements were carried out on both Sn supported graphene, and graphene suspended between the Sn NPs. The room temperature STS spectra in Fig. 1b show that the pre-existing environmental p-doping of graphene (see the HOPG supported graphene) can be significantly reduced by the Sn NPs, an effect which prevails in the suspended graphene parts as well.

After annealing at 500 °C the graphene covered regions transformed drastically, the NPs merged into nanorods and other new nanostructures (Fig. 1c), while on the uncovered regions, the sphere-like shape of NPs was preserved. The melting point of Sn, SnO and SnO_2 are at around 230 °C, 1080 °C and 1630 °C, respectively. This phenomenon demonstrates the shielding efficiency of graphene. When annealing was performed three month after the initial tin evaporation, and graphene was able to protect efficiently the Sn NPs from oxidation in this time frame. On the other hand, non-covered NPs exposed to air oxidized completely, and thus they did not melt during annealing at 500 °C.

We also prepared a graphene/SnO_x nanoparticle hybrid material in the same way, except that the evaporated Sn NPs were annealed (oxidized) before covering with graphene. A topographic AFM image of both graphene covered and non-covered NPs is shown in Fig. 2a. Here, the non-covered NPs are observed in the area between the two blue lines.

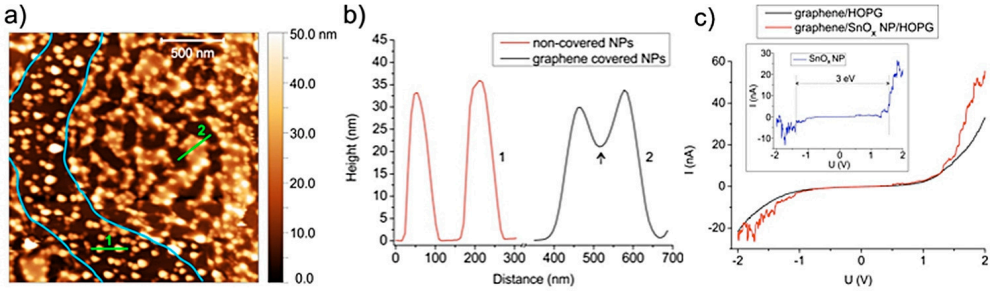

Figure 2 *(**a**): AFM topography of graphene covered SnO_x NPs. Graphene edges are marked with blue lines.* ***(b):*** *Height profiles taken on non-covered (red) and graphene covered (black) NPs.* ***(c):*** *Tunneling spectra on graphene/HOPG (black) and a graphene covered SnO_x nanoparticle (red). Subtracting the graphitic contribution we obtain the tunnelling conductance through the NP (inset, blue line), which shows a band gap of 3 eV.*

Many nanoparticle groups are observed when graphene is suspended between the NPs. This is shown, for example in Fig. 2b, where height profiles taken on non-covered and graphene covered NPs are compared. We investigated the graphene/SnO_x hybrids by STM and STS. The non-covered oxidized nanoparticles could not be imaged with low voltages ($U < 1$ V) due to the high electronic band gap of SnOx. In contrast, graphene covered SnO_x NPs could be well investigated using such low bias voltages also, since graphene immobilizes the NPs and good tunneling conductance is achieved through it. STS measurements revealed band gaps of 2.7 – 3.2 eV, which are better observed when subtracting 'graphenic' contribution of the current (inset of Fig. 2c). In this setting, graphene facilitates the STM investigation of semiconducting NPs by fixing them to the substrate and enabling the study of their density of states by STS.

Changes in structural and pigmentary colours in response to cold stress in Polyommatus icarus butterflies

(OTKA K 111741, OTKA K 115724)

K. Kertész, G. Piszter, Z. E. Horváth, Zs. Bálint, and L. P. Biró

While numerous papers investigated effects of thermal stress on the pigmentary colours of butterfly wings, such studies regarding structural colours were mostly lacking, despite their important role in sexual communication. To gain insight into the possible differences between responses of the two kinds of colouration, we investigated the effect of prolonged cold stress (cooling at 5 °C for up to 62 days) on the pupae of Polyommatus icarus butterflies. The wing surfaces coloured by photonic crystal-type nanoarchitectures (dorsal) and by pigments (ventral) showed markedly different behaviour. On the dorsal wing surface of the males, with blue structural colouration, a smaller magnitude response was found with much more pronounced individual variations (Fig. 1a vs. 1b, & Fig. 1e vs. 1f) possibly revealing hidden genetic variations. The ventral wing surfaces of both sexes exhibited stress responses proportional in magnitude to the duration of cooling and showed the same trend for all individuals, irrespective of their sex (Fig. 1c vs. 1d, & Fig. 1g vs. 1h).

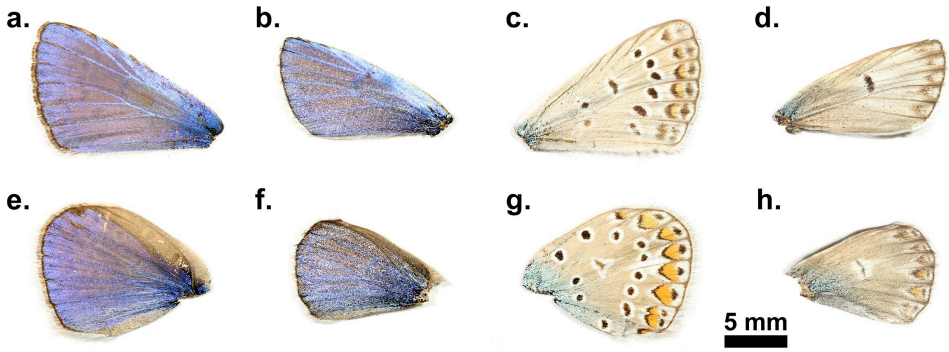

Figure 1 *Wings of wild butterflies and of butterflies eclosed from pupae subjected to prolonged cooling at 5 °C in dark.* ***(a)****: Dorsal forewing of a wild male;* ***(b):*** *dorsal forewing of a male merged from a pupa cooled for 62 days;* ***(c):*** *ventral forewing of a wild male;* ***(d):*** *ventral forewing of a male eclosed from a pupa cooled for 62 days;* ***(e):*** *dorsal hindwing of a wild male;* ***(f):*** *dorsal hindwing of a male emerged from a pupa cooled for 62 days;* ***(g):*** *ventral hindwing of a wild male;* ***(h):*** *ventral hindwing of a male eclosed from a pupa cooled for 62 days.*

The reflectance of the dorsal (blue) wing surfaces (all four wings of each individual) was measured using UV-VIS spectroscopy. Position of the reflectance maximum in the blue region (365–432 nm) was located and plotted as a function of the time they were kept cooled for all the pupae in Fig. 2a. Cold stress for 10 days did not produce significant deviations in the peak position of the blue reflectance. Cold stress for

longer durations (>10 days) caused higher deviations from the normal biological variation of the blue colour of the male P. icarus and induced the appearance of blue scales on all the females, which have brown dorsal wing surfaces in the wild population. The possible cause of the shift in the spectral position of the reflectance maximum may be related to the slight alteration of the dimensions of the photonic nanoarchitecture, or to changes in the scale arrangement.

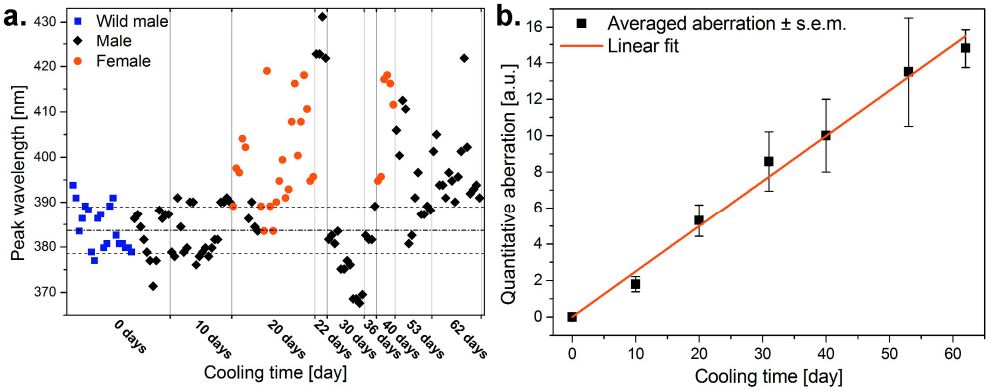

Figure 2 ***(a):*** *Spectral position of the blue reflectance peak for all the investigated exemplars. Horizontal broken lines indicate the range of wild males with centre at 384 nm marked by dotted broken line.* ***(b):*** *The averaged quantitative aberration of the ventral wing surfaces versus the cooling time of the pupae shows linear relationship.*

The ventral side of the wing surfaces of both the males and females exhibited similar complex pigmentation (Fig. 1c and 1g). In fact, this pattern is used by taxonomists to identify these species. It is possible to assign a certain numerical value to any deviation (Fig. 1d and 1h) from the standard pattern observed on normal individuals, enabling quantitative evaluation of the degree of aberration of the pigment colours. We qualified and coded the wing size, ventral wing-surface colouration and pattern in comparison with individuals of the control group as a standard. Numerical value of the aberration was averaged for butterflies eclosed from pupae cooled for the same number of days, and the results are plotted in Fig. 2b. One may observe that the quantitative value of the aberration shows a very closely monotonic and linear variation with the length of the cooling period endured by the pupae.

Clearly, colouration generated by nanoarchitectures and the colouration generated by pigments reacted differently to the stress produced by prolonged cooling of the pupae. This finding may be less surprising if one considers that the two processes, scale formation and pigmentation, are well separated in time, and also perform different functions in the life of these butterflies. The blue colouration, used for sexual communication, is much more stress resistant than the pigment-generated pattern of the ventral wing surface, which is used for camouflage: significantly smaller magnitude changes were induced by the prolonged cooling in the blue color of the males, as compared to the alteration of their ventral wing patterns.

Photonics Department

Head: Dr. Peter PETRIK, D.Sc., scientific advisor

Research Staff

- Emil AGÓCS, Ph.D., (on leave)
- Csaba S. DARÓCZI, dr. Univ.
- András DEÁK, Ph.D., Head of Chemical Nanostructures Laboratory
- Miklós FRIED, D.Sc., Head of Ellipsometry Laboratory
- Antal GASPARICS, Ph.D.
- András HÁMORI, dr. Univ. (retired)
- Norbert NAGY, Ph.D.
- György JUHÁSZ, dr. Univ. (retired)
- György KÁDÁR, D.Sc. (Prof. emeritus)
- Tivadar LOHNER, D.Sc.
- János MAKAI, C.Sc. (retired)
- Judit NÁDOR, Ph.D.
- Ferenc RIESZ, C.Sc.
- Miklós SERÉNYI, D.Sc.
- Gábor VÉRTESY, D.Sc.
- Dániel ZÁMBÓ, Ph.D.

Students

- Bálint ÉLES, B.Sc.
- Bálint FODOR, Ph.D.
- Benjamin KALAS, Ph.D.
- Olívia KOZÁK, B.Sc.
- Enikő MOLNÁR, B.Sc.
- Szilárd POTHORSZKY, Ph.D.
- Alekszej ROMANENKO, M.Sc.
- Dániel SZEKRÉNYES, Ph.D.
- Alex SZENDREI, B.Sc.

Technical Staff

- Tímea CSÁNYI

The objectives of the Photonics Department are the preparation as well as the non-destructive and real time characterization of thin films on large surfaces, in photonic and complex structures; development of optical and magnetic measurement methods for the improvement of sensitivity and for the broadening of the range of materials that can be investigated by these methods; preparation and spectroscopic characterization of self-organized surface nanostructures; in situ monitoring of solid-liquid interface processes for the understanding of the adsorption of complex biomolecules and for the optimization of thin film preparations for sensors.

Some of the major results in 2017:

- A recently developed nondestructive method called Magnetic Adaptive Testing (MAT), which is based on systematic measurement of minor magnetic hysteresis loops, was compared to other non-destructive magnetic methods, and it was proven that the MAT method has a higher sensitivity and a better applicability for

the characterization of inhomogeneities and sample damage at larger distances from the surface.

- The MAT method was tested on special samples; based on finite element calculations it was shown that the non-destructive tool is capable of the quantitative determination of irregularities in the shape and geometry of the samples.
- It was proven that the method is capable of the testing the weld quality.
- Single-particle spectroscopy has been developed and applied to control and understand the effect of the chemical and physical parameters of the colloid system on the interactions between the gold nanoparticles.
- A capillary bridge method has been developed for the high-sensitivity measurement of the wetting properties and the related parameters (e.g. cleanliness) of surfaces.
- Thin films and surface properties of zirconium tubes and plates have been investigated using spectroscopic ellipsometry for nuclear applications.
- A polarization-based optical method has been developed for the quantitative and high-sensitivity (on the nanometer scale) determination of film thickness, surface quality on large areas (up to a square meter), with high resolution (thousands of pixels) and high speed (seconds). This method is unique for the high-precision and quantitative mapping of surfaces on such a large scale.
- Electronic sensors have been created from genetically modified bacterial filaments to test the quality of water.
- Models have been developed for the optical characterization of germanium nanoparticles embedded in zirconium oxide.
- Correlation has been revealed between the quantity of protein layers on the nanometer scale deposited on gold films measured by ellipsometry and X-ray fluorescence.
- The quality and effect of hydrogenation on the thin film properties in silicon-germanium has been investigated.
- A device has been developed for photoluminescence measurements.

Detecting patchy nanoparticle assembly at the single-particle level

(OTKA K 112114, and OTKA K 119532)

S. Pothorszky, D. Zámbó, D. Szekrényes, Z. Hajnal and A. Deák

Patchy colloids allow the development of a spatially inhomogeneous interaction profile and depending on the number and arrangement of the patches, the valence and directionality of the interaction can be controlled. Due to their intense light scattering, noble metal nanoparticles represent an ideal class of model system for the investigation of self-assembly processes at the single particle level.

Relying on the unique optical properties of the heterodimers composed of a patchy gold nanorod and a nanosphere, direct, in situ information on the structure of the assembly can be obtained using single particle scattering spectroscopy combined with correlative electron microscopy investigations. This combined technique opens the possibility to correlate optical properties with relative position of the particles in the heterodimer. In situ measurements performed in a liquid cell give direct information about how the self-assembled structure evolves in the aqueous phase (Fig. 1). Furthermore, both the directing feature of colloidal interactions and immersion type capillary forces can be investigated separately.

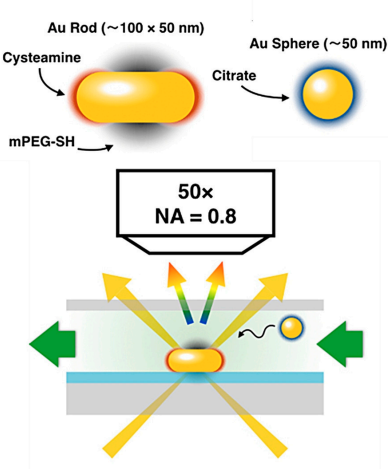

Figure 1 *The prepared nanoparticles (top) and the measurement arrangement (bottom). The patchy nanorods are first immobilized on ITO covered substrates, then the aqueous nanosphere solution is introduced and changes in the scattered spectrum upon binding detected.*

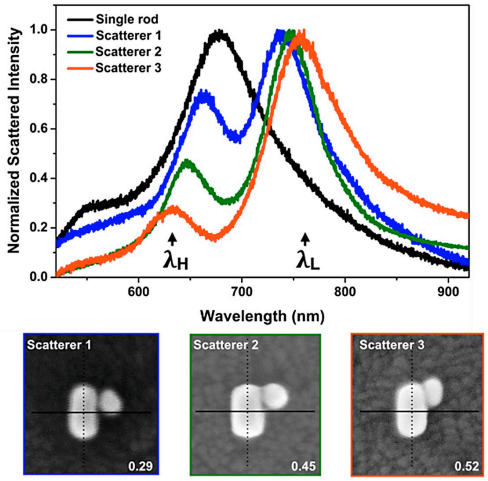

Figure 2 *Typical scattering spectra measured in situ in the liquid cell and the corresponding SEM images. The numbers indicate their respective relative displacement.*

During *in situ* measurements, a blueshifted higher (H) and a redshifted lower (L) energy peak were appeared at around the initial longitudinal plasmon peak of the rod indicating the formation of a heterodimer (Fig. 2.). Based on the energy difference between the two peaks, the spheres were attached to the side region already in the aqueous phase. The side-localization of the spheres and its distribution for the given rod/sphere heterodimer can be interpreted based on the combined effect of dispersion, electric double layer and steric interactions. The results can contribute to the rational design of nanoscale patchy particles for a better control over the resulting assembly structure [105].

Magnetic flux simulation for the inspection of local thinning of ferromagnetic plates – Experimental verification

(OTKA K 111662)

G. Vértesy, Cs. S. Daróczi, and A. Gasparics

For pipes used in industry, wall thinning is one of the most serious defects. Detection of the thickness reduction is a very important issue for prediction of lifetime of the pipes in order to avoid severe accidents. The inspection should be done from the outer side of the pipe. A recently developed nondestructive method called Magnetic Adaptive Testing (MAT), which is based on systematic measurement and evaluation of minor magnetic hysteresis loops, was successfully applied for the detection of local wall thinning in ferromagnetic plates. It was shown, that even a relatively small, local modification of the plate thickness could be detected from the other side of the specimen with an adequate signal/noise ratio.

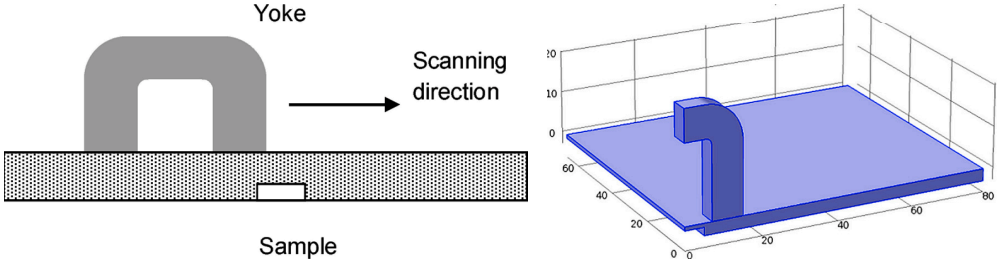

Figure 1 *Configuration used both for measurement and simulation. The geometry on the right represents a quarter-view of the arrangement, showing only part of the whole plate, and with the yoke in central position right above the slot.*

To improve applicability of MAT, the measurement conditions should be optimized. It is important to study, how modification of the measured hysteresis loops, caused by the presence of an artificial slot in the investigated ferromagnetic plate(s), and are influenced by the parameters of the measurement arrangement. Previously we calculated how geometry of the measured arrangement affects change of the magnetic

flux inside the magnetizing yoke. Result of the simulation helped to find optimal parameters of the experimental arrangement.

The purpose of the present work is to perform numerical simulations of the measurement on a single ferromagnetic steel plate which contains various artificial slots of different size, and to compare results of the simulations with the experimental data. Measurements were done by MAT, by moving the magnetizing yoke over the surface. A ferromagnetic steel plate of size 500 mm × 300 mm × 6 mm was considered, which contained an artificial rectangular slot, the size of which is varied. Fig. 1 shows the configuration of the measurement and simulation.

Change of the magnetic flux density in the cross section of the magnetizing yoke, which occurs due to the presence of the artificial slot, was calculated as a function of the size of the slot. The AC/DC Module of the Comsol Multiphysics® finite element software was used for the simulations. By the simulations we investigated how this flux change depends on the size of the slot. Three slot widths (5, 10 and 15 mm) were combined with three slot depths (1, 2 and 3 mm) resulting all together in nine different cases. The result of simulation can be seen in Fig. 2(a), while the results of the measurements are given in Fig. 2(b).

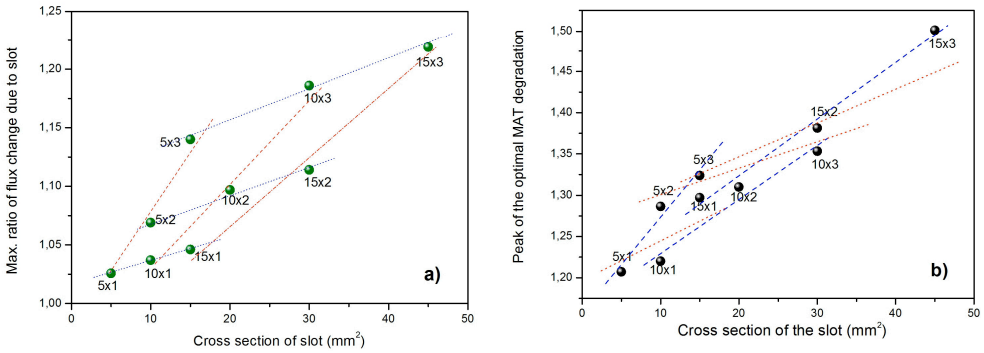

Figure 2 *Maximum values of flux change for different cross sections of the slots.* ***a):*** *calculated,* ***b):*** *measured.*

It was found that existence of the investigated artificial slots can be detected with a good signal to noise ratio by MAT method. The evaluated parameters indicate presence/absence of the slot and are able even to reflect size of the slot quantitatively. Numerical simulation confirmed that detection of the slot by a magnetic inspection head (i.e. the magnetic yoke with the necessary coils) attached to the investigated steel plate from the side opposite to where the slot is situated makes sense. The signal measured inductively by the experimental method in the pick-up coil originates from variation of the magnetic flux inside the magnetic circuit composed of the magnetizing yoke and of that part of the ferromagnetic plate, which contains the investigated slot.

The results of both the simulation and of the experimental measurement showed nearly linear correlation between the evaluated parameters and the cross section of the slots. This was true both for the case when depth of a given slot was fixed and its

width was modified, and also when width of a given slot was fixed and its depth was varied. However, the slopes were significantly different. Consequently, we can conclude that depth of the slot has a larger influence on the measurable signal than its width, considering the same slot volume. Good qualitative correlation was found between the *calculated* maximum relative change of the magnetic flux, and the peak values of the optimally determined *measured* MAT normalized parameters. A useful message of the present work is to show the tendency, that is, how parameters of the testing arrangement affect the measured magnetic flux. This result can also be important for identification of the slots from the measured signal.
The good correlation between the calculated and measured quantities also means the experimental validation of the used simulation method.

Development of optical metrology tool for in-line qualification of thin films on large area

(EU FP7 SEA4KET-611332, ENIAC E450EDL-325613, NEMZ_12-1-2013-0001)

Cs. Major, Gy. Juhász, P. Petrik, and M. Fried

We were involved in 2 EU-projects („SEA4KET" and the ENIAC-2012-2 "E450DL") to develop "Imaging Optical Inspection Device With A Pinhole Camera". Our tool is unique for the characterization of thin films over large area. Using this tool developed in the Photonics department, thin film properties such as the thickness, the refractive index and related physical properties from the spectroscopic measurement, such as the conductivity or the crystallinity, can be determined within several minutes on a large area. We developed 30, 45-60 and 60-90 cm wide prototypes for mapping the optical properties of thin films of big area samples measuring in approximately 1000 points.

Figure 1 *We installed our optical mapping device in the clean-room of IISB (Erlangen, Germany). A 300 mm diameter wafer can be seen on the robotic arm (left side).*

300 mm diameter SiON-on-Si wafers were measured on the robotic arm in clean room environment. We determined the thickness maps on these big wafers and compared it with reference measurements on a commercial Woollam M-2000DI spectroscopic ellipsometer. The results show a good agreement between our maps and the reference one, both having a good fit quality (mean squared error, MSE) or the spectra. For the sake of brevity, the fitted spectra are not shown.

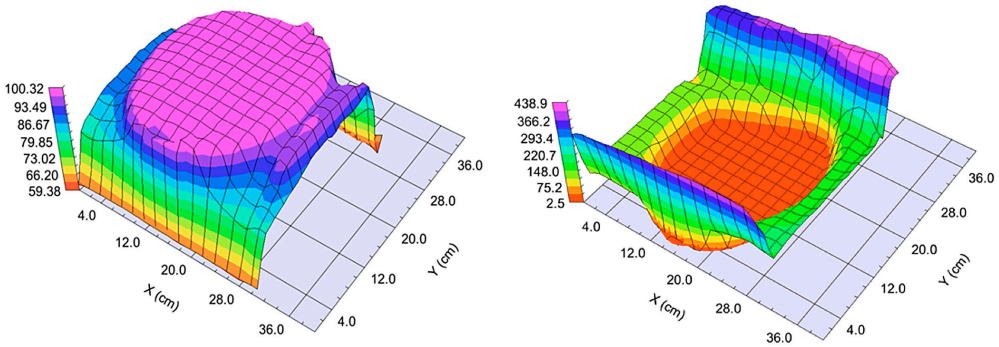

Figure 2 *Thickness map of a nominally 100 nm sample of a 300 mm diameter SiON-on-Si wafer (with automatic scale, left). The mean squared error (MSE) map shows the area of the sample (right).*

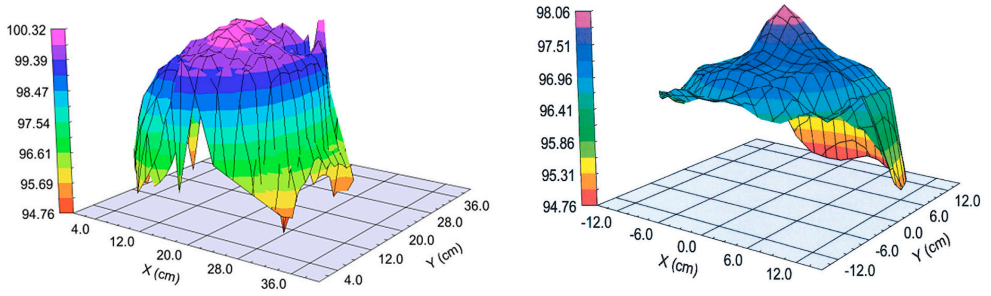

Figure 3 *Thickness map with the same limited scale as the results of checking spectroscopic ellipsometry measurements by a Woollam M2000DI ellipsometer (1 color = 0.29 nm).*

Fabrication of Genetically Modified Bacterial Filament Coatings to Develop Sensor Surfaces for Detecting Water Pollution

(M-ERA.NET WaterSafe/No. 39/2016, OTKA NN 117849, OTKA NN 117847, OTKA K 115852 and EU (ERDF) INFRANANOCHEM No. 19/01.03.2009)

J. Nádor, B. Kalas., A. Saftics, L. Illés, B. Kovács, Cs. Moldován, A. Romanenko, M. Gartner, M. Fried, F. Vonderviszt, and P. Petrik

In modern technology the developments in environmental areas become more important and current. Freshwater stocks and pollution are in the most relevant topics, as they can be crucial in the future of humankind. Within the "WaterSafe" international project, we take part in the development of a device for detecting various water pollution molecules (mainly heavy metals and nitrogen oxide ions). The surface of the disposable sensor can be a mix of dielectrics, nanostructures or genetically modified bacterial flagellar filaments (FF) that have specific binding sites for specific molecules. The adsorption of the target molecules to the immobilized filaments induces a change in the conductance of the electrode which can indicate the presence of the pollution.

The main aim of our group is to create the sensing layers by immobilizing the FFs on the gold electrode of the sensor surface, for which we applied two different methods. Either genetically modified FFs were used, which have an enhanced number of thiol groups on their surface in order to create covalent interactions with the gold surface. Or we used unmodified wild type FFs, and applied chemical crosslinker DSP (dithiobis(succinimidyl propionate)) molecule for immobilizing the FFs to the gold surface.

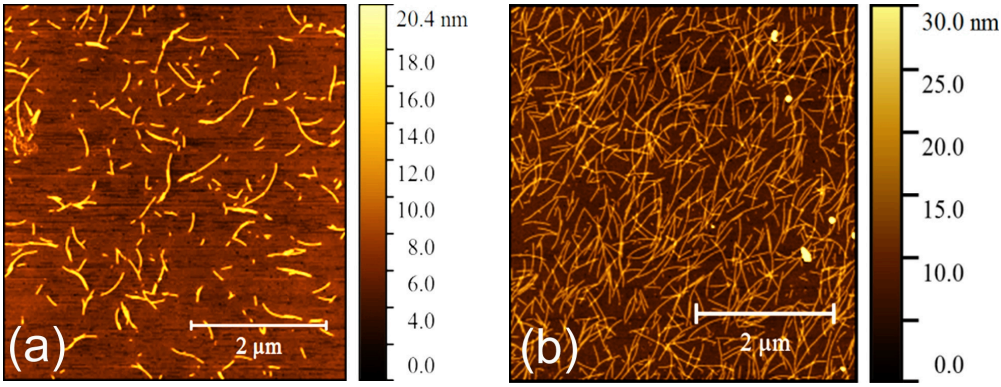

Figure 1 *AFM images of flagellar filaments immobilized on gold coated glass substrates applying* ***(a):*** *genetically modified filaments with an enhanced number of thiol-groups on their surface and* ***(b)****: wild type filaments immobilized by DSP crosslinker molecules.*

Both types of the FFs were immobilized on various surface nanostructures. Using in situ plasmon enhanced spectroscopic ellipsometry, AFM, SEM and ex situ scanning ellipsometry, we have shown that those nanosctructures (e.g. titanate nanotubes, TiO_2 nanoparticles and ZnO nanorods) can facilitate the adsorption of protein.

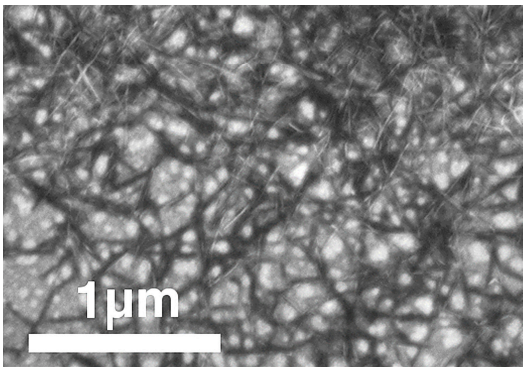

Figure 2 *SEM image of a flagellar filament layer (dark fibers) prepared on titanate nanotube coating (lighter fibers) on gold surface.*

Investigation of wetting processes by the capillary bridge probe technique

N. Nagy

The research aims the development of a highly sensitive measuring method which enables to characterize flat solid surfaces by accurate determination of the contact angle even in case of very low or high contact angles. The proposed capillary bridge probe method is based on the capture and analysis of the shape of the liquid bridge formed between the cylindrical probe and the investigated surface, and on the measurement and analytical calculation of the capillary force. Advancing and receding contact angles can be determined by changing the distance between the probe and the surface even in case of very low contact angles.

The appropriate measuring setup was constructed and built up. The main advantage of the method emanates from the use of the probe: the contact angle can change continuously at the edge of the probe oppositely to the recent apparatuses. A further uniqueness of the construction is the closed sample chamber providing close-to-saturated atmosphere.

The evaluation is based on the accurate image analysis of the liquid bridges and on the analytic calculation of their properties during one approach-retraction cycle. The evaluation program was implemented for nodoid-shaped bridges, i.e., for surfaces of contact angle less than 90°.

Close to the ideal surfaces (freshly cleaned glass slides, SiO_2, Si_3N_4) and surfaces with significant hysteresis are analyzed (Al_2O_3, GaO_2) and the contact angle values are compared to the results of the sessile drop method. Furthermore, the behavior of

these r-ϑ capillary bridges are investigated first and compared to the statements and models of the literature on ϑ-ϑ capillary bridges between identical planes.

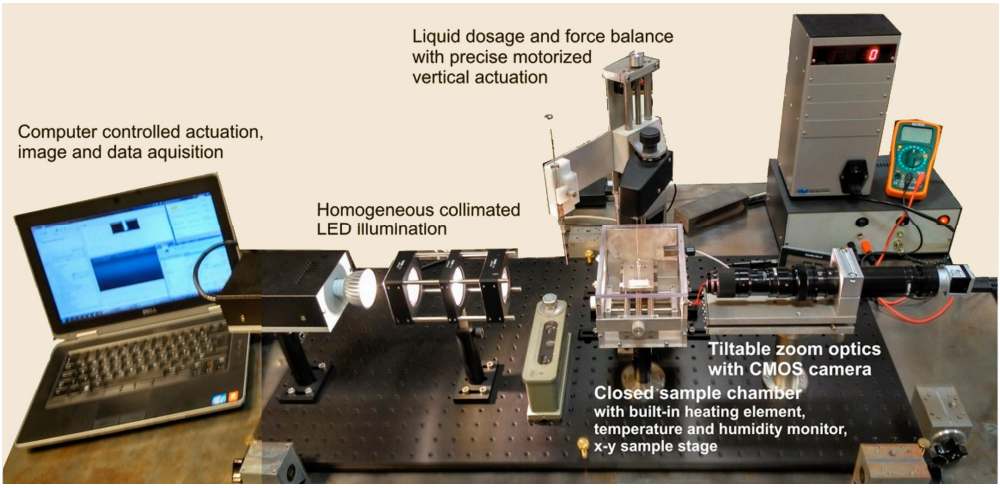

Figure 1 *The accomplished apparatus for highly sensitive characterization of solid surfaces by the sessile drop or by the capillary bridge probe method, furthermore for investigation of r-ϑ capillary bridges.*

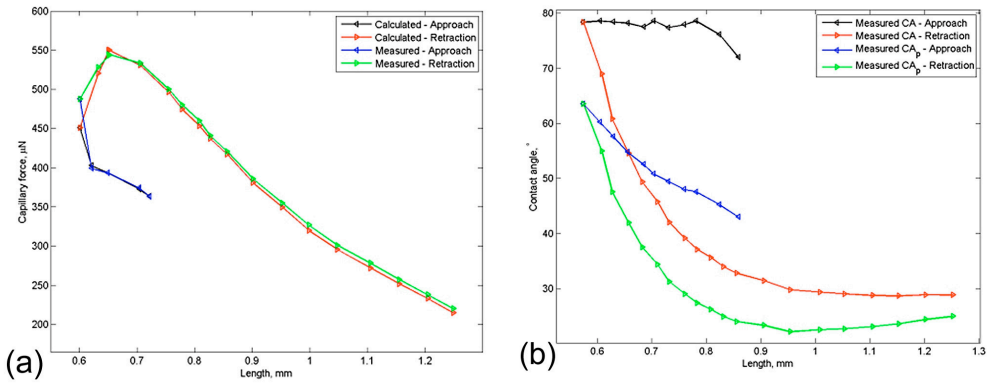

Figure 2 *Measured and calculated capillary force* ***(a):*** *and the determined contact angles* ***(b):*** *on the investigated surface and on the probe (CA_p) in the function of bridge length during one approaching-reversal cycle, measured on a GaO_2 thin film with high hysteresis.*

Optical and structural characteriyation of Ge clusters embedded in ZrO_2

(OTKA K 115852, M-ERA.NET WaterSafe No. 39/2016, OTKA NN 117847)

E. Agócs, Z. Zolnai, A. K. Rossal, J. A. van den Berg, B. Fodor, D. Lehninger, L. Khomenkova, S. Ponomaryov, O. Gudymenko, V. Yukhymchuk, B. Kalas, J. Heitmann, and P. Petrik

Recently, a promising application of Ge-NCs embedded in ZrO_2 matrix for nanocrystal-based memory devices has been shown, since Ge has a smaller band gap than Si, and ZrO_2 has a higher k value than SiO_2 that increases the electric field across the tunneling oxide. This material system may also be interesting for third-generation solar cells, since Ge has a higher exciton Bohr radius. Therefore, a stronger quantum confinement effect is expected than for e.g. Si nanocrystals, and the band gap can better be adjusted.

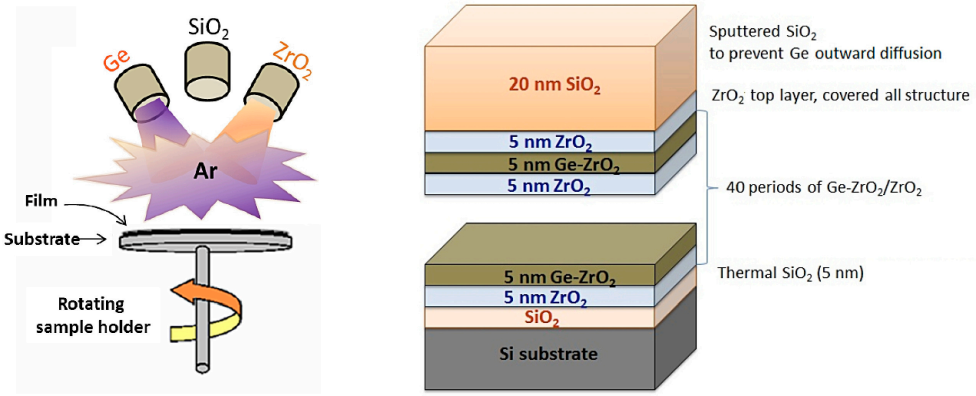

Figure 1 *Shematic graph about the sample preparation (left), and the structure of samples (right).*

The present study has two major aims. First, to develop and to test proper optical models to determine Ge nanocrystals in a single Ge-rich-ZrO_2 layer as well as in a multi-layer structure. Second, to demonstrate the validity of this method by the optical investigation of the evolution of the samples structure caused by annealing.

The samples were fabricated using a radio-frequency (RF) magnetron sputtering system equipped with a confocal arrangement of 3-inch targets (Ge, ZrO_2 and SiO_2) (Fig 1). The ellipsometric measurements were performed by means of a Woollam M-2000DI rotating compensator ellipsometer. Raman scattering spectra were excited with a 488.0 nm line of an Ar^+ laser and recorded using a LabRam HR800 micro-Raman system equipped with a Peltier-cooled CCD detector.

References for both ZrO_2 and pure Ge were determined on single-layer samples prepared with the same deposition conditions as those used for multilayer structures.

The dielectric function of the ZrO_2 component was described by the Cauchy parametrization (Result: A = 1.988, B = 0.0092 μm^2 and C = 0.000812 μm^4.).

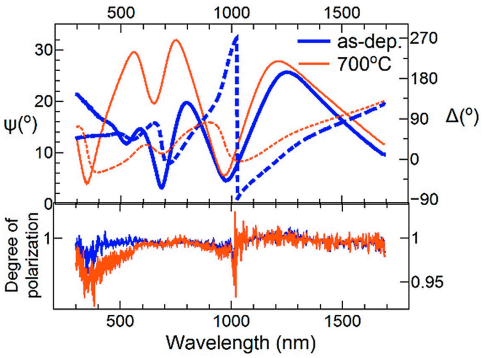

Figure 2 *Measured Ψ (solid lines) and Δ (dashed lines) spectra for Sample Ge-ZrO_2 annealed at 700 °C as well as without annealing.*

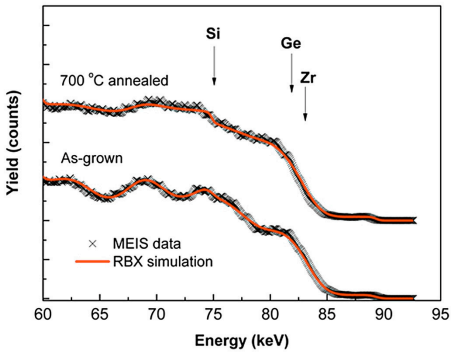

Figure 3 *Medium Energy Ion Scattering spectra and the corresponding RBX simulations of as-deposited and annealed Ge-ZrO_2 samples.*

References for both ZrO_2 and pure Ge were determined on single-layer samples prepared with the same deposition conditions as those used for multilayer structures. The dielectric function of the ZrO_2 component was described by the Cauchy parametrization (Result: A = 1.988, B = 0.0092 μm^2 and C = 0.000812 μm^4.). Germanium requires more complex parameterization of the dielectric function for the modelling. For the as-deposited Ge layer the Urbach-Cody-Lorentz parameterization was used. The superlattice samples have been modeled using either a single-layer (MsL) or a multi-layer (MmL) approach. Both of them utilize a layer stack of Si(substrate) / SiO_2 / SL / SiO_2, whereas the 'MsL' and the 'MmL' models use a Bruggeman-Effective Medium Approximation (B-EMA) layer and 40 pairs of B-EMA layers, respectively, describing the superlattice (SL) structure (Fig. 1 right). In the B-EMA layer, we used the Ge and ZrO_2 references determined above.

It has been shown that ellipsometry offers a characterization method of Ge/ZrO_2 and Ge-rich-ZrO_2/ZrO_2 multi-layer structures with high sensitivity. The as-deposited structure was successfully modeled using reference optical constants determined from single-layer characterizations. It has also been shown that the surface region (several layer-pairs from the top) can sensitively be measured by Medium Energy Ion Scattering (MEIS), that revealed substantial diffusion during annealing.

Ellipsometric and X-ray spectrometric investigation of fibrinogen protein layers

(TÉT-12-DE-1-2013-0002, OTKA K 115852, M-ERA.NET WaterSafe No. 39/2016, OTKA NN 117849)

B. Kalas, B. Pollakowski, A. Nutsch, C. Streeck, J. Nádor, M. Fried, B. Beckhoff, and P. Petrik

The quantitative measurement of thin protein layers is of primary importance from both the metrology point of view and for many applications. Bovine fibrinogen monolayers on thin gold films and glassy carbon substrate were investigated using grazing incidence X-ray fluorescence (GIXRF) and spectroscopic ellipsometry (SE). The aim was to determine the amount of protein and to develop models and references for the SE measurement. Both methods were capable of measuring protein amount in the range of μg/cm^2 with a sensitivity below 10%, which suggests the use of both techniques as complementary, combined methods. To do it with a high confidence, the lateral uniformity and the stability of the layers during transportation has to be investigated in more detail in the future. The surface mass density and homogeneity were determined using X-ray and optical methods. Reference refractive indices have been measured and models have been developed in order to measure the thickness and the uniformity of the protein films quickly and accurately on surfaces. A fair agreement was found between the quantities determined by grazing incidence X-ray fluorescence and spectroscopic ellipsometry, however, the lateral homogeneity might also influence the results considerably.

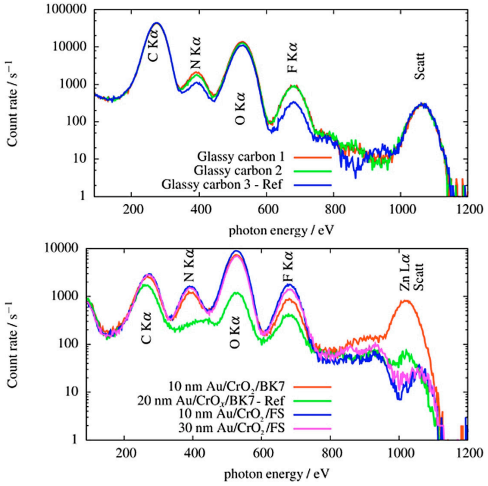

Figure 1 *GIXRF spectra are exhibited recorded at a photon energy of about 1060 eV. Top: Spectra measured at glassy carbon. Bottom: Spectra measured at fused silica and glass substrate.*

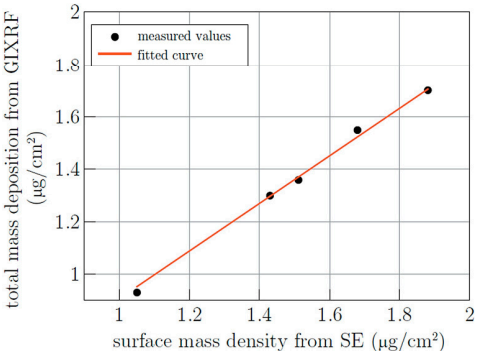

Figure 2 *Comparison of the GIXRF and the SE results using the Cauchy expression. The data show a good agreement between the two methods, within their measurement errors.*

Vegard's-law-like dependence of the activation energy for blistering on the Si/Ge ratio in hydrogenated a-Si_xGe_{1-x}

M. Serényi and A. Hámori

The relationship between the activation energy of blistering and the Si-to-Ge ratio has been determined in hydrogenated amorphous a-Si_xGe_{1-x} by employing layers deposited by radio frequency sputtering. To this aim the blistering activation energy was determined in several samples with different compositions, including x=0 and x=1. Each sample was submitted to heat treatment up to the temperature where the onset of blistering was observed by change of the surface reflectivity. A linear dependence of the activation energy on x has been established similar to the Vegard's law. The experimental result is supported by reaction kinetics modeling. It is suggested that the key step for the formation of blisters is the breakage of the SiH and GeH bonds. The related energetic reaction leading to the formation of H_2 molecules in a-Si_xGe_{1-x} follows a linear law as a function of the x composition similarly to the activation energy.

The activation energy E_a for blistering was determined by Arrhenius plots reporting the minimum time needed to make the blisters optically visible as a function of the temperature. The hydrogenated samples have been heated in air on a plate at constant temperature while illuminated by a 3 mW He-Ne laser beam with a diameter of 3 mm and angle of incidence of 60° which resulted in an elliptically illuminated sample area with size of about 3x6 mm^2 (Fig. 1). The reflected light fell onto a Si PIN detector blended with diameter of 3 mm. During the heating process the specular reflection transforms into a spread one, which has a dominant directional component that is partially diffused by surface irregularities. The onset of blistering was identified with the decrease of the reflected intensity caused by the outgoing rays reflected at many different angles. The activation energy Ea of the a-Si_xGe_{1-x} is displayed in Fig. 2 as a function of the x composition.

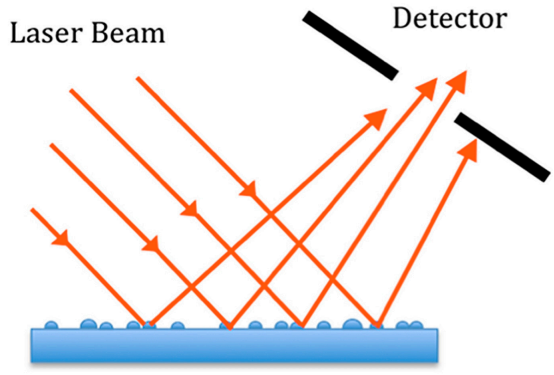

Figure 1 *Sketch of the experimental procedure for detecting the onset of blistering.*

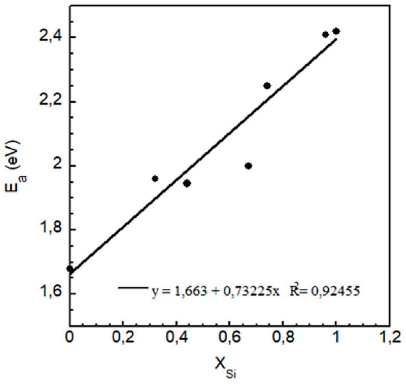

Figure 2 *Blistering activation energy $E_a(Si_xGe_{1-x})$ in Si_xGe_{1-x} as a function of x.*

Porous Si degradation in physiological solution

B. Fodor, B. Kalas, T. Defforge, M. Fried, G. Gautier, and P. Petrik

Cooperation is being continued with the GREMAN laboratory of the University of Tours. Our long-term goal is the development of an accurate and selective biosensor. For this purpose, in situ ellipsometric characterization can be performed with the help of a flow cell, where the solution containing the particles would be adsorbed onto the substrate material, causing a detectable variation in the optical properties of the surface. Silicon-based nanostructured frameworks could be used as adsorbing substrates to increase the sensitivity and selectivity of proteins. However, without adequate surface treatment, these materials remain unstable in physiological solutions, i.e. degradation occurs. Therefore, the degradation in different solutions must be investigated, and appropriate stabilizing methods should be found by applying different surface chemistries (oxidation, carbonization). In a first step, we investigated the degradation by a flow of PBS solution (7.4 pH) for ~90 min. In Fig. 1, the effect of the degradation can be seen on porous silicon with an initial porosity of 68%. It is yet unsure if the collapse of the skeleton frame occurs during the *in situ* experiment or because of the drying step, but ellipsometric signal intensity was lost after 80 min.

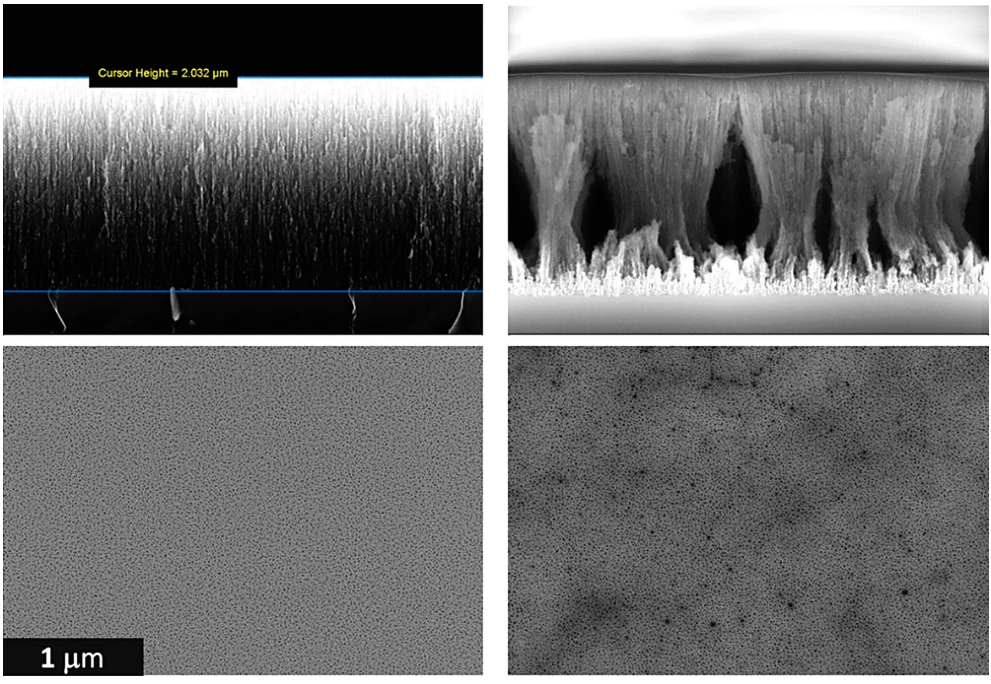

Figure 1 *SEM images showing the degradation effect before (left) and after (right) a 100 min buffer solution flow experiment in a cross-sectional (top) and a top (bottom) view.*

Microtechnology Department

Head: Dr. Gábor BATTISTIG, D.Sc., senior research fellow

Research Staff

- Zsófia BAJI Ph.D. (on maternity leave)
- István BÁRSONY, Member of HAS
- Gábor BATTISTIG D.Sc.
- Orsolya BÁLINT-HAKKEL Ph.D.
- László DÓZSA Ph.D.
- Csaba DÜCSŐ Ph.D.
- Péter FÖLDESY Ph.D.
- Péter FÜRJES Ph.D.
- Zoltán HAJNAL Ph.D.
- Nguyen Quoc KHÁNH, Ph.D.
- István LUKÁCS Ph.D.
- György MOLNÁR Ph.D.
- Andrea Edit PAP Ph.D. (part time)
- Anita PONGRÁCZ Ph.D. (part time)
- Vilmos RAKOVICS Ph.D.
- István RÉTI Ph.D.
- Zoltán SZABÓ Ph.D.
- János VOLK Ph.D.
- Zsolt ZOLNAI Ph.D.

Technical Staff

- János FERENCZ (engineer)
- Levente ILLÉS (engineer)
- Csaba LÁZÁR (engineer)
- Petra HERMANN (Engineer)
- Róbert HODOVÁN (engineer)
- András STRASZNER (engineer)
- Erika TUNYOGI (engineer)
- Katalin VERESNÉ VÖRÖS (engineer, retired)
- György ALTMANN (technician)
- Gabriella BÍRÓ (technician)
- Tibor CSARNAI (technician)
- Magda ERŐS (retired, part time)
- Attila NAGY (Technician)
- Károlyné PAJER (technician)
- Csilla ARIAS-SOTONÉ FARAGÓ (technician)
- Attila NAGY (technician)
- Magda VARGA (technician)

Postgraduate students

- Zsófia BÉRCES
- Ferenc BÍRÓ
- Máté TAKÁCS
- Eszter HOLCZER
- Eszter TÓTH
- János RADÓ
- Anita ZÁTONYI
- Ágoston HORVÁTH
- László PÓSA
- Anita ZÁTONYI
- Saeedeh SOLEIMANI

Task of the Microtechnology Department is

Fundamental research on:
- novel sensing principles;
- novel materials and nanostructures;
- novel 3D fabrication techniques.

Research and development of physical, chemical/biochemical sensors, and integrated systems:
- **MEMS** – R&D on gas sensors, 3D force sensors, thermal sensors, CMOS compatible and related techniques.
- **BioMEMS** – Development of novel microfluidic and bio-electrode systems, their application in new fields of biochemistry.
- **NEMS** – Synthesis and characterization of quasi-one-dimensional semiconducting nanostructures, semiconductor nanodevices, their integration into functional sensors, optoelectronic and photovoltaic devices.

Modelling, structural and device characterization methods available:
- Electrical characterization;
- Thermo-mechanical characterization;
- Optical characterisation;
- Scanning Microprobes;
- SEM, TEM, EDX;
- Ion beam analysis methods;
- Spectroscopic Ellipsometry.

The Department runs two clean labs (300 m^2 + 160 m^2 - Class 100-10000) comprising a complete Si-CMOS processing line and a mask shop, unique facility in Hungary. The technology allows to manufacture layers, patterned structures and devices with line resolution of 1 μm by optical and down to ≈10 nm by e-beam lithography on 3" and 4" Si and glass wafers.

Competences (available as service for academic, industrial partners and customers):
- High temperature annealing, diffusion and oxidation; Rapid Thermal Treatment;
- Low Pressure Chemical Vapour Deposition of poly-Si, SiO_2 and Si_3N_4 layers;
- Low Temperature Chemical Vapour Deposition;
- Plasma Enhanced Atomic Layer Deposition;
- Physical Thin Film Depositions – Electron beam evaporation, DC and RF Sputtering;
- Ion implantation;
- Reactive Ion Etching, Deep Reactive Ion Etching;
- Photolithography with back-side alignment and Nanoimprinting;
- E-beam lithography;
- Nanopatterning, deposition and etching by Focused Ion-Beam;

- Wafer-bonding;
- Wet chemical treatments;
- Electro-chemical porous Si formation;
- Liquid Phase Epitaxy of III-V compound semiconductors;
- Mask design, laser pattern generator;
- Polymer (PDMS, SU8, Polyimide) structuring by photolithography and micro-molding techniques,
- Chip dicing, packaging especially for sensor applications;
- Materials and structural analysis & characterization:, SEM, FIB, EDX, Atomic Force Microscopy, Electrochemical Impedance Spectroscopy, Stylus Profiler;
- Electrical and functional modelling and characterization.

For detailed information please visit our web-sites:
www.mems.hu, **www.biomems.hu**, **www.nems.hu**
or contact us by e-mail: **dragon@mfa.kfki.hu**

MEMS

Activity leader: Cs. Dücső
Group members: Z. Baji, I. Bársony, G. Battistig, P. Földesy, P. Fürjes, Z. Hajnal, G. Molnár, A.E. Pap, V. Rakovics, J. Radó, Z. Szabó, I. Réti, Z. Zolnai, F. Biró, M. Takács (M. Szappanos, N. Nyirfás - MSc Students)

Projects:

- OTKA K 109674 – Graphen based terahertz modulators (2013-2017)
- OTKA K 108869 – Wide band-gap semiconductors (2014-2017)
- OTKA PD 116579 – ZnO és Ga_2O_3 nanostructures by ALD (2015-2018)
- OTKA K 112114 – Combined micro- and nanotechnology methods and analytics – from patterning to applications (2014-2017)
- EU FP7- ICT-611019 - High-resolution fingerprint sensing with vertical piezoelectric nanowire matrices (PiezoMAT) (2013-2017)
- ENIAC 2013-1 621278 - Intelligent Catheters in Advanced Systems for Interventions (INCITE) (2014-2017)
- NVKP_16–2016-0018 - Up-to-date functional materials for autonomous sensor nodes and sensor networks (KoFAH) (2016-2019)
- NVKP_16-2016-0014 – Materials research studies on zirconium Participants: László Dózsa and György Molnár)
- Italian-Hungarian joint program (CNR-IMEM – MTA EK MFA) - Synthesis, characterization and study of semiconducting materials for energy conversion, sensors, electronics and medical applications (2016-2019)
- VEKOP-2.3.3-15-2016- 0001 – "Updating infrastructure of microtechnology to reach compatibility with EU" (2017-2018)

Development of micro gas sensors

Solid-state gas sensing microstructures were developed aiming at the detection of hydrocarbons below their lower explosion limits as well as for measuring NH3 and H2S in the ppb - 00ppm range.

Degradation mechanisms of microhotplates operated above 500°C

In calorimetric sensors for hydrocarbons a high T_c Pt micro-heater is coated with catalyst to initiate combustion of hydrocarbons in the presence of oxygen. The generated chemical reaction heat modifies the temperature, thereby the heater resistor. The transduction principle is based on resistance read-out. Our previous results show that the most efficient catalyst is Pt, however, the minimum temperature required is 500°C and 700°C for LPG and CH_4, respectively. A detailed investigation revealed the degradation mechanisms of the Pt filament. We found three phenomena of

different activation energies leading to the continuous resistance change and finally the fatal degradation. First the TiO_2 adhesion layer beneath the Pt filament forms TiO_2 nanocrystals which penetrate the bulk of Pt. Parallel to the well-known electromigration effect, thermally driven Pt migration dominates in regions, where the local temperature exceeds ~850-900K and the temperature gradient approx. 0.5K. The coincidence both of thermo- and electromigration driven by temperature, and potential gradients precisely determine the position of the filament rupture. The phenomenon was proven by statistical analysis of experimental measurements. We determined the operation limits of the filaments and concluded that highest allowable temperature for a device expected being operational at least for one year is ~540°C (Fig.1).

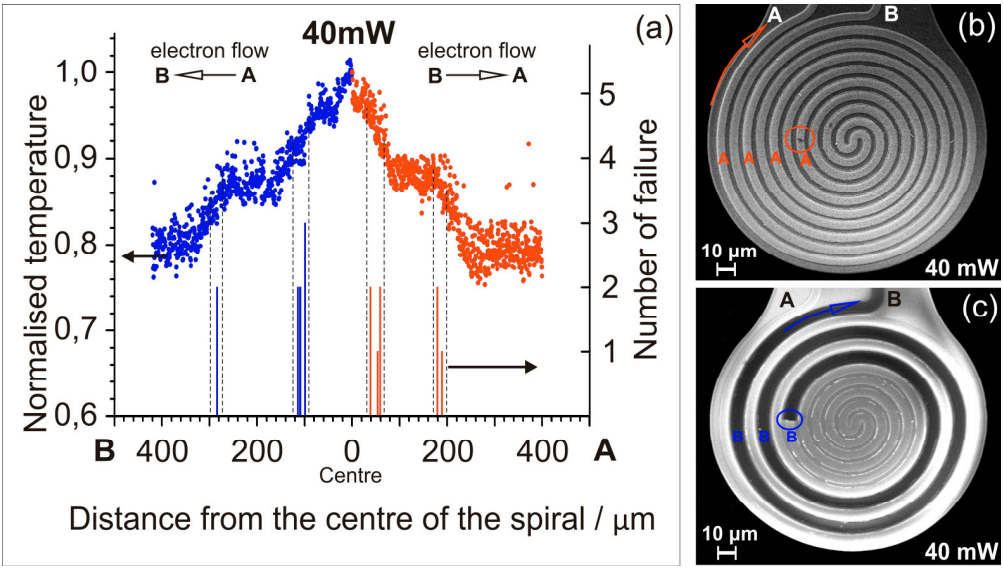

Figure 1 *Graphical illustration of correlation between the temperature distribution and breakdown positions. Graphs on the left indicate the temperature profile as a function of the distance from the centre point along the filament as measured by pyrometry for 40 mW heating powers The number and position of ruptures for each of the hotplates are marked by bars. Corresponding SEM micrographs are shown on the right. Potential contrast mode image better reveals the location of the rupture. Blue and red colours denote the spiral arms, the electron flow direction (blue and red arrows) are indicated.*

We also elaborated ALD technique to deposit 2-4 nm sized Pt nano-catalyst in the porous alumina surface formed by electrochemical etching of thin Al layer on top of the hotplate. Functional tests revealed another degradation mechanism, i.e. the coalescence of Pt nanocrystals at elevated temperature, and the thermo-migration of Pt due to the inhomogeneous temperature profile of the hotplate. Pt migrates in radial direction from the hottest centre towards the colder perimeter of the hotplate leading to the sensitivity loss.

From the above degradation mechanisms we conclude that the investigated meander and coil-type filament heated hotplates covered with ALD Pt catalyst are capable to measure LPG (T_{max}<540°C), but for methane (T_{min}>700°C) the lifetime of the device is ~160hrs only at continuous loss of sensitivity. The best way for improvement is definitely to apply a new catalyst active at reduced temperature and to use pulse mode operation. Nevertheless, some improvement in lifetime is expected from novel geometric and possibly material design.

Conductivity type sensors for NH_3 and H_2S

Nanostructured WO_3 layers were synthetized, sensitized and characterized for their performance in detection of NH_3 and H_2S. In 2016, we elaborated a hydrothermal method for formation of hexagonal WO_3 nanorods and demonstrated the efficiency of Au and Pt doping. Reliable detection of H_2S down to 25 ppb was demonstrated.
As the drop deposition of the separately synthetized sensing layer is a bottleneck in reproducible mass production, thus, we elaborated wafer level processing methods to form uniform, nanostructured WO_3 layer on top of the microhotplates. Two alternatives were investigated; sol-gel process with spin-coating and electrochemical (anodic) etching of thin W layer. The sol-gel process results in sponge-like porous structure with 12-20 nm characteristic pore size, whereas 50-70nm diameter pores grown perpendicularly to the surface can be formed by the electrochemical process. Both techniques were integrated in the MEMS sequence using lift-off technique or selective anodization for lateral patterning. ALD Pt was deposited for sensitizing and the performance of all WO_3 structures was investigated. The operation temperature of the best sensors was found between 180-220°C. The electrochemically processed sensors doped with 2-4 nm Pt nanoparticles exhibited the best performance in terms of sensitivity and stability as well as regarding response and recovery time (Fig 2).

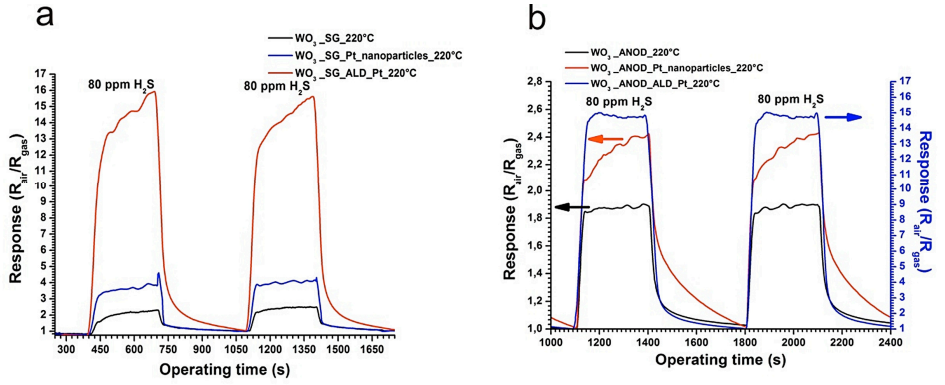

Figure 2 *Transients of sol-gel* ***(a)****, and electrochemically* ***(b)*** *formed sensors for exposure of H_2S.*

In summary, we conclude that by low enough operation temperature we meet the sensor standards in terms of the hotplate stability and read-out dynamics. By proper

selection of WO_3 nanostructure and sensitizers both NH_3 and H_2S can be detected in the 5-100 ppm range. ALD gold doping of electrochemically formed mesoporous WO_3 promises dynamic, reliable H_2S detection far below the ppm level.

Development and production of Near Infrared LEDs

This year, the activity was focused on further improvement of the multiple wavelength GaInAsP/InP NIR light source reported in 2016. Following structural/processing improvements demonstration activities were intensified to establish a cooperation-network for exploitation of the application potential of NIR LEDs.
Appropriate measures to increase our production capacity for the standard single wavelength, and the novel multiple wavelength NIR LED design were introduced.

BioMEMS

Activity leader: P. Fürjes
Group members: O. Bálint-Hakkel, Cs. Dücső, P. Földesy, Z. Hajnal, E. Holczer, E.L. Tóth, J. Radó (A. Füredy, M. Szappanos, N. Nyírfás, A.B. Tóth, B.V. Farkas, V. Kálmán – MSc. students)

Projects:

- ENIAC 2013-1 621278- Intelligent Catheters in Advanced Systems for Interventions (2014-2017)
- OTKA CK 83821 – Preparation of microchannels by proton-beam micropatterning and their application in Lab-on-a-chip devices
- VKSZ_14-1-2015-0004 – Development of Multiparameter Point of Care in vitro diagnostic systems
- GINOP-2.3.2-15 – Application of chip-technology for the improvement of the success rate in human in vitro fertilisation
- VEKOP-2.2.1-16-2017-00001 - Rapid urine bacteria analyzer

Main task of the BioMEMS activity is the support of the development of biosensors, biointerfaces and microfluidic systems in micro- and nanofluidical, bioanalitical and medical diagnostics.

Polymer microfluidic systems for medical diagnostics

Precise and fast Point of Care, PoC monitoring of disease related blood protein marker levels could be crucial in effective therapies. Due to the specific tools and novel microtechnology processes the cost-effective, complex but miniaturised analytical systems, such as Lab-on-a-Chip (LoC) and microfluidic devices have

become available and can be implemented in the overall sample analysis from the preparation to the molecular diagnostics. The use of biological sample requires bio-inert surface properties with minimized non-specific adsorption and coagulation in the channels. The perspective of our work is to develop a polymer based microfluidic cartridge suitable to autonomously controlled sample transport and preparation of integrated bioanalytical devices.
Accordingly, microfluidic system was designed and manufactured for whole blood or plasma transport by precisely controlled sample rate. These autonomous sample transport systems can be integrated into PoC Lab-on-a-Chip based diagnostic devices. The developed systems are planned to be applied for detection of inflammation and cardiovascular diseases, in cooperation with "Diagnosticum Inc." and "77 Elektronika Ltd.".

Characterisation of blood protein adsorption on modified PDMS surfaces

Polymer based microfluidic sample transport system with multiple functions was developed for application in bioanalytical devices detecting blood protein biomarkers or cells. Significant flow controlling subparts of the overall microfluidic system were designed, fabricated and characterised in the function of different surface modifications and microscale geometries. In order to fulfil the requirements the polydimethylsiloxane (PDMS) base material was modified by embedding PDMS-b-PEO molecules into the PDMS matrix. PDMS-b-PEO molecules change the inherent hydrophobicity of the polymer ensuring adequate capillary pressure for self-driven transport and affecting also the level of the non-specific protein adsorption simultaneously.
In order to modify the surface characteristics of PDMS, PDMS-b-PEO block-copolymer was added in different concentrations into the non-polymerized raw mixture. The embedded copolymer molecules can not only enhance the wettability of the surface, but also reduce the non-specific protein adsorption, significantly and permanently. The embedded molecule concentration dependent surface adsorption of typical human blood proteins (HSA, IgG, fibrinogen) were characterized by fluorescent microscopy and BCA colorimetric protein assay in the function of the modified PDMS surfaces. The applied methods enable quantitative determination of the relative and absolute amount of irreversibly bonded proteins. Based on the results material compositions were defined in order to avoid the non-specific adsorption of different proteins in autonomous microfluidic systems. Embedding non-ionic surfactants in the PDMS effectively changes the surface characteristics of the material. The non-specific protein adsorption can also be significantly decreased by the developed surface modification method. By embedding PDMS-b-PEO molecules above 0.5V/V% concentration the irreversible protein binding can be completely terminated. (Fig. 1)

Fabrication of hybrid microfluidic system on transparent substrates

High complexity polymer or hybrid microfluidic structures open the way towards fabrication of cheap, disposable analytical cartridges. Glass and polycarbonate were considered as primary transparent substrate material for metal (Au, Pt) electrode deposition, whereas the microchannels were formed in multi-layered SU-8 negative photoresist. PDMS layer was proposed as cover layer for proper sealing and sample inlet formation (Fig. 2).

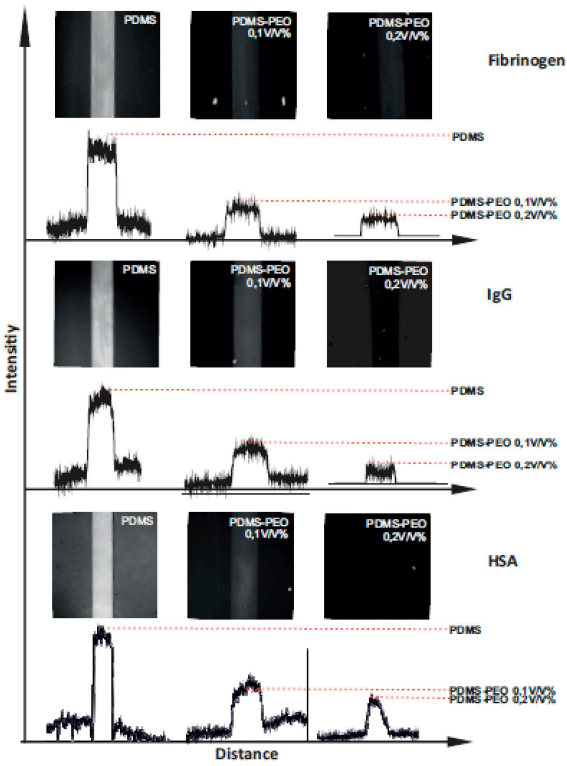

Figure 1 *Recorded fluorescent intensities indicating the presence of irreversibly bonded fluorescent labelled protein molecules on the microchannel surfaces.*

Our aim was to modify both the SU-8 and PDMS surface in order to form covalent bond between the substrates. According to the literature the feasible SU-8 / PDMS binding is evolving through the reaction of the epoxy groups and amino groups, however our attempts to reproduce the published recipes failed in most cases. Several bonding strategies were characterized in terms of their adhesion and stability, considering plasma processes (O_2, N_2) and silanization treatments. Chemical composition of the SU-8 and PDMS bonding surfaces were analysed by sensitive analytical methods in molecular level. The appropriate materials and processes were defined to achieve reliable formation of complex hybrid polymer microfluidic systems. Accordingly, SU-8 series can be bonded to PDMS layer after silanization of its surface and oxygen plasma treatment of PDMS. This method enables to form integrated hybrid microfluidic cartridge on transparent substrates.

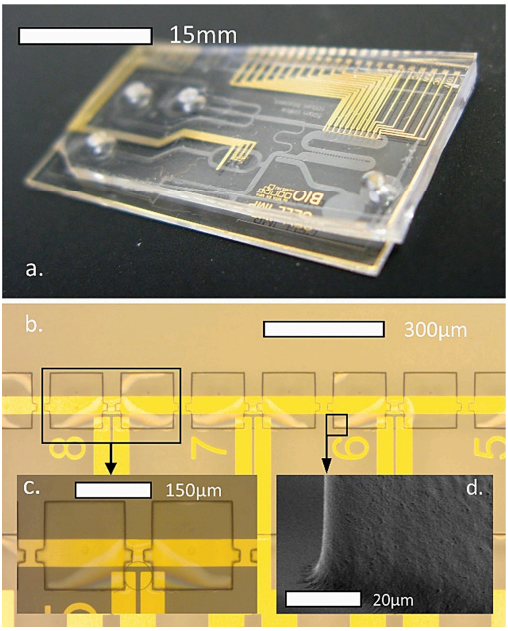

Figure 2 *Metal (Au) electrodes integrated in SU-8 based hybrid microfluidic system* ***(a)****. For proper alignment, electric insulation and transparency the channels are formed in multi-layered SU-8* ***(b, c)****. SEM view presents the interface between the thin insulation and the thick channel forming SU-8 layers* ***(d)****.*

Cell and particle manipulation and screening in microfluidic systems

The rapid development of microscale diagnostic (Lab-on-a-Chip) devices has underlined the importance of microfluidics enabling fast and effective preparation and analysis of liquid samples. Nevertheless, due to the governing physical phenomena on microscale, classical sample preparation methods might become challenging, such as the effective mixing of fluids as well as the size-dependent separation of corpuscles and their sorting or filtering from the liquid samples. This leads to the development of novel microfluidic structures based on the physical laws of this size domain.

Modelling and characterisation of cell and molecule advection in continuous microfluidic systems

Lab-on-a-Chip applications often require separation of particles of specific properties e.g., shape, size, density or other physical, chemical or biological properties. Microfluidic chip with special channel layout was developed for hydrodynamic particle sorting by their cell size or density for optical scattering based pollution monitoring applications. Finite Element Method (FEM) was used to model the hydrodynamic properties and the behaviour of the microfluidic system including their effects on particle movement. COMSOL Multiphysics was used to calculate the laminar flow field and particle trajectories having different parameters along the channel. The microfluidic chip was fabricated by fast prototyping using SU-8 photoresist and polydimethylsiloxane (PDMS) for replica moulding. The developed

chip was evaluated using fluorescent microscopy with two particles of 10 and 16 µm diameters labelled with different fluorescent dyes. Measurement was in good agreement with the modelling predictions and successful size-dependent particle sorting was demonstrated.

Particle separation and trapping in micromagnetic separation (MMS) systems

Bioanalytical methods based on detection of receptor / marker protein interactions are widespread in today's clinical diagnostics. Determination of specific receptor molecules with high affinity (such as antibodies or artificial aptamer molecules) is a key issue of assay development. Aptamers can recognize a wide range of targets, from ions to complex cellular macromolecules, although their synthesis by in-vitro SELEX (Systematic Evolution of Ligands by Exponential Enrichment) method is a time and money consuming process. Using microfluidic SELEX method, the aptamer selection process can be improved and accelerated, and pave the way for development specific diagnostic devices. The aim of this work is to adapt, study, and optimize magnetophoretic separation and trapping methods in microfluidic systems to be applied in mSELEX process. Microfluidic Magnetic Separation (MMS) devices use the effective magnetophoresis based magnetic bead manipulation by applying microfabricated paramagnetic patterns to locally amplify the magnetic field. With the integration of ferromagnetic (FeNi) microstructures into a microfluidic platform the lateral magnetic field gradient can be altered and locally enhanced, thereby enabling the precise manipulation of small amount of magnetic beads.
Different micromagnetic separation (MMS) systems with various ferromagnetic pattern and microfluidic channel geometry were designed, modelled, fabricated and characterised. The studied microfluidic structures were manufactured by the combination of traditional micromachining and soft lithography methods in heterogeneous glass-polymer (PDMS, polydimethylsiloxane) systems. Different micromagnetic separation (MMS) systems were characterised considering their separation and trapping parameters using superparamagnetic beads.

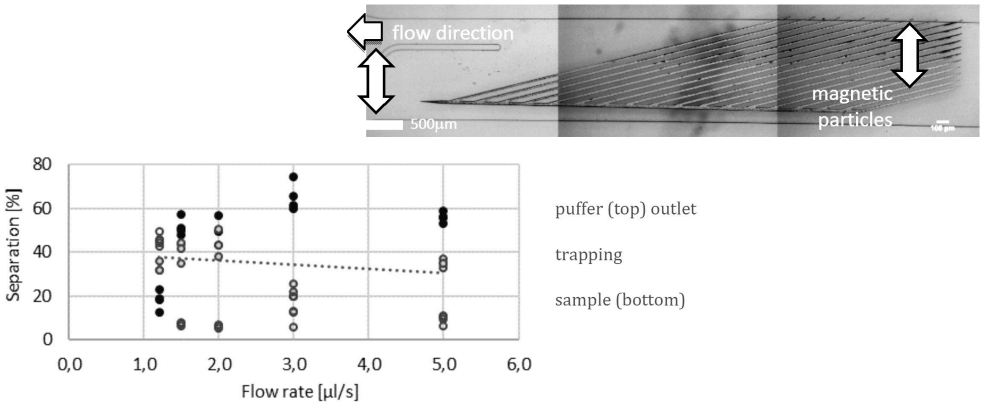

Figure 1 *MicroMagnetic Separation structure in the microfluidic channel (top) and the flow rate dependent separation efficiency (bottom).*

MMS systems were proved to be applicable for temporal (trapping) and spatial separation of superparamagnetic particles. Based on the experiments an efficient micromagnetic separation architecture was proposed including the special layout of the ferromagnetic microstructure and the geometry of the fluidic system.

Droplet generation and trapping for cell analytical two-phase microfluidic system

Multi-phase flows have numerous applications in the growing field of Lab-on-a-Chip (LOC) technology. In these multi-phase flow devices, monodisperse sheath emulsion helps to manipulate, focus and separate encapsulated chemical reagents or living cells. Therefore, cell-analytical and diagnostic procedures can be automatized on microscale, although the precise control of droplet parameters and movements are essential for their reliable application. Present work focuses on the design and characterisation of a two-phase microfluidic device with integrated electrode system (Fig. 2) for impedance analysis. The system is capable to create and manipulate droplets having pre-determined size aligned to the cell diameter of 4-20 µm.

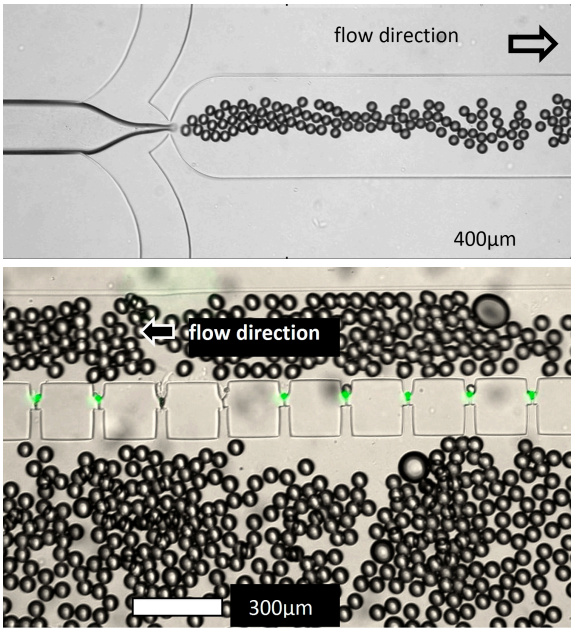

Figure 2 *Droplets generated in the two-phase microfluidic system (top), and encapsulated fluorescent beads trapped in the perforated cavities of the model microfluidic system (bottom).*

Present study analysed the influence of flow characteristics of special water-oil two-phase microfluidic systems on the droplet generation, cell encapsulation and trapping processes. Water droplets were dispersed in a continuous phase oil targeting precise size distribution to enable effective cell entrapment. The evolving droplet size and the number of encapsulated cells were examined considering the applied flow rate ratios of the two phases. Droplet size dependency on geometrical and flow parameters has

been investigated experimentally with special focus on the influence of flow rates and their ratios. Yeast cells were encapsulated in water droplets and distribution of their number in a single containment was also recorded. Direct dependency on the flow rate ratios with multiple maximum was observed versus the size distribution of the yeast cells.
Model was built in the simulation code COMSOL Multiphysics ©. The hydrodynamic environment of the trapping zone and droplet trajectories were calculated. The hydrodynamic behaviour of the microfluidic system was modeled by Finite Element Method (FEM) coupled with particle trajectory. Flow velocity field and decreasing flow rates in the perpendicular perforations demonstrate decreasing trapping efficiency of the cavities in the direction of the main flow. The suspected effect was verified by encapsulation and trapping fluorescent particles (Spherotech, 10 µm diameter): the trapping probability was experienced to be highest near the inlet of the trapping zone. The experimental results were compared to the simulation and the applicability of our droplet based cell microfluidic system was characterised.

Concentration gradient generation for cell population analysis

The chemical environment plays significant role in controlling biological, physiological processes in the living organism at molecular level. Accordingly, several biomedical researches aim to study the behaviour of cells in artificial chemical concentration distributions. Such as studying the mechanism of chemotherapy in cancer research can be highlighted. Due to the low sample volumes and accelerated reactions in microfluidic environment, this apparatus is highly suitable for advanced analysis of cell populations. These Lab-on-a-Chip (LoC) microfluidic systems are suitable for more realistic and accurate reproduction of extracellular microenvironment as well as for the manipulation and examination of cell populations with limited, but representative size. Flow-based concentration gradient generators (CGGs) are capable to maintain a stable spatial and temporal concentration distribution, which can be dynamically changed. Note, that due to the laminar flow conditions the molecular diffusion is limited, thereof special geometric design is needed to improve the performance of these microfluidic systems..

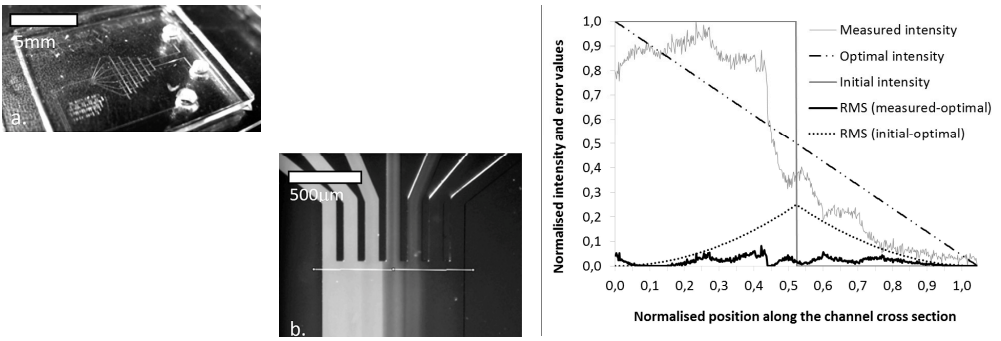

Figure 1 *Enhanced pyramid type CGG structure with Herringbone mixer (a), and the fluorescent intensity distribution (b, c) of the HSA concentration (at 0.1µL/s flow rate).*

Microfluidic chemical concentration gradient generators (CGGs) were designed with advanced geometric structures to establish a stable gradient along the gradient chamber at the output region. Basic structures were combined with secondary Herringbone mixers to improve the efficiency of distinct structures. The resulted concentration distributions were characterized for different flow rates and the performance of a given generator was defined as the root-mean-square of the difference between the measured and the ideal linear concentration values. The quality factors of the different structures were compared and the advantage of the integrated Herringbone mixer structures were proved.

SERS active periodic 3D structure for trapping and high sensitive molecular analysis of particles or cells

SERS (Surface Enhanced Raman Spectroscopy) evolves in close vicinity of metallic nanostructures where the interaction between the electromagnetic field of photons and the surface plasmons results in several orders of magnitude enhancement of the Raman signal. This effect extremely improves the sensitivity of Raman spectroscopy achieving the limit of molecule detection in attomolar (10^{-18} M) concentrations.
The highly sensitive molecule recognition performance of a specially designed surface SERS substrate was demonstrated. The general inverse pyramid structures were perforated as cavities in perforated membrane applicable for particle and cell filtering, sorting and trapping. In the voids of the gold covered substrate size compatible particles functionalised by different molecules were trapped, their SERS signal was detected and the different molecules were recognised (Fig.1).

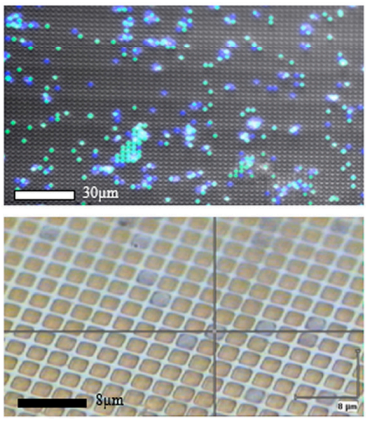

Figure 1 *Fluorescent beads with appropriate 2µm diameter (Sigma Aldrich - green and Spherotech - blue) entrapped in the periodic array of perforated pyramidal structures: multichannel fluorescent image (top) and upright optical micrograph (bottom).*

The fluorescent molecules were analysed by SERS taking advantage of the plasmonic enhancement by the structured surface of the traps. The definite and sensitive differentiation of the molecules immobilized on the polystyrene bead surfaces are presented in Fig. 2, where a huge increase in the Raman signal can be observed on the SERS surface.

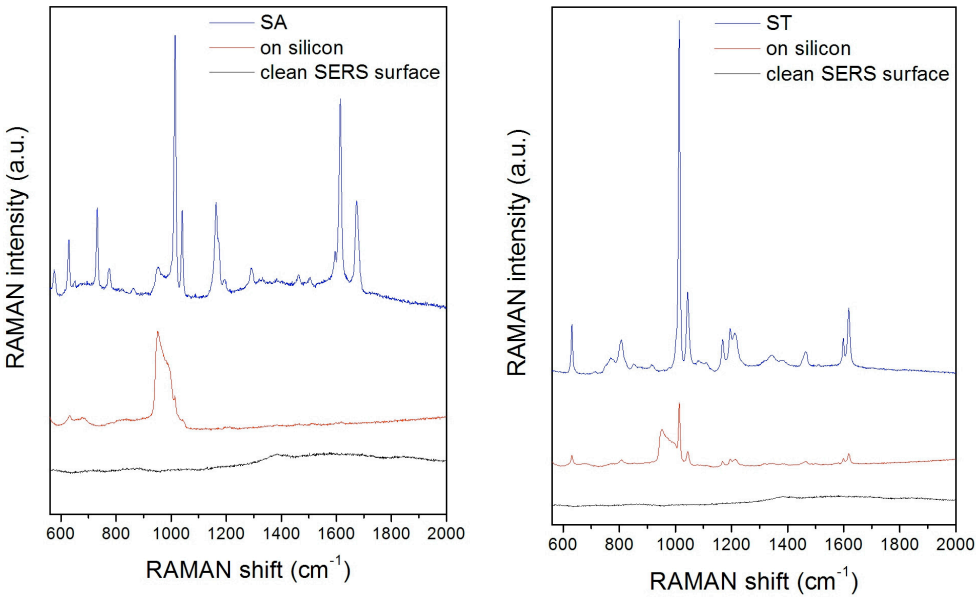

Figure 2 *Comparison of the SERS spectra recorded on the clean SERS substrate (black) and different fluorescent beads on silicon (red) and trapped in the periodic array (blue). SA – Sigma Aldrich and ST - Spherotech fluorescent beads, respectively.*

The advantage of the 3D structure was demonstrated for simultaneous particle (or cell) trapping and extremely sensitive SERS-based detection of molecules immobilized on the surfaces of the confined beads.

Intelligent wound patch for online monitoring wound healing processes – WoundER

In the clinical practice, the proper care of wounds is of primary importance in the case of accidents, postoperative and ulcerative ulcers. It is a basic expectation of the treating physician or nurse to provide continuous or regular information on the healing of the wound. In case of a home-based hospitalization, the control of wound is time consuming and difficult for the physician, but remote monitoring of the appropriate parameters can help in effective curing. The role of the intelligent bond is to facilitate the work of both the physician and the patient by monitoring the process of healing and, in the event of a problem, warns the user and the physician about the need for a check or a replacement.

In this work an intelligent tool was developed to provide continuous information about various parameters of the wound healing, such as temperature, humidity, and the tightness of the bandage. These are the major parameters determining the condition of the recovery of the injury. Aiming at the final wireless, point-of-care

application we focused on the minimisation of the energy consumption. Appropriate sensors were chosen and integrated into a flexible PCB. Low power consumption electronics solve the preliminary signal processing and communication tasks using Bluetooth protocol. Data processing and visualisation software was also developed (Fig.1). Functionality tests, calibrations and the influence on the patient behaviour are in progress.

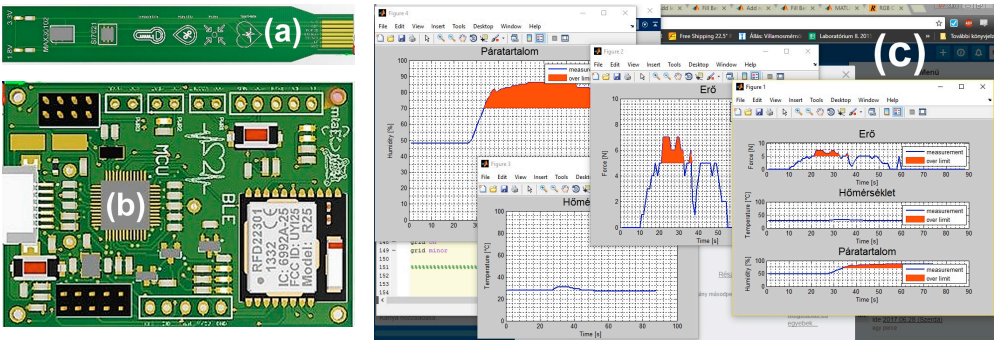

Figure 1 *Flexible PCB for sensors* ***(a)****, and signal processing electronics* ***(b)****, for wound healing monitoring system. The sensor data can be visualised in the application specific software* ***(c)*** *– WoundER / PC.*

Precisely controlled Focused Ion Beam milling of solid state nanopore array for molecule sensing

Nanoporous membranes are fundamental components of the transport modulation based label free electrochemical biosensors envisioned for high sensitive molecule detection. The sensitivity and the specificity of these sensors are significantly affected by the pore geometry what has to be fitted to the size and conformation of the target molecules. Precise tailoring of nanopore geometries and alignment to target molecule conformation and size improves the signal-to-noise level of the identification method - in our case the impedance spectroscopy. This pore geometry engineering is essential for reliable and reproducible manufacturing of solid state nanopore-arrays in integrated molecule diagnostic devices. Commercialization of the nanopore based biosensors or Lab-on-a-Chip devices seem to depend on the development of the high throughput nanofabrication techniques enabling reliable and reproducible shaping nanopore geometries in solid state membranes.

During this work, FIB milling process was exploited and the resulting time dependent nanopore geometries were characterized to achieve reliable and reproducible manufacturing nanoporous dielectric membranes. The time dependence of the evolving pore diameter in different layer structures was studied during ion beam milling. A pore diameter evolution rate parameter (γ) was defined, its continuous regression during the milling process verified and interpreted by the Gaussian profile of the spatial ion intensity distribution of the ion beam. Adequate milling parameters

(current, time) must be defined to achieve precise and predictable pore evolution in the applied membrane structure. The reproducibility of the FIB nanoprocessing was improved by neutralization (electrostatic grounding) of the sample surface. By this technique the distortion of the pore diameter could be reduced significantly, and the pore size variations reproducibly kept below 5 nm (Fig. 1).

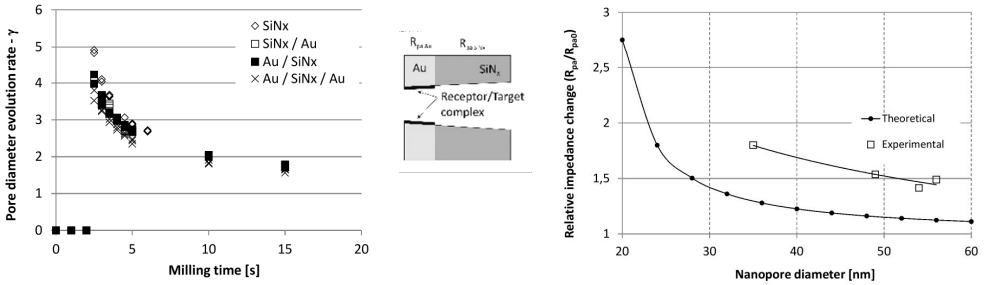

Figure 1 *Pore diameter evolution rate parameter (γ) as a function of the milling time (10 pA ion current and 30 keV ion energy) (left). Theoretical and measured relative impedance variation of the solid-state nanopore array as a function of the nanopore-diameter after avidin binding (right).*

The performance of membrane impedance analysis based molecule detection was studied by avidin-biotin binding in the nanopore array. The application of uniform pores is a major importance, since the sensor response depends on both the concentration of the target molecule and the pore size as well. Development of precise nanoprocessing techniques of predictable yield is therefore an elementary requirement for molecule sensing.

NEMS

Activity leader: J. Volk

Group members: Zs. Baji, A. Békési, G. Battistig, Cs. Dücső, P. Földesy, N. Q. Khánh, I. Lukács, Gy. Molnár, A. L. Tóth, Zs. Zolnai, Z. Szabó, and I. Bársony

Projects:

- OTKA K 109674 – Graphene based terahertz modulators (2013-2017)
- OTKA PD 116579 – Preparation of ZnO and Ga_2O_3 nanostructures by atomic layer deposition (2015-2018)
- OTKA K 112114 – Combined micro-nanotechnology supported by local probe analytical techniques: from pattern formation toward applications (2014-2017)
- EU FP7 ICT 611019 - High-resolution fingerprint sensing with vertical piezoelectric nanowire matrices (PiezoMAT) (2013-2016)
- NVKP_16-1-2016-0018 – Up-to-date functional materials for autonomous sensor nodes and sensor networks (KoFAH) (2016-2019)

Piezoelectric Nanowire Arrays for High Resolution Tactile Mapping

In 2017 our main contribution to the project was the completion of the fabrication process and the functional characterization of a high-resolution fingerprint sensor, where all the 250 nanowire (NW) pixels are contacted vertically (top-bottom contact). The base chips with Ga doped ZnO (GZO) seed layers and bottom contact were produced by project partner CEA-LETI. The subsequent fabrication steps, including the wet chemical NW growth, encapsulation, and top contact formation (Fig. 1) were optimized by the MFA team.

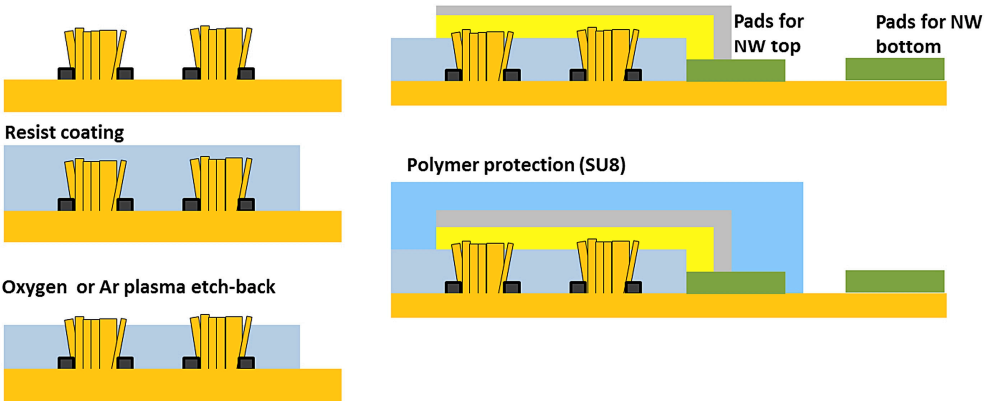

Figure 1 *Schematic representation of the process steps for top-bottom contacted NW: selective area wet chemical growth, polymer encapsulation, plasma etch-back, top contact deposition and patterning, deposition of a protective coating.*

The process started with the selective area wet chemical growth (SAWCG) of ZnO NWs where the nucleation windows were patterned by e-beam lithography. It resulted in an almost parasitic crystal free chip surface with bundles of vertically oriented NW in each matrix position (Fig. 2). The height of the NWs was approximately 3.5 µm.

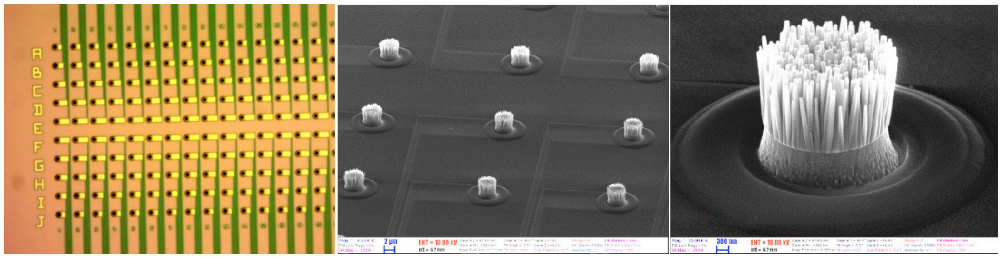

Figure 2 *Optical micrograph of the left half of the matrix* ***(a)****, and SEM images of ZnO nanowire pixels after wet chemical growth through e-beam lithography patterned nucleation windows* ***(b-c)****.*

SAWCG was followed by polymer spin-coating and hot plating, where three conventional polymer materials were tested: SU8 negative epoxy based photoresist, PMMA e-beam resist, and S1818 positive photoresist. The polymer matrix was etched in oxygen (or Ar) plasma until AFM observation confirmed that the tip of the NWs got released. An Au layer of 100-250 nm was then deposited onto the chip using e-beam evaporation method through a handmade stencil mask to obtain Schottky-type rectifying junction. Similar results were found for PMMA, however, SU-8 negative epoxy resist was found to leave an unwanted residue on the top of the NWs. Though it can be removed by physical dry etching using e.g. Ar plasma, due to the ion bombardment of ZnO top surface it results in an Ohmic contact with Au.
The photograph of chip in Fig. 3a shows the square shaped, reddish photoresist coating and the cross-shaped yellow top metal coating, which is connected to four metal pads through its arms. SEM observation of an FIB cut NW pixel confirmed the quality of the polymer encapsulation and direct contact between the top metal and ZnO NW (Fig. 3b). Before wire bonding of the chips randomly selected NW pixels were tested electrically. Most of the circuits demonstrated high quality Schottky type I-V characteristics with the expected polarity (Ohmic at the bottom and Schottky on the top). In case of the best chip the calculated ideality factor scattered in the 2.6 - 3.6 range which is rarely found in the literature for contacted NWs.

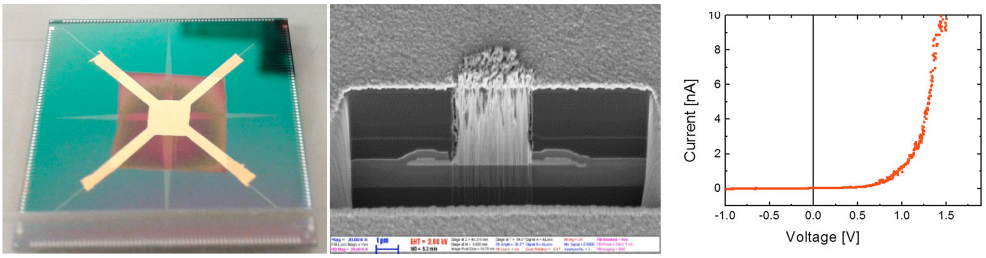

Figure 3 *Photo of the fabricated chip after top Au deposition* ***(a),*** *SEM image on the FIB cross section of a NW pixel* ***(b),*** *and a characteristic I-V curve showing Schottky type electrical junction* ***(c)****.*

In accordance with the original research plan most of the completed chips were sent to our consortium partners for automatic wire-bonding and for a subsequent direct piezoelectric test (zero-bias voltage type). However, a few were kept at MFA to carry out manual wedge bonding and an alternative, 'non-zero bias voltage' characterizations. These chips were wire bonded to a test printed circuit board with limited number of contact pads (128). Hence, roughly only every second pixel was connected among the available 250 matrix elements.
In Fig. 4, the macroscopic characterization setup purposely built for the alternative demonstration is shown. During the loading tests, simple stamps were pressed against active matrix of the chip (225 µm x 600 µm). The magnitude of the loading force was continuously monitored by a calibrated force gauge. The electrical signal of each wire bonded pixel was collected one-by-one through two ribbon cables by a high-density matrix switch which was connected to a source measure unit (National Instrument, PXI).

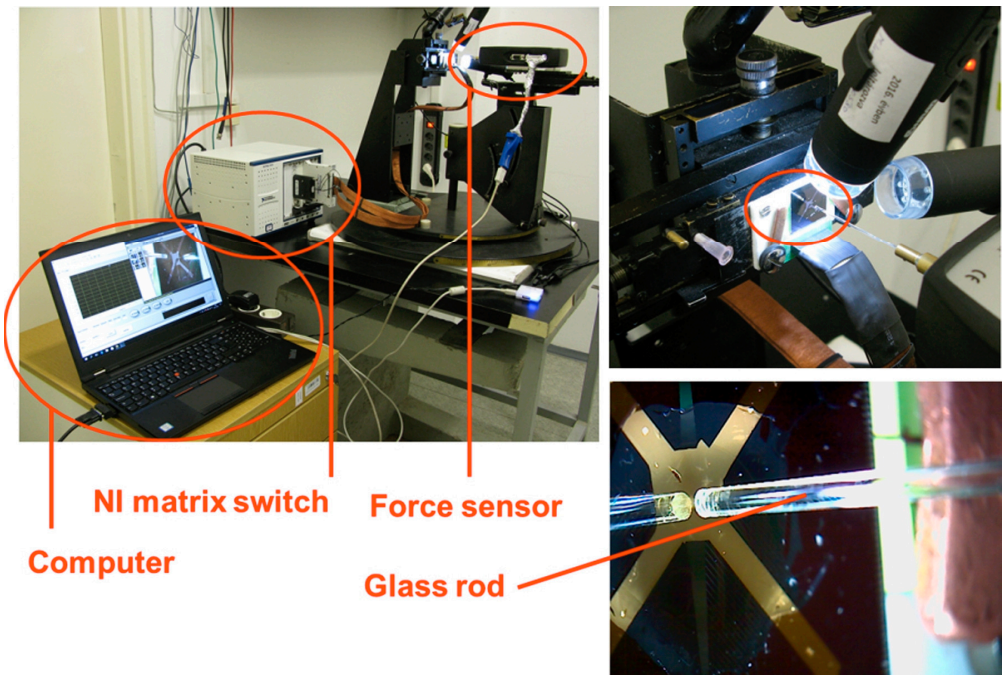

Figure 4 *Macroscopic setup for pressing tests using calibrated force sensor, source measure unit connected to a 128 channel high density matrix switch (NI PXI) and a controller computer with LabVIEW based data acquisition software.*

A LabVIEW based data acquisition and evaluation software was written to take I-V curves from each pixel, to monitoring time domain current/voltage signals, applying bias voltage, drawing response maps, and to monitor the signal of the force gauge. About 4.5 s is needed to collect current/voltage data for all the 128 channels at fix bias voltage/current and to refresh the chess pattern map.

At first I-V curves were collected from each pixel in relaxed state. It confirmed that most of the pixels, around 117 have Schottky type rectifying curves. By applying this current monitoring method on every channel we could monitor the whole matrix and may have a chance to recognize simple patterns. However, as we found, the measurement is less noisy in current generator mode, i.e. a constant current (e.g. 100 nA) was forced through each pixel and the generated voltage was monitored and visualized by the software. Prior to pressing, reference voltage (V_0) was taken from each pixel. Afterwards, only the absolute value of the relative change ($\Delta=|V_1-V_0|/V_0$) was shown by a color scaled matrix.

In order to demonstrate pattern recognition and position sensitivity a fine Al wire was pressed (Ø= 200 µm) against the NW matrix. The Al wire was looped around the apex of a Cu cone mounted on the horizontal force sensor. It was aligned such a way that the long axis of the Au wire was perpendicular to the long edge (600 µm) of the rectangular matrix. During the demonstration at first the wire was pressed near to the left edge of the matrix. The applied loading force was 500 mN. After releasing the

stamp it was moved manually towards the right side of the matrix along the x-axis using micro-meter positioner and pressed the matrix again. This sequence was repeated until reaching the right side of the matrix.

Fig. 5 shows the color maps taken at each loading event. Black pixels in a chess pattern indicate the un-bonded inactive elements. Deep blue color corresponds to the unchanged voltage signal (Δ =0), while red is set to show a relative change of 7% (Δ =0.07) in this particular experiment. On the right side of Fig. 5 snapshots were taken by a USB camera to show the position of the pressing stamp relative to the chip. For clarity, two dotted red lines indicate the initial and final position of the Au wire. The recorded maps on the left side clearly show the perpendicularly elongated shape of the Au wire and its position. Even though some of the unloaded pixels are also red due to the voltage drift, the pattern recognition concept, at sufficiently high loading force, seems to be feasible.

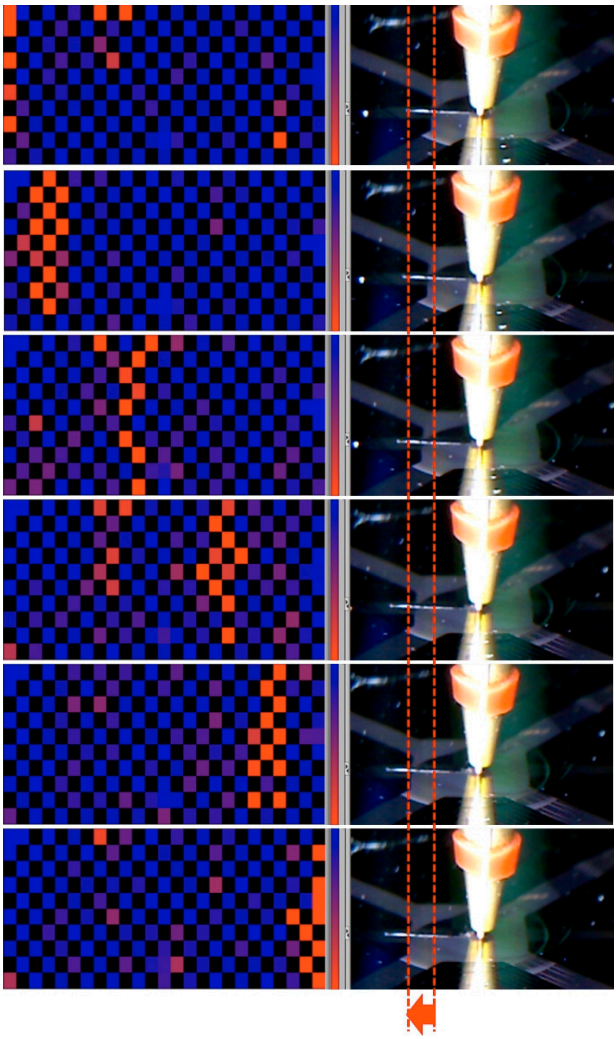

Figure 5 *Relative voltage change maps at a bias current of 100 nA at different positions of the perpendicularly aligned AI wire type stamp. Position of the stamp was changed from left to right of the matrix with incremental steps of approximately 100 µm.*

Spiral-Shaped Piezoelectric MEMS Cantilever Array for Fully Implantable Hearing Systems

Fully implantable, self-powered hearing aids having no external unit could significantly increase the life quality of the patients suffering from severe hearing loss. This highly demanding concept, however, requires a strongly miniaturized device which is fully implantable in the middle/inner ear and includes the following components: frequency selective microphone or accelerometer, energy harvesting device, speech processor, and cochlear multielectrode.

In this work we demonstrated a low volume, piezoelectric MEMS cantilever array which is sensitive even in the lower part of the voice frequency range (300-700 Hz). The test array consisting of 16 cantilevers (Fig. 1b) has been designed using Comsol Multiphysics © simulations and fabricated by standard bulk micromachining on a Si-on-Insulator (SOI) wafer with AlN as a CMOS and biocompatible piezoelectric material. The low frequency and low device footprint (2×2 mm^2) were achieved by Archimedean spiral geometry and Si seismic mass (Fig. 1a).

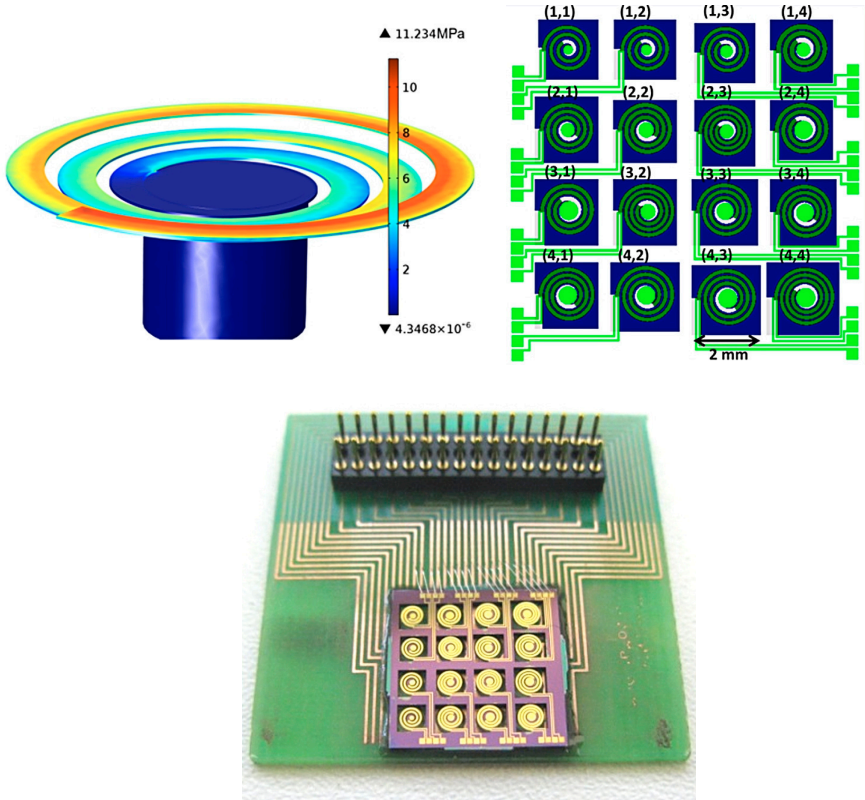

Figure 1 *Tensile stress distribution along the beam, calculated by finite element method* ***(a)****, layout of the selected 4x4 spirals* ***(b)****, and the wire bonded chip ready for shaking tests* ***(c)****.*

On the 4” wafer most of the chips with the sensitive spirals survived the fabrication process of over 30-steps; an example is shown in Fig. 1c. Scanning electron micrograph of two typical spiral cantilevers situated in the (1,3) and (3,4) array positions are shown in Fig. 2a and b, respectively. The darker region on the cantilever beam corresponds to the metal-piezo-metal stack covered region. A reflecting Au disk in the center was designed for additional laser beam deflection tests. As shown in both SEM images the diameter of the seismic mass is decreasing from the back side towards the membrane, i.e. the sidewall of the DRIE etching was not perpendicular.

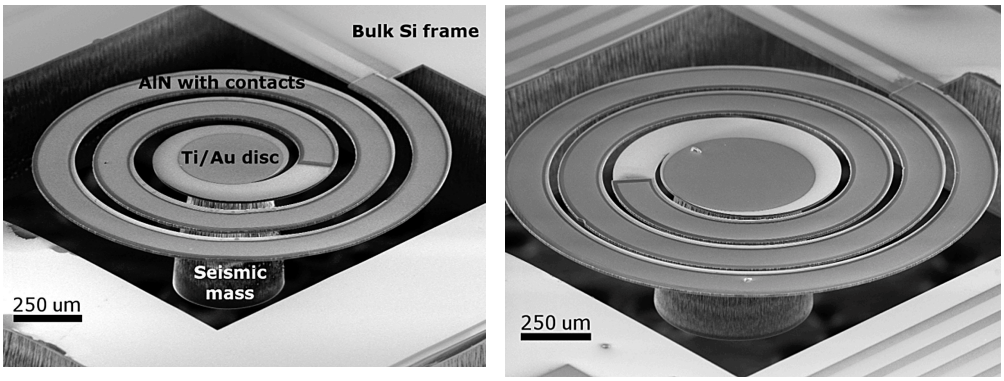

Figure 2 *Tilt-view SEM images of two typical suspended spiral-shaped cantilevers (1,3) (a) and (3,4) (b) with contacted AlN layer (darker region) on their top surfaces and a wafer thick 3D-micromachined Si seismic mass beneath.*

Vibration tests, performed at a fix acceleration of 1g (9.81 m/s^2) using a PID controlled mini-shaker confirmed the frequency selectivity of the cantilever array (Fig. 3). Most of the spirals (12 out 16) showed sharp resonance peaks scattering in the range of 281-672 Hz. For clarity, the spectra were ordered according to their resonance frequency from low to the high (Channel 1-12). The calculated Q-factors ($f_0/\Delta f_{\sqrt{2}}$) in air vary in the range of 117-254.

As shown in the inset image of Fig. 3 the recorded time-dependent open circuit signal is purely sinusoidal without any vertical offset which indicates stress-free cantilevers. The inactivity of the remaining 4 devices can be attributed to the low electrical resistance of the metal/AlN/metal stacks. That may be the result of random defects in the AlN layer. The generated open circuit voltages fell in the range of 3.0-9.6 mV.

The frequency selectivity demonstrated in the lower half of the voice frequency range and the relatively high Q-factor measured in air are promising for next generation fully implanted cochlear implants (FICI). Moreover, due to the low volume and weight several cantilevers (>12) could be placed inside the human middle ear. Nevertheless, there are still several challenges to be solved: the generated voltage and especially the power are too low for the direct excitement of the hearing nerves, the piezo-cantilevers have not been tested at low accelerations (<1 mg), and overtones may generate unwanted signals.

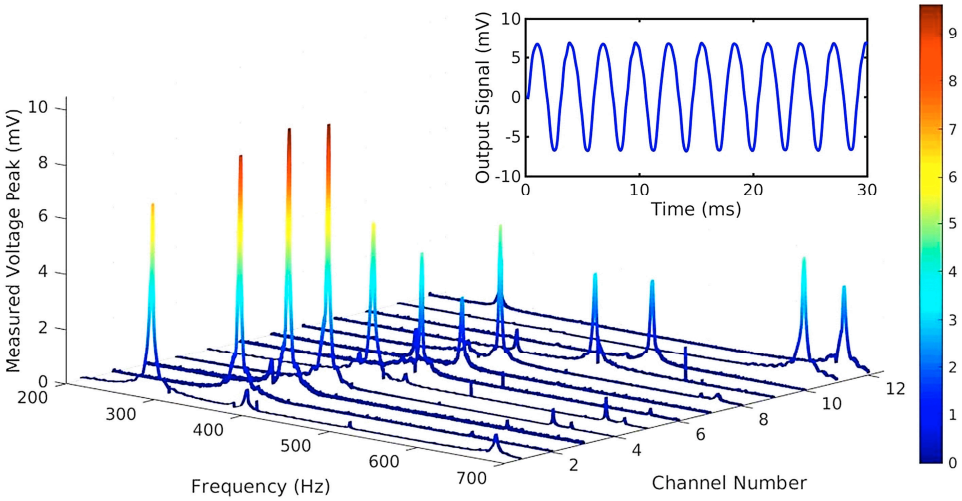

Figure 3 *Piezoelectric output voltage during continuous sinusoidal excitation at a feedback controlled acceleration of 1g. Depending on the geometry the base frequency of the cantilevers falls in the range of 281-673 Hz. Inset shows the sinusoidal output waveform of channel 1 at resonance.*

Vibrational energy harvester powered sensor node

The aim of this work is to demonstrate a wireless accelerometer sensor node which can operate autonomously even in dark and hardly accessible places in a continuously vibrating ambient such as industrial machine, vehicle, heavy traffic road, bridge, railway etc. In such environments vibrational energy harvesting (VEH) seems to be a reasonable choice to power 'place and forget' type systems.

In this bread-board demo set-up a commercially available piezoelectric energy harvester was applied to investigate limits and challenges for microscopic piezo-MEMS based energy harvesting. The development of the latter one is currently in progress in the KoFAH project.

The developed sensor node (Fig. 1a) consists of a purpose designed electronics and a tunable VEH holder. The former one was optimized for low power consumption and continuously varying charging voltage level. The PCB, shown in Fig. 1b, includes a microcontroller, an RF module for short-range wireless communication, an energy management unit, two supercapacitors, and an accelerometer. During operation it is powered by the piezo VEH (Midé) whose resonance frequency can be adjusted to the characteristic resonance peak of the ambient by changing the clamping position, i.e. the free length of the vibrating cantilever beam.

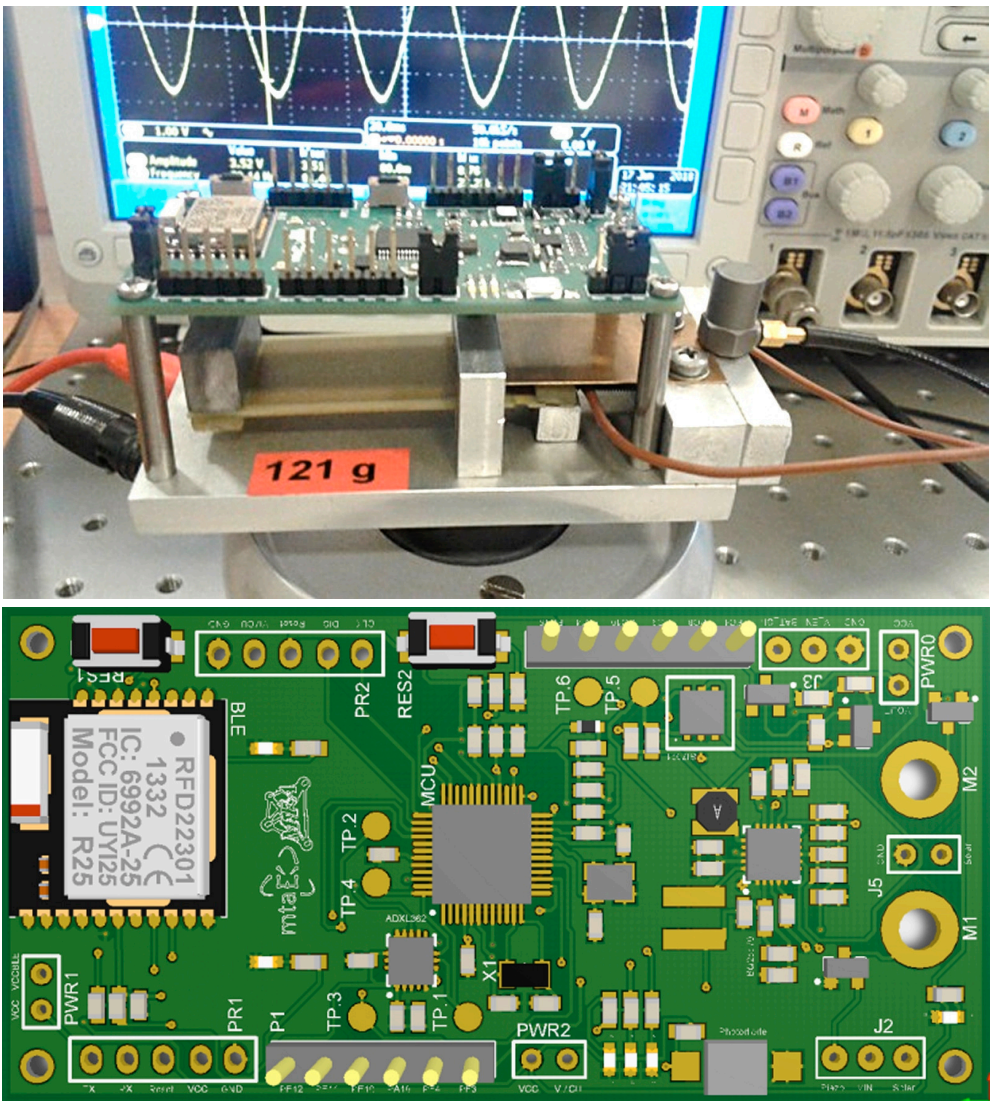

Figure 1 *Vibrational energy harvester powered wireless sensor system (top) and the electronics of the purposed designed electronics (bottom).*

Thin Film Physics Department

Head: Dr. Katalin BALÁZSI, Ph.D., senior research fellow

Research Staff

- Ildikó CORA, Ph.D.
- Zsolt CZIGÁNY, D.Sc.
- Zsolt FOGARASSY, Ph.D.
- Viktória KOVÁCSNÉ-KIS, Ph.D.
- János LÁBÁR, D.Sc,
- Riku LOVICS, Ph.D.
- Fanni MISJÁK, Ph.D. (on leave, Univ. Ulm from October)
- Béla PÉCZ, D.Sc., deputy general director of Centre for Energy Res., MFA director
- György Zoltán RADNÓCZI, Ph.D.
- György SÁFRÁN, C.Sc.
- Attila SULYOK, Ph.D.
- Orsolya TAPASZTÓ, Ph.D.
- Lajos TÓTH, C.Sc.

- Árpád BARNA, D.Sc., Prof. emeritus
- Péter B. BARNA, D.Sc., Prof. emeritus
- György GERGELY, D.Sc., Prof. emeritus.
- Miklós MENYHÁRD, D.Sc., Prof. emeritus
- György RADNÓCZI, D.Sc., Prof. emeritus

Ph.D. students

- Erzsébet DÓDONY (from September)
- Mónika FURKÓ
- Klára HAJAGOS-NAGY
- Tamás KOLONITS
- Nikolett OLÁH (maternity leave from August)
- Adél RÁCZ
- János SZÍVÓS
- Márton SZENDRŐ
- Zsolt DALLOS (from August)
- Haroune Rashid BEN ZINE ("Hungaricum stipendium")
- Awais QUADIR ("Hungaricum stipendium")
- Soukaina LAMNINI ("Hungaricum stipendium" from February)
- Mohamed ARFOIU ("Hungaricum stipendium" from September)

Technical Staff

- Noémi SZÁSZ
- Sándor GURBÁN
- Andor KOVÁCS
- Viktor VARGA
- Andrea FENYVESINÉ JAKAB
- Valéria OSVÁTH
- Tamás ZAGYVA
- Bence GELLAI
- Zsolt DALLOS (50%)

In 2017 the Department continued its long-time research in the following main topics: preparation, structure and physical properties of 1) semiconductor layers, 2) protective coatings, 3) high-entropy alloys, 4) ceramic composites, and 5) bioceramics.

More in details, studied were structure and growth evolution in semiconductor GaN based layers, of TiC/a:C thin hard coatings, nanopatterning of CoPt magnetic layers, and a new type of functional high-entropy alloy.
Development of hydroxyapatite bioceramic coatings on surgical implants was still an important research subject. As new topic, development of highly wear resistant and low friction ceramic/graphene nanocomposites prepared by powder technology was introduced.
Furthermore, studies of ceramic dispersed austenitic 316L steel composites for high temperature and nuclear applications represented a new direction. In all cases, long experience of the department in transmission electron microscopy (TEM) and in methodology of electron diffraction was thoroughly used. Our "one-sample combinatorial method" for high-throughput TEM and for other analytical studies on thin binary layers was also applied where proper.
In 2017, 39 papers appeared in refereed journals with a cumulative impact factor of 121. In addition, 12 papers in conference proceedings were published with no impact factor. Members of the group presented 7 invited lectures, 22 oral talks and 29 posters at international conferences. The group received 1590 independent citations in the examined interval of the last two years. The 15th Conference and Exhibition of the European Ceramic Society was organized in Budapest between July 9 and 13 by members of Thin Film Physics Department.
Summarizing also other activities, members of the group lectured three courses at universities and four members held laboratory practices. All courses were for full semester (Roland Eötvös University, Budapest - ELTE, and Budapest University of Technology and Economics - BME, and Óbuda University - OE). In addition, 12 Ph.D. students were supervised.
Social activity of the group is landmarked by 15 memberships in different committees of the Hungarian Academy of Sciences and in boards of societies, giving one elected representative to the General Assembly of the Hungarian Academy of Sciences.

TEM study of the as-deposited and annealed Ga_2O_3 films grown by vapor phase epitaxy

(MTA Postdoctoral Fellowship and bilateral scientific agreement between CNR and MTA)

I. Cora[a], B. Pécz[a], M. Bosi[b], F. Mezzadri[b], F. Boschi[b], G. Calestani[b], R. Fornari[b], M. Čaplovičová[c], and A. Rečnik[d]

[a]MTA EK MFA Thin Film Physics Department, Budapest, Hungary, [b]IMEM-CNR, Parma, Italy, [c]Slovak University of Technology, Bratislava, Slovak Republic, [d]Jožef Stefan Institute, Ljubljana, Slovenia

Ga_2O_3 is a wide bandgap semiconducting oxide (~4.7 eV), promising for UV optoelectronics and power electronics. Ga_2O_3 layers were grown onto (001) surface of α-Al_2O_3 by vapor phase epitaxy and were annealed at 1000 °C for 2 and 6 hours. The as-deposited layers and the two annealed samples were studied by high-resolution transmission electron microscopy (HRTEM), X-ray diffraction (XRD) and Differential Scanning Calorimetry (DSC*). In situ* heating was also performed in TEM in order to follow the κ→β structural transformation. A previous XRD study [F. Mezzadri et.al. Inorg. Chem. 55, 12079. (2016)] on *as-deposited films* showed that these films are single crystalline epitaxial layers and exhibit hexagonal *P6₃mc* space group symmetry, characterized by partial occupation of the Ga sites, which corresponds to the ε phase, with disordered Ga atoms in the structure. The studies coupled with simulations by JEMS allowed us to investigate the real structure of this phase on the nanoscale [19] The structure is ordered in 5-10 nm large (110)-twinned domains, and each domain has an orthorhombic structure with $Pna2_1$ space group symmetry, called κ-Ga_2O_3. This phase is a new polymorph among the Ga-oxides. Parallel XRD analysis carried out on thicker samples (9-10 μm layer thickness) confirmed the same results, and refined structural parameters were provided.

Crystalline structure of these Ga_2O_3 layers consists of an ABAC oxygen close-packed stacking, where Ga atoms in between occupy octahedral and tetrahedral sites forming two types of polyhedral layers parallel to (001) (Fig. 1). The edge-sharing octahedrons and the corner-sharing tetrahedrons form zig-zag ribbons along the [100] direction. Anti-phase boundaries are common inside the domains. Polar character of the structure was confirmed, in agreement with the characteristics of the $Pna2_1$ space group and explaining the ferroelectric nature. Differential Scanning Calorimetry (DSC) up to 1100 °C was carried out on fragments of pure κ-Ga_2O_3 taken from a very thick layer [34]. This polymorph can tolerate long-lasting thermal treatments up to 700 °C, although some weak traces of lattice modifications were detected by DSC (endothermic bent) starting from about 650 °C. A complete transition to β-phase is observed for annealing temperatures ≥900 °C while at intermediate temperatures of 800 °C the films showed very disordered noisy diffraction spectra, with no evident diffraction peaks of either κ or β types. The detailed structural transformation was studied by TEM during *in situ* heating (results are under publication).

The duration of *ex situ* thermal treatment at 1000 °C strongly influenced the crystallinity of the samples: while for a 2 hours annealing, the sample remained polycrystalline and strongly textured, samples annealed for 10 hours were found almost single crystalline [34]. In more detail, the sample that was *annealed ex situ for 2 hours*, consists of pure β-Ga_2O_3. The layer is polycrystalline and strongly textured: [-201] direction of each β-Ga_2O_3 crystal is perpendicular to the (001) of the α-Al_2O_3. The *10 hours-long, ex situ annealed sample* is pure β-Ga_2O_3 and almost single crystalline: β-Ga_2O_3 grow onto the α-Al_2O_3 with epitaxy: (310)/[-13-1] β-Ga_2O_3 ‖ (001)/[1-10] α-Al_2O_3 [34]. The upper part of the layer grows with epitaxy but with a different orientation: (310)/[-130] β-Ga_2O_3 ‖ (001)/[1-10] α-Al_2O_3.

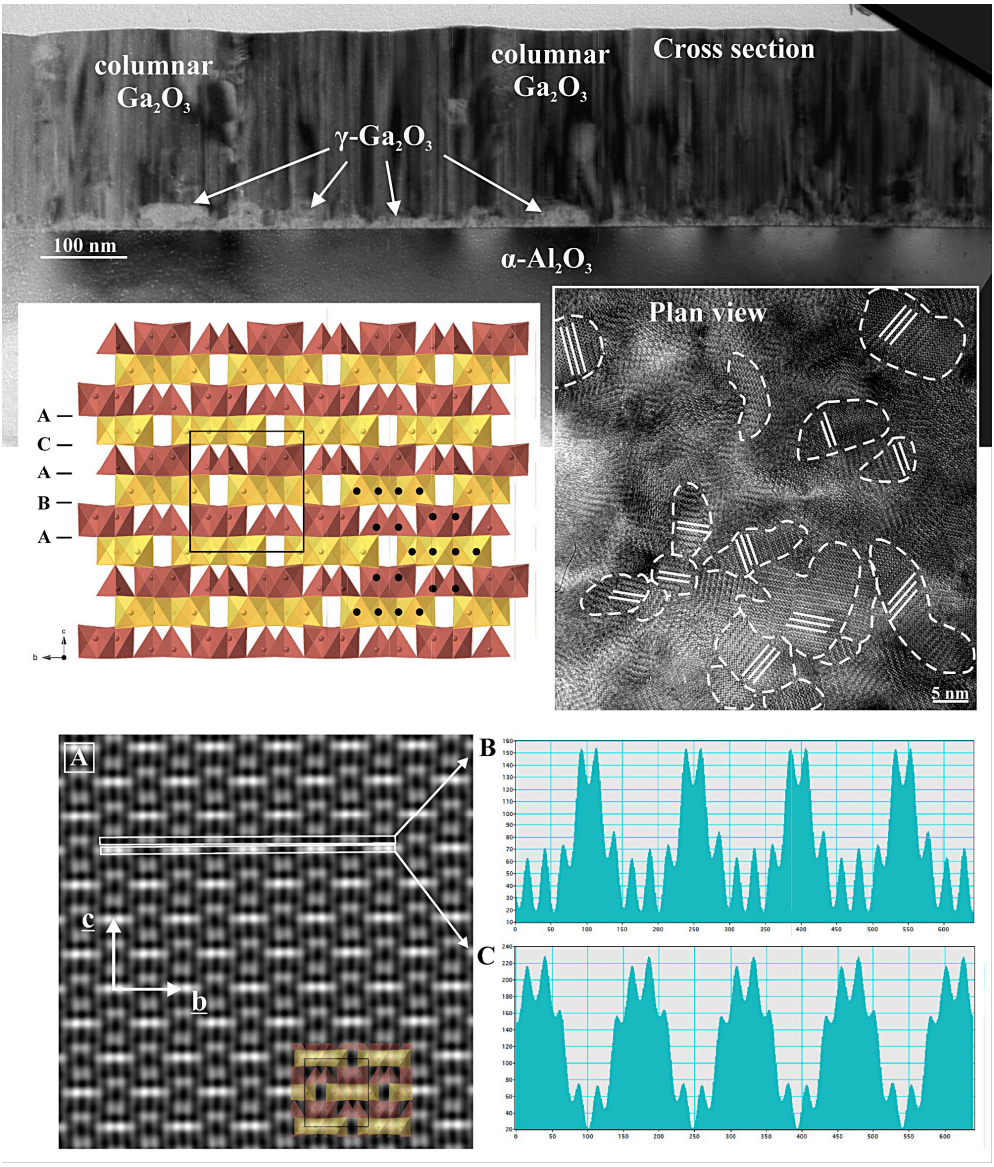

Figure 1 *TEM images of the cross-section and the plane view TEM specimens of the as-deposited layers with the corresponding crystal structure of κ-Ga_2O_3. The structure is textured consisting of 5-10 nm large (110)-twinned orthorhombic domains. STEM image (at the bottom) with the corresponding line scans shows the Ga atoms in [100] projections. Spurious peaks are due to overlapping of the twin domains.*

Phase formation sequence in the Ti/InP system during thin film solid-state reactions

J. L. Lábár, M. Menyhárd, E. Ghegin[1,2,3], Ph. Rodriguez[2], S. Favier[1,2], I. Sagnes[4], and F. Nemouchi[2]

[1]STMicroelectronics; [2]Univ. Grenoble Alpes; [3]CNRS-C2N; [4]Centre de Nanosciences et de Nanotechnologies

Continuous demand for increasing data rates necessitates switching to optical devices and interconnections. Due to the indirect bandgap of Si, the III-V semiconductor compounds are considered and introduced as candidates in optical applications. Integration of these devices in the Si CMOS technology (called "Si Photonics") requires a change of material of electrical contacts, as those traditionally contain Au or Pt (elements which are not even allowed to enter into Si cleanrooms, thus are excluded from the integration procedure). Ohmic contacts with low specific contact resistivity are needed. The main process flow consists of a surface preparation (wet and/or plasma treatments), one or several metal layer depositions and a heat treatment. These processes aim to control formation of intermetallic compound(s), thereby modifying the contact resistivity.

In this paper, the phase formation sequence of various observed phases obtained on the Ti (20 nm and 50 nm)/InP systems under rapid thermal processes (RTP) was investigated to identify mechanisms responsible for their formation. Sample preparation consisted of wet etching for 30 s in dilute HCl:H_2O (1:2) solution followed by a direct Ar^+ plasma etching (RF) prior to the metal deposition process. The 20 and 50 nm-thick titanium films were deposited by physical vapor deposition (magnetron sputtering in DC mode) at 100°C and capped by 7 nm thick TiN protecting films deposited at the same temperature.

Investigations on this system highlight the initiation of a reaction between the Ti and the InP substrate during deposition process performed at 100°C. Simultaneous formation of two binary phases, namely, Ti_2In_5 and TiP is detected by XRD and confirmed by electron diffraction (SAED) in the TEM (Fig. 1). TEM image corresponding to a sample subjected to Ar pre-clean, features important roughness with a discontinuous TiN film, which morphology is determined by individual TiN grains. An amorphous layer of about 10 nm is also identified. Because of the important roughness, the corresponding Auger electron spectroscopy (AES) depth profile (Fig. 2) is highly smeared and the signals emanating from the InP, the amorphous layer, and the TiN top layer are not clearly distinct. Nonetheless, a compositional gradient can be observed in the profile. It, therefore, appears that this kind of plasma leads to a phosphorus depletion of the InP surface consistently with what was previously reported in the literature [E. Ghegin et.al., Microelectron. Eng. 156, 86 (2016).]. Formation of the Ti_2In_5 and TiP phases is attributed to the compositional gradient induced in the InP by the wet surface preparation and enhanced by the subsequent in situ Ar^+ pre-clean. Once formed, the TiP layer acts as a diffusion barrier inhibiting further reaction up to 450°C in spite of the presence of

an important Ti reservoir (Fig. 3). Consequently, the layer system is stable up to 450°C. At higher temperature, however, i.e., from 550°C, a reaction is enabled either by the enhancement of the species diffusing through the TiP layer or by its agglomeration. This reaction gives rise to the total consumption of the Ti_2In_5 and Ti while the TiP and In phases are promoted. For more details, see [40].

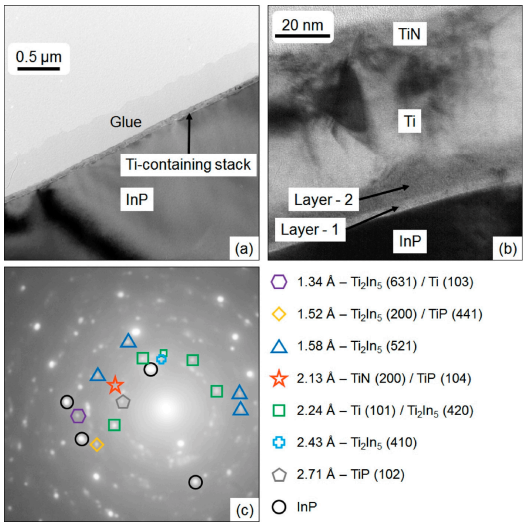

Figure 1 *Bright field TEM cross section of (a) the TiN (7 nm)/Ti (20 nm)/InP as deposited sample in low magnification, (b) the TiN (7 nm)/Ti (50 nm)/InP as deposited sample in high magnification and (c) the corresponding SAED pattern highlighting the presence of four different layers in the system.*

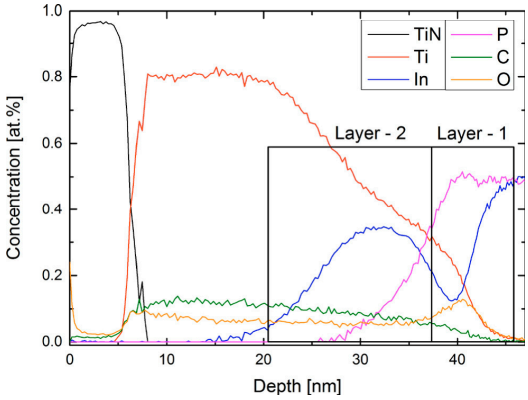

Figure 2 *AES depth profile corresponding to the as deposited TiN (7 nm)/Ti (20 nm)/InP system.*

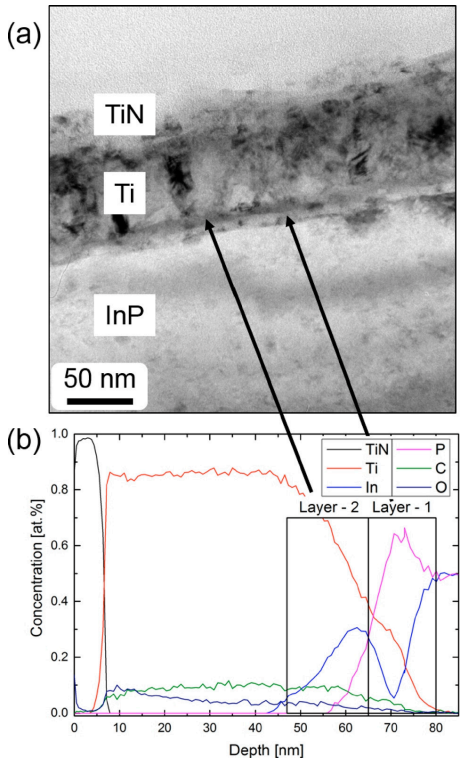

Figure 3 *above (a) TEM cross section of the TiN (7 nm)/Ti (50 nm)/InP system annealed at 450°C and (b) corresponding AES depth profile.*

Effect of deposition parameters on cubic TiC and hexagonal Ti formation in TiC/a:C thin films

Z. Fogarassy, N. Oláh, I. Cora, Z. E. Horváth, T. Csanádi (IMR SAS), A. Sulyok, and K. Balázsi

Formation of TiC and Ti phases and their influence on their mechanical properties were studied. Thin layers were deposited by DC magnetron sputtering at room temperature in ultrahigh vacuum from two targets (Ti and C).

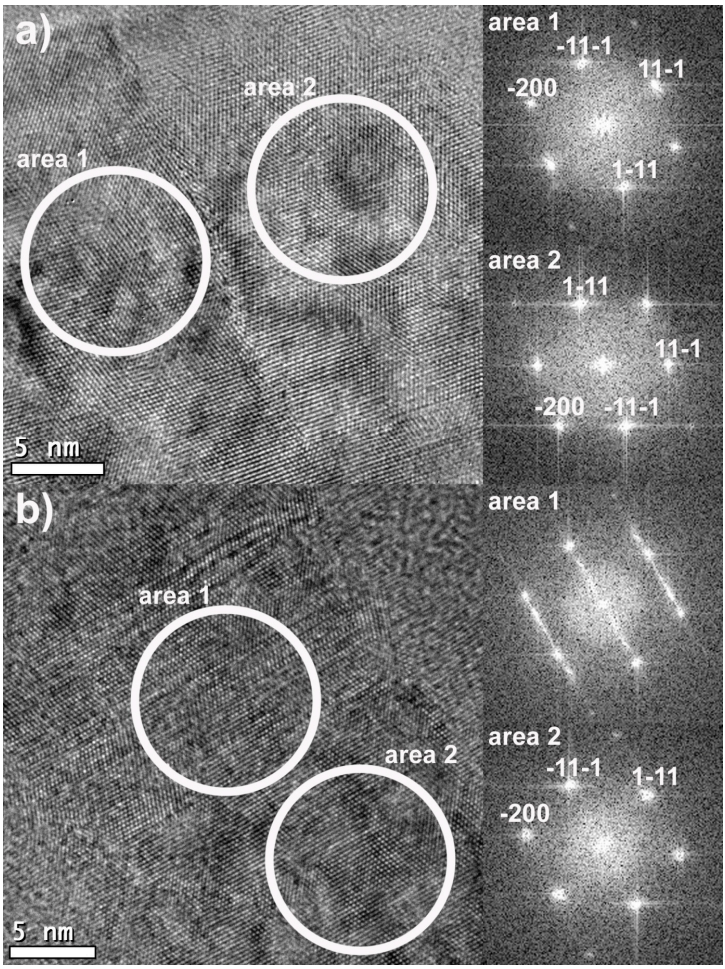

Figure 1 *HRTEM images of the TiC layer with 86 at % Ti content. In the* ***a)*** *HRTEM image of an incoherent twin boundary and the FFTs from twin boundary two side. In the* ***b)*** *HRTEM image, stacking faults in the c-TiC are forming h-Ti structure, as seen on its associated FFTs (in one FFT area are from twin boundaries, in the other FFT area twin boundaries are not present).*

Thin films with columnar structure containing Ti between 58 at.% and 95 at.% were obtained in dependence of the sputtering power of the carbon (C) and titanium (Ti) target. Previous studies by us covered mechanical and structural properties of the a-C/TiC and TiC films with Ti content from 0 to 58 at.% [N. Oláh et.al., Surface and Coatings Technology, vol. 302, (2016), pp.410-419.]. Cubic TiC phase (c-TiC) was formed in films with Ti content from 58 to 86 at.%. Formation of hexagonal Ti (h-Ti) occurred first from 86 at.% of Ti content and was observed for all films with Ti content between 86 and 95 at%. The c-TiC disappears at 90 at. % and higher Ti content, where only h-Ti crystallizes. Both the h-Ti structure and the c-TiC structure can be formed in the layer with 86 at.% titanium content. The HRTEM investigation shows that dominantly c-TiC structures are formed in the film. However, c-TiC grains contain several stacking faults. There are some areas where after a single stacking fault the orientation of the grain changes in one part of the grain (Fig. 1a right). In such areas where the two grains with different orientations meet, they form (112) type incoherent twin boundary perpendicular to the surface of the substrate (Fig. 1). In certain areas the density of stacking faults increases and locally the crystal structure of c-TiC can pass through h-Ti structure. The TEM and the XRD studies confirmed the dominance of c-TiC (111) texture with increasing Ti content.
The hardness of thin films agrees with structural observations. The highest hardness value (~26 GPa) showed the c-TiC thin film with 67 at.% Ti content. A hardness of ~25GPa was measured in films with 58 to 70 at.% Ti content. The nanohardness showed decreasing character with increasing Ti content over 70 at.%. The lowest values of nanohardness (~10 GPa) was observed for thin films with only h-Ti phase.
The present phases will have a large influence on mechanical properties: the films with pure cubic TiC phase exhibited two times higher hardness than films with the softer hexagonal Ti phase. It was proven, that the lowest hardness value of around 10 GPa in films with 90-95 at.% Ti is still 2-4 times higher than the hardness of various Ti alloys like the TiAl6V4 alloy that is often used as implant material.

Structure and mechanical properties of hard yet fracture resistant W-B-C coatings with varying W and C content

Zs. Czigány, M. Alishahi (Brno) , S. Mirzaei (Brno), P. Soucek (Brno),
L. Zábransky (Brno), V. Buršíková (Brno), M. Stupavská (Brno), V. Peřina (Řež),
P. Vašina (Brno), and K. Balázsi

Sputter deposited WBC films were investigated in cooperation with Department of Physical Electronics of Masaryk University, Brno, Czech Republic (Brno) and Nuclear Physics Institute of Academy of Sciences of the Czech Republic, Řež (Řež). Preparation of coatings simultaneously exhibiting high hardness and enhanced fracture toughness is currently a hot topic, as nowadays used ceramic based protective coatings show difficulties to cope with increased demands due to their inherent brittleness. Materials exhibiting such seemingly contradictory combination of

mechanical properties - high hardness and moderate ductility - was already realized in Mo2BC and recently predicted by ab initio calculations in crystalline X_2BC system (X = Ti, V, Zr, Nb, Mo, Hf, Ta, W). The WBC films were deposited by RF magnetron sputtering of W, C and B4C targets in Ar at 500°C. The coatings were systematically synthesized to contain a constant amount of boron. The effect of C/W ratio on the bonding structure, microstructure, hardness, stiffness, scratch behaviour and fracture toughness of the coatings was studied. The films with C/W ratio of 0.11 and 0.78 have amorphous structure, however, the films also exhibit a certain short range ordering that is manifested in irregular curved lattice fringes with short extension in HR images. The films with C/W ratio of 0.48 and 0.61 contain crystalline clusters inside the near-amorphous matrix (Fig. 1). These clusters of 1-2 nm size with lattice fringe contrast are clearly visible in the HRTEM images. In the diffraction patterns sharper textured segments at 2.41 are observable within the inner diffuse ring. The textured segments indicate lattice planes parallel with the substrate surface. Therefore, coatings with the C/W ratio the furthest from W2BC stoichiometric composition were near amorphous with no obvious crystallites, coatings closer to the W_2BC stoichiometry were nanocomposites with small grains embedded in an amorphous matrix. A gradual roughening of the microstructure from dense close packed to a porous columnar structure was observed with increasing of the C/W ratio and was attributed to a decrease of the energy flux and momentum transfer to the growing coating during the deposition with the increasing C/W ratio. All of the presented coatings classified as hard coatings with hardness > 20 GPa (Fig. 2). The level of crystallinity played no crucial role in determining the hardness of the coating, while the effect of the coating structure was clear – the densest coating with the highest relative amount of W-B bonds exhibited the highest hardness of ~ 29 GPa. The presented coatings furthermore exhibited high adhesion to industrially important substrates as well as scratch and crack resistance unmatchable by current top-of-the-shelf industrial protective coatings of comparable hardness. Therefore, W-B-C coatings might pave the way to the next generation of coatings for tool protection.

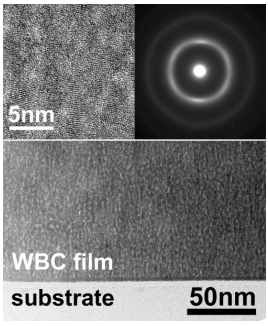

Figure 1 *Cross-sectional TEM image of WBC film with C/W=0.61. Porous column walls are visible. Nanocrystallites are observed by HRTEM and SAED pattern (insets).*

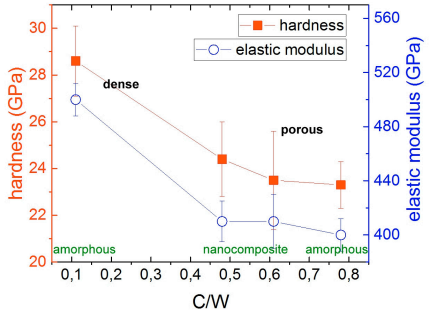

Figure 2 *Hardness and elastic modulus of WBC films with different C/W ratio. The mechanical properties show correlation with the density of the microstructure rather than with the degree of the crystallinity of the films.*

Dot patterning of CoPt films by RF plasma etching for high capacity magnetic media (Ph.D. work)

J. Szívós, G. Sáfrán, Sz. Pothorszky, J. Soltys,
M. Serényi, H. An, Tenghua Gao, A. Deák, and J. Shi

In a Ph.D. work new, cheap and green solution for the nanopatterning of FePt and CoPt films was searched for to implement Bit Patterned Magnetic Media (BPM) as a potential candidate to increase bit density in present-day hard disk drives. As for template Langmuir-Blodgett (LB) films of silica nanospheres self-organized in hexagonal structure were applied. In 2015, excimer laser pulses were used for surface modification through the template [J. Szívós et.al., Vacuum 109, 200 (2014)]. In 2016, RF plasma-etching was introduced that removes the layer only at the uncovered areas, and separated islands are formed behind the silica nanospheres. The technique was demonstrated through nanopatterning metallic, semiconductor and insulator films and the influence of plasma parameters was revealed on the depth, morphology and resolution.

RF plasma etching technique was applied in 2017 for dot-patterning CoPt magnetic layers prepared in cooperation with the Tokyo Institute of Technology. We obtained hexagonally distributed individual magnetic domains of sizes below 100 nm. TEM (Fig. 8), VSM (Fig. 9) and MFM studies revealed that our films exhibit the hard magnetic L10 (fct) CoPt phase in separated and magnetically decoupled, islands. Such nanopatterned layers are candidates for dot patterned magnetic media [G. Sáfrán, Applied Surface Science 435 (2018) 31–38].

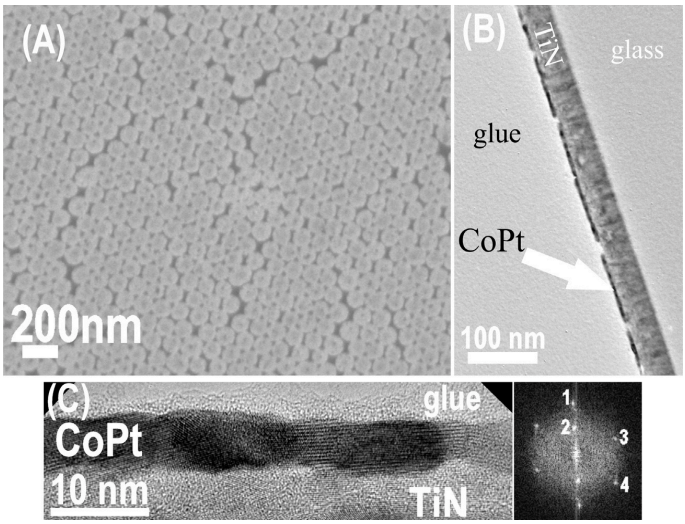

Figure 1 ***(a)*** *SEM and* ***(b)*** *XTEM of dot-patterned L10 (fct) CoPt film.* ***(c)*** *HRXTEM image and its Fast Fourier Transform. Marked reflections: 1 – fct CoPt(002); 2 – fct CoPt(001); 3 – fct CoPt(011); 4 – fct CoPt(110).*

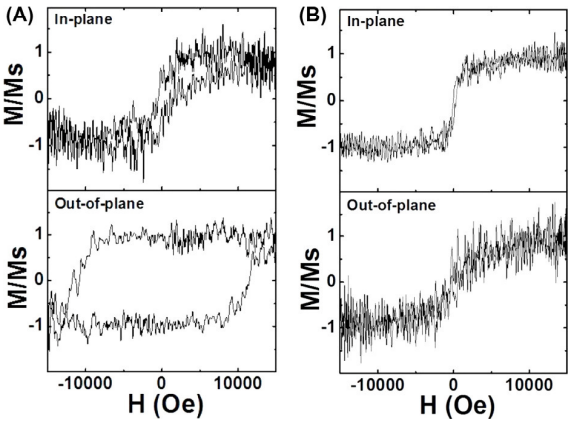

Figure 2 *Vibrating Sample Magnetometry (VSM) results. VSM of nanopatterned CoPt films measured parallel and perpendicular to the surface, respectively (a) heat treated sample, (b) non-heat treated sample.*

Formation and properties of self-forming diffusion barrier layers

(OTKA K 81808)

K. H. Nagy and F. Misják

Cu-Mn films are perspective contact and interconnect material [J. Bogan et.al., J. Appl. Phys. 120 (2016) 105305]. However, their application on low-κ dielectrics (carbon doped oxides, CDO) has difficulties since Mn can react with carbon present in the dielectric, which complicates interface chemistry. Thermal stability and solid phase reaction between amorphous Cu-Mn films and carbon substrates were investigated by in-situ TEM. Amorphous Cu-Mn films (with 50 and 70 at% Mn content) were deposited by DC magnetron sputtering at room temperature. Evaporated carbon foils were used as substrates to model low-κ carbon doped oxides in their reaction with Cu-Mn films. In-situ TEM revealed that the amorphous state is stable below 300°C, where the films crystallize into Cu(Mn) and α-Mn-based solid solutions. While Cu-based solid solution remains stable up to 600°C, Mn-based phases alter. Mn carbide phases appear at 400°C accompanied with the disappearance of α-Mn phase and the decrease of Mn content of Cu(Mn) phase. In the temperature range of 400-500°C $Mn_{23}C_6$ and Mn_5C_2 carbide phases are present. As temperature increases more carbon diffuses into the film and hence the compound of lower C:Mn ratio ($Mn_{23}C_6$) disappears and a new phase of higher C:Mn ratio, the Mn_7C_3 appears. Mn_5C_2 carbides have lamellar structure and show Arrhenius-type grain growth in the temperature range of 400-600°C.

The activation energy of Mn_5C_2 growth is 101±20 and 88±22 kJ/mol respectively in the film containing 50 and 70 at% Mn indicating that carbide growth is facilitated with increasing Mn content. In addition to carbide formation, surface oxidation occurs as well in the system. Thermodynamic considerations indicate that Mn carbide

formation can only occur in the Cu-Mn-C-O system when the Mn is not fully oxidized, and there are free metallic Mn atoms left. Our results suggest that a thin, uniform barrier layer without carbide formation can be formed on the surface of CDOs when sufficient O is available for full oxidation of Mn within diffusion distance to the Cu(Mn)/CDO interface and when the diffusion of Mn into the CDO is prevented.

TEM study of nickel and copper silicides

E. Dodony and Gy. Z. Radnóczi

Microelectronics and semiconductor industry has a growing appetite for the use of nickel and copper silicides in their products, because of their favorable properties. For example, nickel is used for metal induced lateral crystallization (MILC) processes, and nickel silicides in various nano-, and microelectronic devices as contact material. Cu_3Si is used as contact material as well as catalyst in making semiconductor nanowires and ultrapure silicon suitable for photovoltaic devices.

Due to their importance, we have studied formation of nickel and copper silicides in thin amorphous silicon (a-Si) films. A 10 nm thick a-Si film was transferred onto Cu and Ni grids and heated in-situ in a Philips CM20 transmission electron microscope. During heating, the Cu and Ni grids acted as unlimited sources for the diffusion of metals into the a-Si. Copper silicides started forming at 500 ^{o}C, and nickel silicides at 560 $^{\circ}$C. We observed two competing phases, Ni_3Si and one of the low temperature polymorphs of the Cu_3Si (Fig. 1). Both forms are superstructures. Available structural models for both phases were compared to the measurements, and was found that they do not match properly, similarly, as calculated diffraction patterns using published models do not match our experimental data.

Now we focus our efforts to collect diffraction data and high-resolution electron microscopic images of both phases. Our goal is to make new crystal structure models for both the η”-Cu_3Si and Ni_3Si.

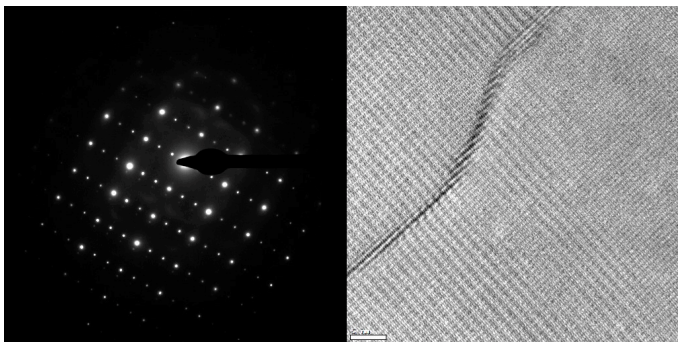

Figure 1 *Diffraction of η”-Cu_3Si [110] projection and a HREM image of the same phase.*

Characterization of defect structure, mechanical properties and stability of electrodeposited nanocrystalline Ni films

T. Kolonits, Zs. Czigány, J. Gubicza (ELTE Univ.), P. Jenei (ELTE Univ.), S. Zsurzsa (Wigner Res. Centre), L. Péter (Wigner Res. Centre), and Bakonyi (Wigner Res. Centre)

Effect of various organic additives on defect structure and mechanical properties of electrodeposited Ni films was investigated by X-ray diffraction (XRD) line profile analysis (eCMWP model), transmission electron microscopy (TEM) and energy disperse spectroscopy (EDS). Main task in the project is to investigate the effect of the additives on the grain structure and defect (dislocation and twin) density which influence macroscopic properties of the layers and their applications.
Electrodeposited layers were prepared at room temperature and at low current density onto copper substrates. The basic electrolyte mainly contained nickel-sulphate ($NiSO_4 \cdot 7\ H_2O$) and boric acid (H_3BO_3). XRD and TEM grain size and phase analysis was carried out to determine the microstructure. Hardness tests were made to examine mechanical properties. Heat treatment (at 500, 750 and 1000 K) was also applied to investigate the stability of the micro and macro properties.

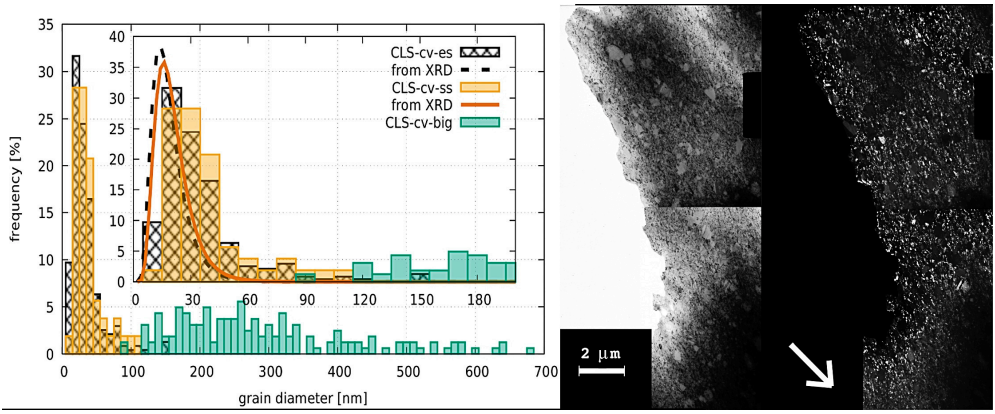

Figure 1 *Grain size distribution of nanocrystalline Ni film deposited from electrolyte based on nickel-sulfate and nickel-chloride with saccharine additive determined by TEM (left). A bimodal grain size distribution can be observed by TEM (right). Arrow indicates the growth direction of the layer.*

According to our former research [T. Kolonits et.al., J Electrochemical Society (2016), 163(3): D107-D114] in the film deposited without additives, a columnar structure was observed, textured into direction <220>. Varying additives in the bath, various microstructures were observed: textured (both in direction <220> or <200>), non-textured, twinned, ultrafine grained and nanocrystalline, etc. EDS revealed that mainly the low quantity of (~0.1 at%) incorporated sulfur, sodium and chlorine is responsible for the different microstructures. Due to the synergic effect of nickel-chloride and saccharin, an interesting bimodal grain size distribution could be

observed: a smaller one due to saccharin, and a larger one corresponding to the effect of nickel-chloride (Fig. 1). Hardness test was compared with the microstructure both before and after heat treatment. One of the additives (trisodium-citrate) showed outstanding hardness and thermal stability, meanwhile in samples deposited with saccharin (which showed the smallest grain size, largest defect density and best hardness) the recrystallization process occurred between 750-1000 K and took place in a few minutes.

New type functional alloy films

(OTKA NN 112156)

F. Misják[1] F,B.R. Braeckman[2] , K.H. Nagy[1], G. Radnóczi[1], D. Depla[2]
[1]MTA EK MFA, [2]Dept. of Solid State Sciences, Ghent University, Belgium

A new type of material, high-entropy alloy (HEA) thin films were investigated in this project. High-entropy alloys processed by non-equilibrium methods such as splat quenching, ball milling or magnetron sputtering exhibit in most cases simple structures. HEA prepared in the form of thin films or coatings can have favourable functional properties like relatively high hardness and plasticity, good electrical or magnetic as well as anticorrosion properties making them suitable for different applications. The phase formation in HEA films depends on the alloy composition and the synthesis methods.

Nb_x-(CoCrCuFeNi) thin films were synthesized by sputtering from compacted powder targets. The films were deposited at room temperature onto Si substrates with a deposition rate of ~10 nm/min. The structure formation mechanism of the Nb_x-CoCrFeNiCu (HEA) model system was investigated by transmission electron microscopy (TEM) to reveal nanostructure of the films. Fig. 1 shows the cross-sectional bright field HR-TEM images and the electron diffraction patterns of the deposited thin films as a function of Nb content. The CoCrCuFeNi alloy without Nb exhibits a single phase face centred cubic (fcc) solid solution [Braeckman BR, et.al., Thin Solid Films 616, pp. 703-710. (2016)]. When adding Nb, the diffraction rings are broadened with increasing Nb content and the higher order diffraction rings eventually vanish. The bright-field images reveal the presence of nanocrystallites in the film with 5, 7, and 9.6 at.% Nb, while films with 15.2 and 24.3 at.% seem amorphous. However, a thorough HREM investigation of the 15.2 at.% sample revealed nanocrystallites of 2–3 nm in size, and with a lattice spacing corresponding to the observed FCC phase in samples with a lower Nb content. These crystallites are embedded into an amorphous matrix. It is also observed that the size and density of the crystallites decreases with increasing Nb concentration [18]. A comparison between grain sizes (as determined from HRTEM, and XRD) is shown in Fig 1f. The XRD grain size was calculated using Scherrer's equation, and a continuous decrease

with increasing Nb concentration is observed. The HREM analysis shows apparently the same result.
Structural changes in the nanostructure as a function of Nb content can be understood from topological point of view: such alloys can be regarded as binary alloys. The addition of Nb with a larger atomic radius (143 pm) as compared with the five base elements (between atomic sizes of 125 and 128 pm) introduces lattice strains. When the Nb concentration becomes too high, the FCC lattice cannot accommodate the atomic level strains, and the amorphous configuration becomes more favourable.

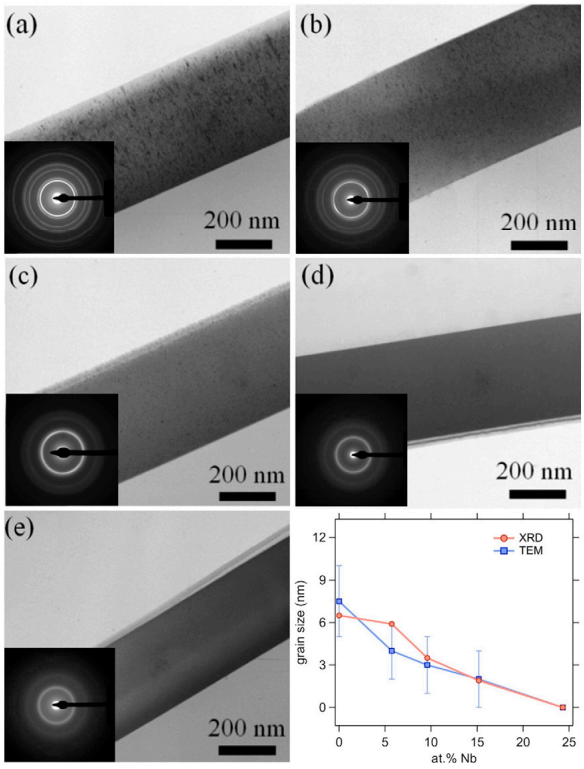

Figure 1 *Cross-sectional bright field TEM images and electron diffraction patterns of the Nbx-(CoCrCuFeNi) thin films for (a) 0 at.% Nb, (b) 5.7 at.% Nb, (c) 9.6 at.% Nb, (d) 15.2 at.% Nb, and(e) 24.3 at.% Nb. The grain size as determined from XRD and TEM is shown in (f). The grain size of the amorphous film with 24.3 at.% Nb was set to 0 nm.*

Graphene-ceramic composites for tribological application in aqueous environments

(M-ERA.NET GRACE, OTKA NN 114422, OTKA PD 121368)

C. Balázsi, O. Tapasztó, Zs. Fogarassy, V. Varga, M. Knoch (FCT), J. Dusza (IMR SAS, Slovakia), A. Kailer (IMW Fraunhofer, Germany), K. Balázsi

Main objective of the project was to develop tribological systems on the basis of functionalized graphene and ceramic-graphene nanocomposites and their qualification for technical applications, e.g., for slide bearings and face seals in aqueous media.

Our current knowledge in the field of ceramic nanocomposites shows that it is possible to make ceramic materials with improved mechanical and tribological properties by incorporating graphene both into the Si_3N_4 (Fig 1) and the SiC structure. During the last period, we tested six different types of graphene as additions in SiC and Si_3N_4. The multilayered graphene (MLG) was prepared by attritor milling at 10 hours intensive milling of few micrometer sized graphite powders in large quantities (few kilograms). The large quantity, very cheap and quick preparation process are the main strengths of our MLG. The Si_3N_4/MLG and SiC/MLG nanocomposites were prepared by attritor milling and sintered by hot pressing (HP) in Slovakia (laboratory scale, diameter of samples was 3 cm) and in FCT lab, Rödental (industrial scale, for industrial testing). The laboratory scale Si_3N_4 ceramics were produced with 1 wt%, 3 wt%, 5 wt% and 10 wt% content of MLG. In all composites, densities between 97 and 100 % were obtained.

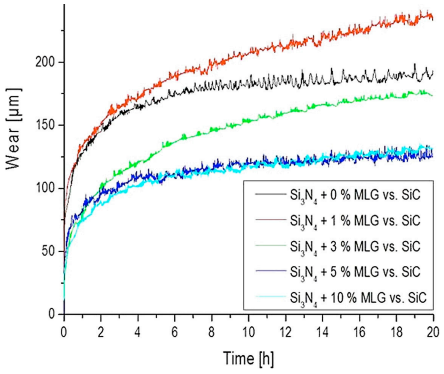

Figure 1 *Development of the total wear depth of the multilayered graphene containing Si_3N4-pins on SiC-rings and structure of Si_3N_4/ 5 wt% MLG.*

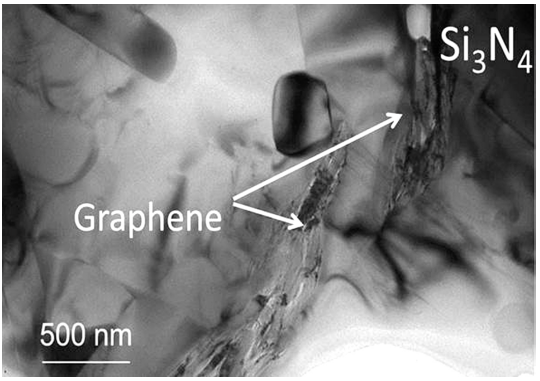

Figure 2 *TEM image of Si_3N_4 / 5 wt% MLG showed the dispersion of MLG between silicon nitride grains after milling and sintering.*

The α-Si_3N_4 to β-Si_3N_4 phase transformation was completed during hot pressing. The structural investigations and phase analysis measurements confirmed the presence of MLGs in all composites after the HP sintering process (Fig. 2). Presence of very fine nanostructred zirconia on the silicon nitride grains is the consequence of the highly efficient milling process. HV values decreased with increasing of MLG content from 18.86 GPa to 9.69 GPa. The small increase to 18.86 GPa of HV at 1wt% MLG content in comparison to 17.01 GPa reference Si_3N_4 might be attributed to smaller grain sizes. The results showed that improved tribological properties, more stable frictional behaviour and a significant increase of the wear resistance at MLG contents beyond 5 wt% can be achieved (Fig. 1). This new approach is very promising, since ceramic microstructures can be designed with high toughness and provide improved wear resistance at low friction [7,134].

New approaches in the development of Hypoallergenic implant material in Orthopaedics: steps to personalised medicine

(EU FP7 HypOrth 602318)

K. Balázsi, N. Oláh, Zs. Fogarassy, V. Varga, T. Sopcák, T. Zagyva, L. Illés, D. Delfonse (Mathys, Switzerland), C. Lohman (Magdeburg Un., Germany), J. Lorenzen (Teknologisk Inst., Denmark), A. Wielowiejska-Giertuga (INOP, Poland), Cs. Balázsi

Joint replacement is one of the most successful in current orthopaedics. Although many improvements have been made, tissue reactions to biomaterials, infection and lacking osseointegration are still the main reason for the failure of implants and for revision surgery. Various materials - considered as "ideal" to wear resistance (e.g., CoCr-alloys) or "bioinert" (Ti-alloys) – are found to induce adverse tissue reactions or to support biofilms. Patients with a known metal allergy are at a higher risk of developing sensitivity against biomaterials. HypOrth project helps understanding local adverse reactions around artificial joint replacements and to improve integration of potential hypoallergenic implants with improved biocompatibility.

HypOrth has already developed bioactive implant surfaces including bioceramics. Those surfaces and implant materials are being tested in material tests as well as cell culture experiments. From these results, prototypes are being designed. A very unique surface coating will be realized by using eggshells and seashells as a source for calcium/hydroxyapatite coating to enhance osteointegration and mimic biocompatibility. This technology has been proven to be efficient and effective in simulator tests.

It can be assumed that the initiative HypOrth has direct impact on the health of European citizens but also on the technology transfer by stimulating metal forming industries. Already today, the prototype surfaces are expected to show superior properties as compared with existing technologies. The main part of the project´s results is confidential.

Investigation of Biocompatible Glasses for Biomedical Applications

V.K. Kis, M. Fábián, J. Lábár, I. Székács, A. Sulyok, Zs. Dallos, Zs. Horváth, F. Misják and Zs. Kovács

Synthesis and optimization of Ca and P containing bioactive glasses which, due to their composition, structure and mechanical properties, are suitable for biomedical application. Bioactive glasses has been prepared by melt-quench technique in the compositional range $SiO_2(45)CaO(25)Na_2O(30\text{-}x)P_2O_5(x)$, x=0, 1, 3, 5. Using DTA/DSC analysis, the glass transition and crystallization temperatures were determined for the different samples. Mechanical properties, such as Vickers hardness

and Young's modulus were measured by nanoindentation tests at different positions in the as-cast glasses.

Structure of the bioactive glasses was characterized using electron and neutron diffraction. TEM studies supported amorphous structure on the nanoscale in case of glasses with 0, 1 and 3 mole% P content, while the sample with 5 mole% P, contained nanocrystals with size <30 nm (Fig. 1). Partial atomic correlation functions and coordination numbers were revealed from RMC modelling based on neutron data (Fig. 2). Structure forming bonds of Si–O and P-O exhibit narrow distance distribution, while those corresponding to Ca–O, Na–O and O-O bonds show broader and more asymmetric distributions.

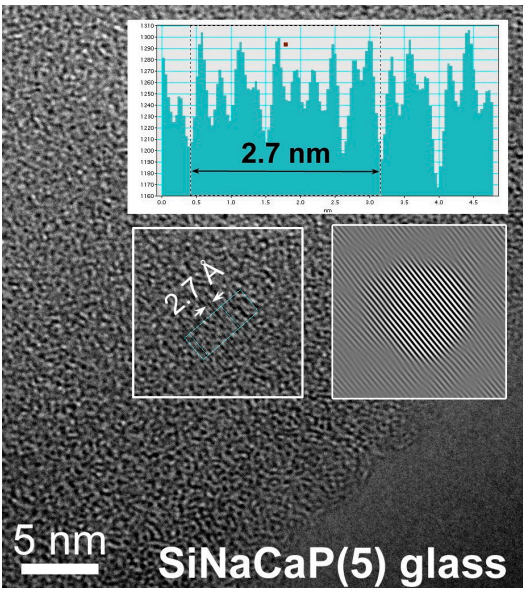

Figure 1 *HRTEM: Nanocrystal in bioglass with 5 mole% P.*

Interference functions and e-PDFs obtained from NBD were compared with bulk neutron RMC results. To validate e-PDF analysis, the effect of sample thickness and mean free path was analysed using a reference pure SiO_2 glass with different thickness at 200 and 300 keV. The probe size was 1.5 µm and 25 nm in case of 200 keV and 300 keV respectively. According to our results the atomic distances obtained from e-PDFs are in good agreement with neutron based RMC data and independent of sample thickness and the applied Q-range. Thus, e-PDF proved to be suitable for semi-quantitative characterization of amorphous structure on the nano scale. e-PDFs of the 5 mole% P sample obtained from NBD using 25 nm probe size at 300 keV imply inhomogenities in the amorphous structure which is in agreement with HRTEM observations.

To test the bioactivity of the glasses, samples have been treated in simulated body Fluid (SBF, following the protocol of Kokubo and Takadama, 2006) for different soaking times (3h, 3days, 7days, 21 days). After three hours all P containing samples exhibited a Ca and P rich layer on their surface, which proves the bioactivity of the glasses. At the same time, on the surface of the P-free glass a silica-rich layer was

formed. According to XPS, this silica-rich layer contains Mg and P, which implies the ion-exchange between SBF and glass.
Characterization of the bioactive layer as a function of composition and soaking time in comparison to bone mineral component is still in progress. A 30 min soaking experiment is also planned parallel to nanoindentation measurement to reveal the initial stage of glass transformation and related changes of mechanical properties in SBF.

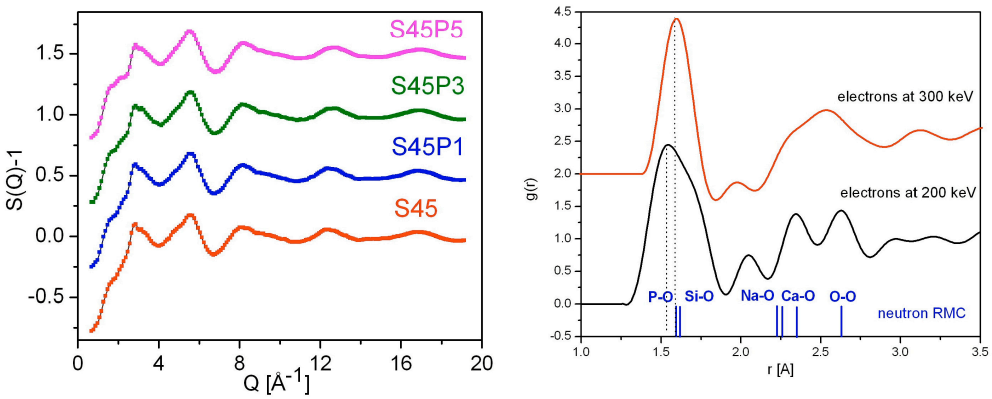

Figure 2 *(left): Neutron diffraction structure factors, experimental data (colour) and RMC simulation (black solid line). (right): Comparison of total pair distribution functions from electron and neutron diffraction data (local vs. bulk, respectively) in the 5 mole% P content sample (S45P5) indicate the spatial inhomogeneities observed by HRTEM.*

Development and characterization of multi-element doped hydroxyapatite coatings on metallic implant materials

M. Furkó and Cs. Balázsi

The aim of this research work is to develop coatings onto implant materials which possess simultaneous antimicrobial and biocompatible properties. The coatings were prepared by applying pulse current deposition technique (Fig. 1). The pure hydroxyapatite (Hap) layer was doped and co-deposited with Ag^{+}, Zn^{2+}, Mg^{2+} and Sr^{2+} ions (multi-element Hap, mHap). The corrosion and biodegradable properties of the layers were studied by carrying out potentiodynamic polarization measurements in simulated body fluid (SBF) using three-electrode open cell over a long time period. The biocompatible characteristics of the layers were investigated by seeding osteoblast-like MG-63 cells onto the sample surface.
Fig. 2 clearly demonstrate that the most corrosion resistant material is the substrate (Ti6Al4V) while the least corrosion resistant (the highest corrosion current measured) is the multi element doped HAp coating, proving its biodegradable properties.

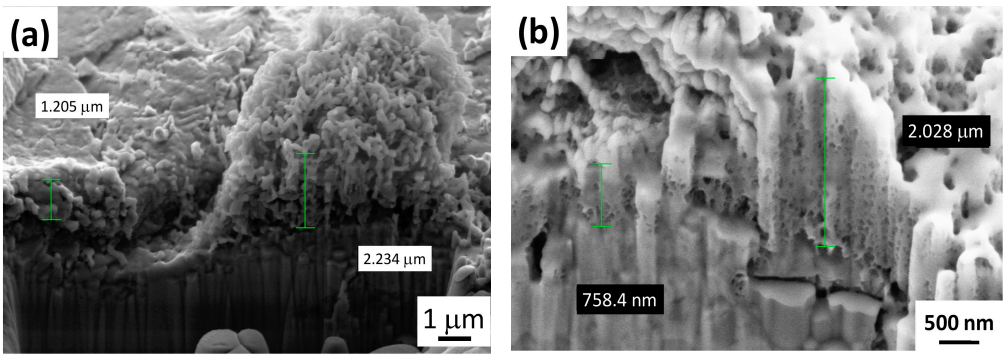

Figure 1 *SEM-FIB images on HAp coating* ***(a),*** *and on multi-element doped HAp* ***(b)****.*

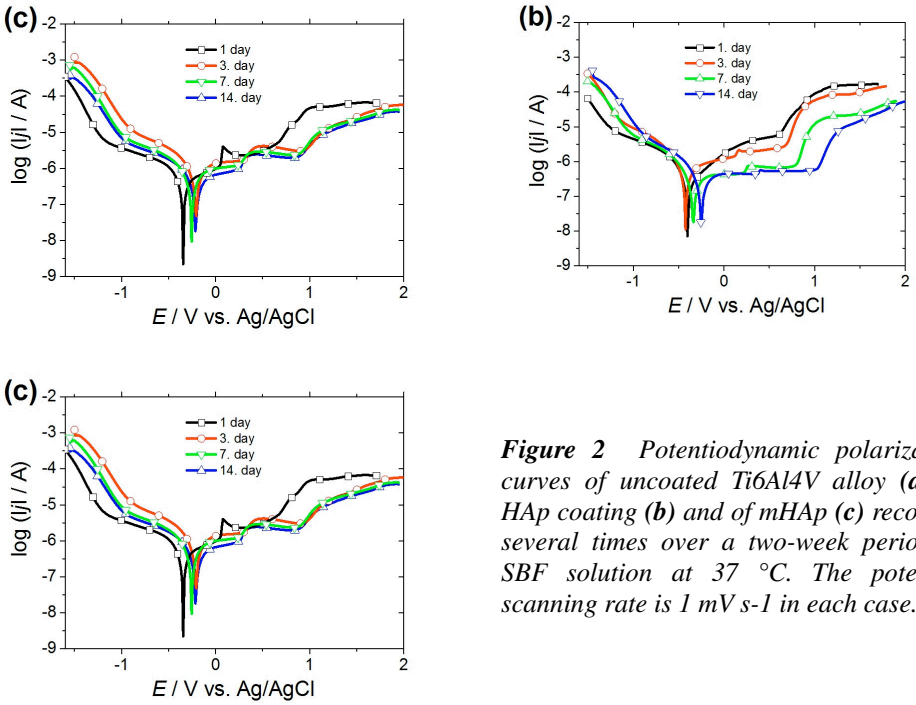

Figure 2 *Potentiodynamic polarization curves of uncoated Ti6Al4V alloy* ***(a)*** *of HAp coating* ***(b)*** *and of mHAp* ***(c)*** *recorded several times over a two-week period in SBF solution at 37 °C. The potential scanning rate is 1 mV s-1 in each case.*

Development of protective TiC/a:C thin films prepared by DC magnetron sputtering

N. Oláh and K. Balázsi

Most of the metallic medical implants are made of titanium (Ti) or of its various alloys because of the favorable biocompatibility. However, after implantation, Ti ions

(and / or alloying elements) can be detected in the body – due to corrosion or metal scraping – which may cause inflammation, and may lead to allergic symptoms, or in the worst case, the implant must be removed. In order to increase the metal insulation, corrosion resistance, and thus biocompatibility, several methods can be used. One of them is the passivation of the surface with different nanocomposites. Ceramic titanium carbide / amorphous carbon (TiC/a:C) protective nanocomposite thin film may be a potential candidate for such a surface protection coating to the different implant materials serving as barrier layer. The main goal of this work was to develop and produce TiC/a:C nanocomposite thin film coatings by DC magnetron sputtering, electron microscopic examination of growth mechanisms, determination of relationship between the structure and the physical - biological properties, as well as the sample preparation.

It was shown that the TiC/a:C thin films produced by DC magnetron sputtering at room temperature follow the morphology characteristic of the two- component system zone diagram but they do not follow the phase transformations expected based on the macroscopic Ti - C phase diagram. Based on structural examination it was found that the globular TiC nanocrystals began to take shape until 25 W of Ti target power and above this value, the films were grown by columnar crystals. The diameter of the columns increases with the thickness increase, the higher the Ti content is widening faster. As the Ti content increased, the thickness of the amorphous carbon matrix decreased from 10 nm to 1 – 2 nm and the size of the TiC nanocrystals grew from ~ 0.5 nm to 26 nm (Fig.1). FFT confirmed the presence of the only identifiable face-centered-cubic (fcc) TiC crystal phase. Further increasing of Ti content, up to ~ 60 at% showed the disappearance of amorphous carbon from the full length TiC columns, and any other Ti phase, such as hcp Ti, was not manifested.

The effect of TiC/a:C thin films on the mechanical (hardness (H), modulus of elasticity (E)) and tribological properties was also analyzed and it was detected that these properties show a distinct variation depending on Ti content. The highest H of ~ 26 GPa and E of ~ 140 GPa with friction coefficient of 0.268 was observed in case of the film prepared at ~ 38 at% Ti content (Fig. 2).

Most important result of the corrosion tests was that the TiC/a:C protective coating on various substrates, while providing a high hardness to the surface, was also sensitive to electrochemical processes. The TiC/a:C coated sandblasted TiAl6V4 alloy possesses the highest polarization resistances over time while the lowest resistances belong to coated polished wafers. It was observed from the ICP-OES results that the TiC/a:C coated sandblasted TiAl6V4 alloy prevents dissolution of both Ti and Al into simulated body fluid.

Based on the biocompatibility and viability tests of the thin films, it was found that the cells like the surface of the coating, are proliferated on the TiC/a:C thin film, so the films become non-toxic, biocompatible and the viability of the cells is excellent after 3 days. Furthermore, based on the results of the hydrophilicity tests on the coatings it was found that all films exhibited hydrophobic behavior regardless of the composition [90].

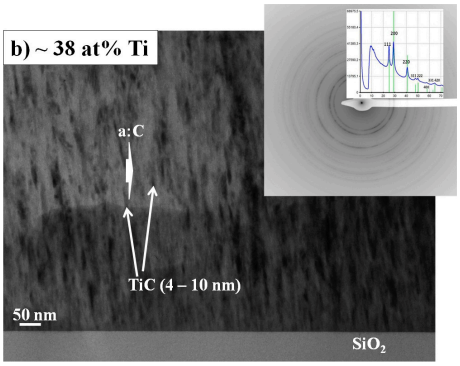

Figure 1 *Cross section TEM image of TiC/a:C thin film d*eposited consisted at 40 W PTi.

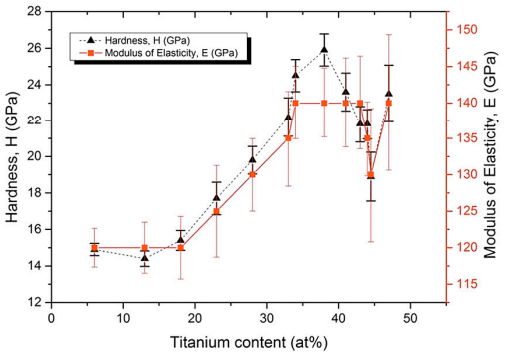

Figure 2 *Effect of structure on mechanical properties of TiC/a:C thin films.*

Effect of oxidization of Si_3N_4 particles on structure of sintered Si_3N_4 ceramics

A. Qadir, K. Balázsi, and Cs Balázsi

Materials made of silicon nitride (Si_3N_4) are used in high-temperature oxidizing environment, thus, it is necessary to investigate the oxidation mechanism on structural, mechanical and tribological properties. The effect of hot isostatic pressing (HIP) on nanosized oxidized silicon powder particles on the structural and mechanical properties of Si_3N_4 was studied. The starting α-Si_3N_4 powders were oxidized for 10 and 20 hours at 1000 ˚C in ambient air. Amorphous oxide layer formation was observed on the surface of Si_3N_4 powder particles by high resolution transmission electron microscopy (HRTEM). Thickness of the oxide layer on the surface of powder particles increased with oxidation time. These powders were densified at 1700 ˚C in nitrogen gas environment under 20 MPa for 3 hours using HIP technique. The complete α to β transformation was observed in Si_3N_4 samples which were sintered at 1700 ˚C under 20 MPa for 3 hours. Silicon oxynitride (Si_2N_2O) phase was found in sintered samples and the amount increased with the oxidation time (Fig. 1). The β phase decreased with the increase of Si_2N_2O phase in the sintered samples. We showed that the oxidation influenced the mechanical properties of sintered composites as well. The flexural strength of samples at 1700 ˚C sintering temperature is higher due to the higher amount of β- Si_3N_4 phase than that of samples which were sintered at 1500 ˚C. Decreasing tendency in flexural strength of the samples was observed with oxidation time. Higher amount of oxygen in the base powders results in higher tendency of formation of Si_2N_2O in the sintered Si_3N_4.

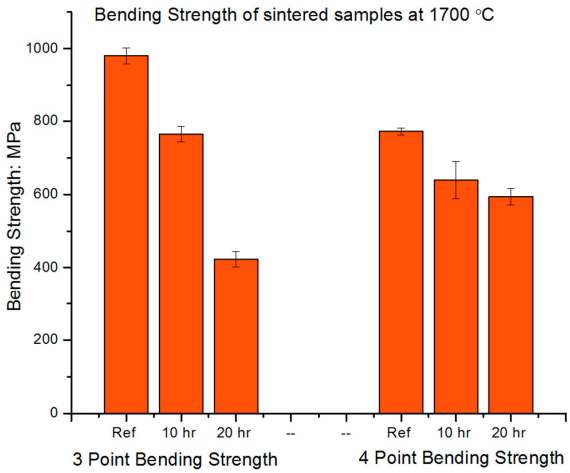

Figure 1 *The bending strength of sintered samples decreased with the increase of oxidation time.*

Advanced ceramic and their composits for energy application

S. Lamnini, K. Balázsi and Cs. Balázsi, Zs. Fogarassy, E. Zs. Horváth, and S. Tóth

Several applications in energetics are known where yttria-stabilized zirconia (YSZ) and zirconia / multiwall carbon nanotube (MWCNT) composites were useful used as parts of solid oxide fuel cells (SOFC), photovoltaic solar cells, supercapacitor or hydrogen storage materials. The Ni – YSZ cermets are widely accepted as anodic materials in SOFCs with high catalytic activity and electrical conductivity. Research works showed drawbacks when with hydrocarbon fuels carbon build-up, sulfur poisoning or low tolerance to redox cycling is found. These irreversible processes damage the microstructure of anodes and reduce cell performance, therefore, Ni-free anode materials are continuously researched for and developed to overcome these problems. In this work, milled YSZ / MWCNT composites were studied. The effect of attritor milling on structure of 8 mol% yttria-stabilized zirconia (8YSZ) composites with 1wt%, 5 wt% and 10 wt% MWCNTs addition was studied. In all cases, a high dispersivity of the particles with a sharp and irregular shape was found, while the as-received MWCNTs were observed as clusters forming bundles of 2.5μm in length. Raman measurements showed results also supporting structural observations. The apparition of the G and D bands for all the composites at ~1589cm−1 and ~ 1356cm−1 confirmed the structural integrity of MWCNT after the milling process as well. The next step will be the sintering of milled composites by spark plasma sintering and study effect of MWCNT addition on density and electrical properties.

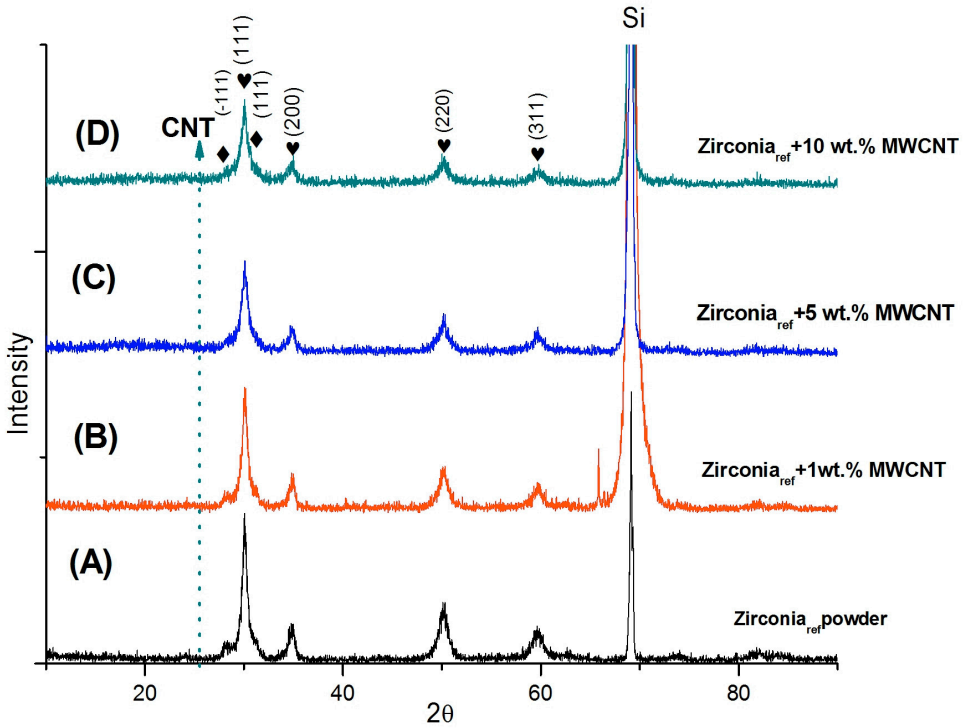

Figure 1 *XRD measurements of YSZ/MWCNT compositesafter 5h intensive attritor milling.*

Effect of Si_3N_4 addition on the morphological and structural properties of the 316L stainless steel for nuclear applications

H. R. Ben Zine, K. Balázsi, and Cs. Balázsi, F. C. Sahin (ITU), Z. E. Horváth, Z. Czigány, and Á. Horváth

316L austenitic stainless steel has attracted attention due to its good mechanical properties at high temperatures, good corrosion resistance and good weldability, which can be an effective solution for several industrial applications. Effect of addition of submicron sized Si_3N_4 on the morphological and structural properties of the ceramic dispersion strengthened (CDS) 316L stainless steel prepared by powder technology was studied. Two composites were prepared; 316L/0.33 wt. % Si_3N_4 and 316L/1 wt. % Si_3N_4. In order to assure a good dispersion of the ceramic particles in the stainless steel powders and a grain size reduction at the same time, highly efficient attrition milling was used. It was found that 5 hours milling in ethanol at 600 rpm and using 3 mm grinding stainless steel balls was sufficient to obtain grains with flake-

like shape in case of 316L/0.33wt. % Si_3N_4. Spark plasma sintering (SPS) was used for fast sintering of milled composites.
The samples have been sintered under 50MPa at 900C° for 5 minutes in vacuum. Structural and morphological changes were studied after milling and sintering process. It was found that the amount of Si_3N_4 addition influenced the efficiency of milling process resulting in powder mixtures with different 316L stainless steel grain size and shapes. In the case of 0.33 wt. % Si_3N_4 addition (Fig. 1). The intensive milling assured an optimal coverage of 316L stainless steel grains with submicron sized Si_3N_4 particles in both cases, as demonstrated by EDS and TEM. In this case, the fracture is propagating through both intergranular or transgranular paths as shown in Fig. 2. The slightly damaged globular grains covered with Si_3N_4 particles clearly affected the fracturing behaviour as the SEM images shows a dominance of the intergranular fracturing with the presence of very few transgranular fracturing [106].

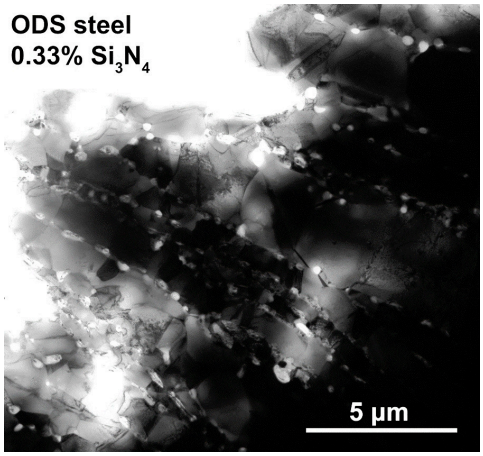

Figure 1 *TEM images of sintered samples. a) 316L/0.33wt. % Si_3N_4.*

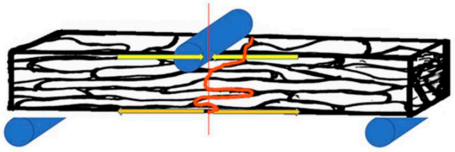

Figure 2 *Schematic representation of the dominant fracturing behaviour. in the case of the 316L/0.33wt. % Si_3N_4.*

Adhesion model of graphene islands on metal substrates based on Moiré-patterns

M. Szendrő and P. Süle

One problematic aspect of graphene (GR) CVD growth on metal substrates is that GR is capable to create rotational domains, separated by grain boundaries (GBs), sometimes even on a single crystal surface. GBs worsen the electric properties of GR, therefore the nucleation of differently orientated islands is an undesirable phenomenon.
An interesting feature is, that the different existing orientations are very specific to the substrate (e.g: on Cu(111) the most commonly known orientations are: R0°, R7°, but for Ir(111) we have R0°, R14°, R19°, R23°, R26°, R30°). We are not aware of a

physical model that can somehow clarify the very basic nature of these orientations. Why only these orientations can appear, and what are circumstances that influence GR to form one or another orientation?

In order to understand these aspects a continuum mathematical model was developed which calculates the adhesion energy of a GR island with a given size and orientation based only on knowledge of the underlying Moiré-pattern which is formed among atomic lattices. This approach agrees surprisingly well with DFT and CMD results. This shows that we have captured some very basic physical insights of the adhesion.

Using our model, Monte-Carlo (MC) simulations can be carried out to perform GR growth simulations on several nuclei to analyze their distribution of orientation (Fig. 1). These MC simulations are several orders of magnitude faster than Kinetic MC methods (Fig. 2).

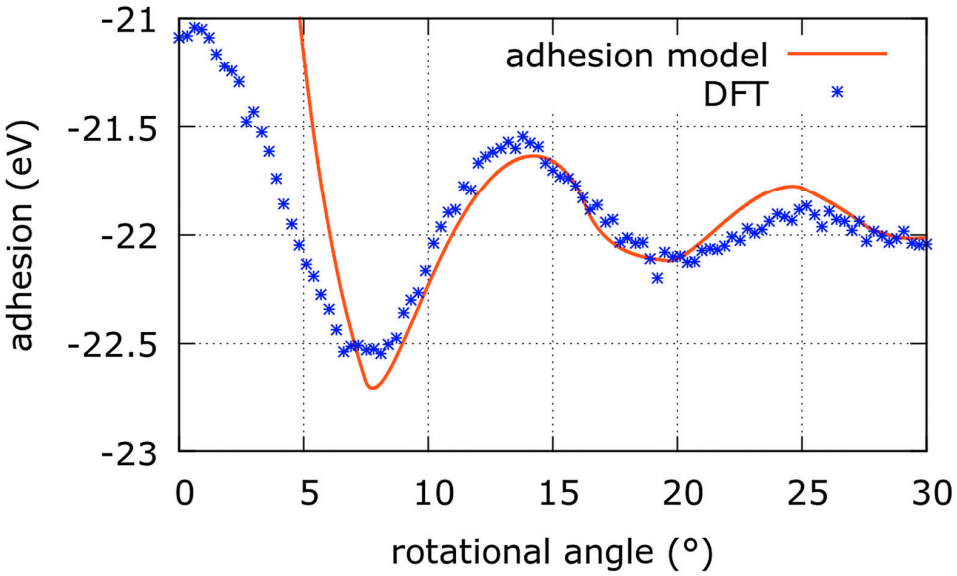

Figure 1 *The dependence of the adhesion on the orientation of a GR nanoisland with a diameter of 2.2 nm on Cu(111) surface. Our model (red line) is compared to DFT calculations (blue spots).*

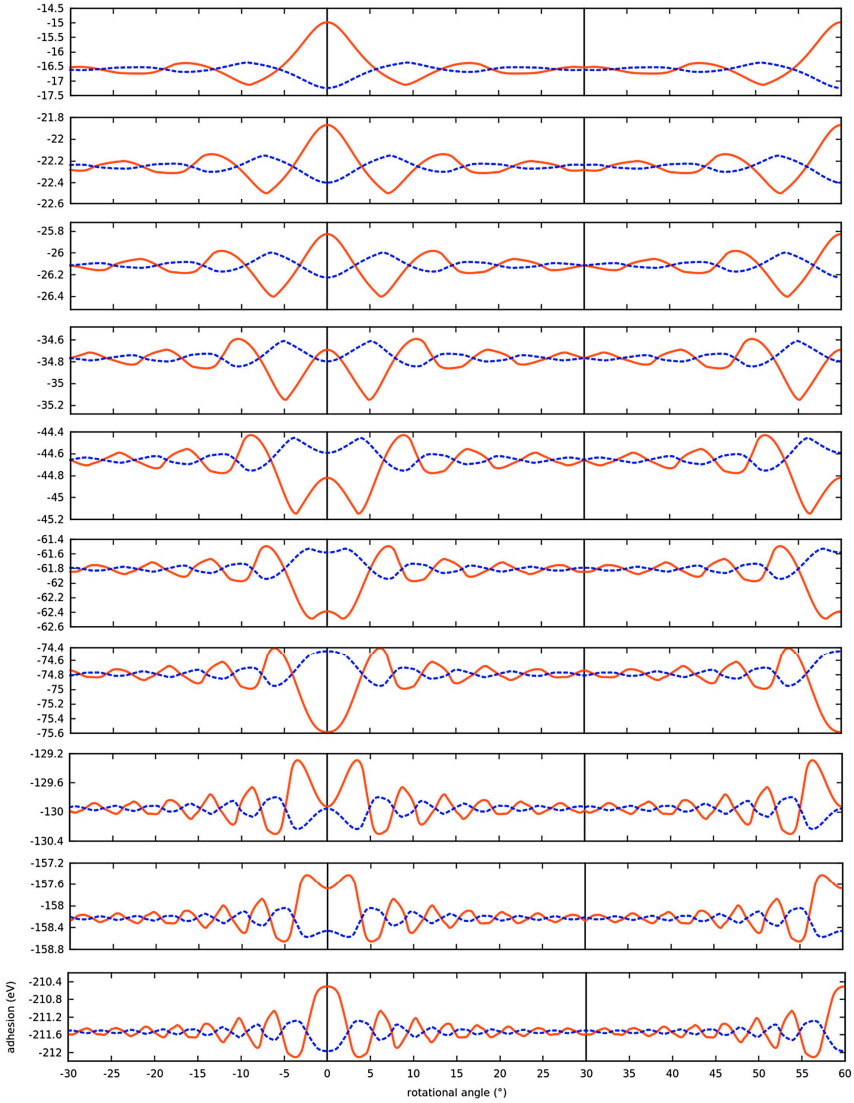

Figure 2 *The behavior of the rotational energy spectrum of a hollow (red line) and a hcp stacking island (blue line) when increasing the size (from top to bottom) according to our model. The spectrums of the two types of islands are almost mirror images of each other. During growth the number of energy minimums increases. The 30° is the source of the minimums: as the island grows new minimums appear at 30°, then they travel towards 0°. When two hollow minimums get close enough to 0° they unite and change the hollow maximum to a minimum and vice versa for the hcp type. This means that 0° is a dynamic minimum.*

One-sample combinatory for high throughput TEM- and other analytical studies of thin binary layer systems

G. Sáfrán, T. Lohner, M. Serényi, P. Petrik, B. Kalas, Zs. Zolnai, and J. Gubicza

Our aim was to effectively study the concentration dependent properties of two component thin layer systems. We worked out a high throughput method, so called micro-combinatory, based on the "one-sample concept" i.e., a single gradient sample condenses the whole binary system of components A and B where A_xB_{1-x} (x=0...1) with a geometry that fits the actual analytical measuring technique. The patented method [G. Sáfrán: Hung. Patent, P 15 00500 (2015)] enables a comprehensive study within one specimen within a single measuring session. A specific advantage of μ-combinatory is that the phases of the binary film are formed and investigated side by side, in a single TEM grid that provides superior reproducibility and a straight comparison. The all-in-one feature is very efficient; only one sample is to handle, there is no need for laborious preparations replacement and study of a series of TEM samples. The consistency, and known concentration profile of μ-combinatorial samples are an invitation to high throughput automated TEM. That may be implemented by combining computerized stage positioning, precession electron diffraction and digital image storage and processing.

For a demonstration of the micro-combinatorial method and because of the technological importance Si-Ge binary films were studied by TEM, RBS, and ellipsometry and nanoindentation to reveal the correlation of composition, structure,optical and mechanical properties (Fig. 1).

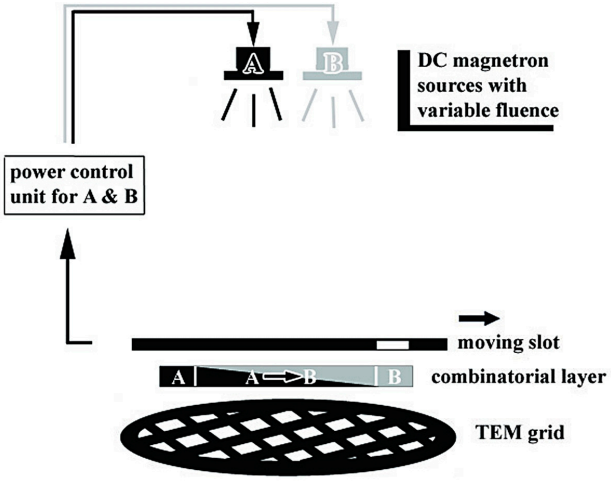

Figure 1 *Set-up of micro-combinatorial deposition for TEM samples. For RBS, ellipsometry, nanoindentation, and XRD the sample size is scaled up from 3 mm diameter to 25x10 mm^2. The combinatorial layer track consists of three sections; sections of components A and B and in between a gradient section of A-to-B.*

Research of thin SiGe layers is strongly motivated due to potential of widespread applications, e.g., solar cells, thin film transistors, Schottky diodes, thermal sensors, bolometers. The present study spans the whole cc. range, of the SiGe binary system,

while earlier studies cover only the low Ge-content range. Besides, due to enhanced non-linear properties of Ge to Si, layers of higher Ge content are of interest in development of optoelectronic devices for the mid-infrared region [Carletti, et al. Opt. Express, 23 (2015) 32202].

A reveal of the concentration dependent properties of SiGe-on-Si provides the fine tuning of the properties – band gap (Fig. 2 and 3), refractive index – as well, the extension of the range of operation up to 8 µm, the Si absorption wavelength, or to 14 µm, the Ge transparency cut-off (Fig. 4 and 5) [M. Brun, et al. Opt. Express 22, 508 (2014)],[M. Ramirez, et al. Opt. Express 25, 6561-6567 (2017)]. The development of the µ-combinatorial method and device was done in co-operation of MFA and Holocom in a GINOP [Hung. Dev. Innov. Op. Prog. GINOP-2.1.7-15-2016-02073].

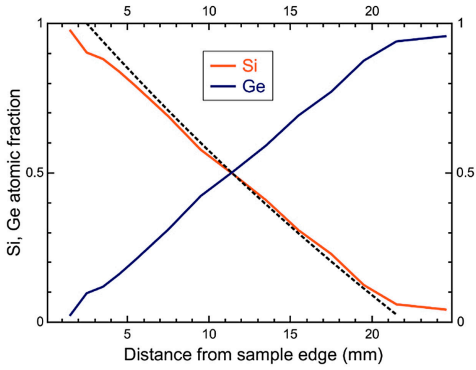

Figure 2 *Linear concentration distribution and optical band gap of DC magnetron sputtered Si-Ge obtained by RBS.*

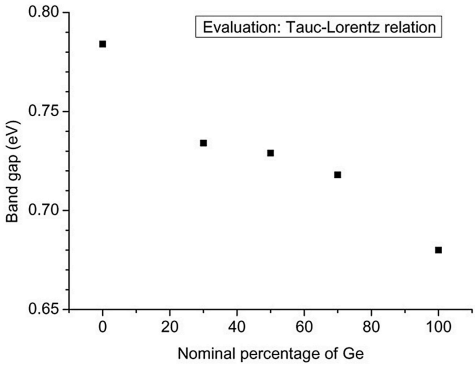

Figure 3 *Ellipsometry as a function of Ge-concentration measured in a 25x10 mm^2 size µ-combinatorial sample.*

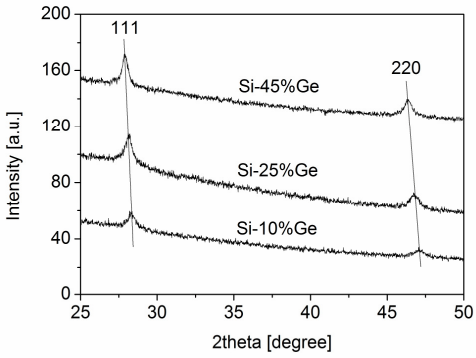

Figure 4 *XRD diagrams and the 111 and 220 peak distances of a Si-Ge sample crystallized at 800°C.*

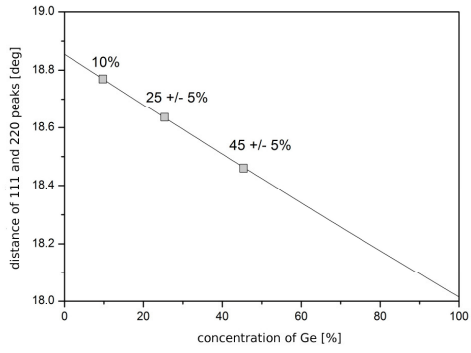

Figure 5 *Linear lattice parameter change with Ge concentration.*

Nanobiosensorics Group

Head: Dr. Róbert HORVÁTH, Ph.D., senior research fellow

Research Staff

- Sándor KURUNCZI, Ph.D.
- Inna SZÉKÁCS, Ph.D.
- Beatrix PÉTER, Ph.D.

Ph.D. students / Diploma workers

- Boglárka KOVÁCS, Ph.D. student
- Enikő FARKAS, Ph.D. student
- András SAFTICS, Ph.D. student
- Tamás GERECSEI, Ph.D. student
- Nicolett KANYÓ, diploma worker
- Kristóf KLIMENT, diploma worker
- Bálint KOVÁCS, diploma worker
- Aurél PRÓSZ, diploma worker
- Olga NÉMETH, diploma worker
- Brgitta RUSZNÁK, diploma worker
- Milán SZTILKOVICS, diploma worker
- Barbara TÜRK, diploma worker
- Anna FORGONY, diploma worker
- Kinga Dóra KOVÁCS, diploma worker
- Zsófia MAGYAR, diploma worker

The research profile of the Nanobiosensorics Group is the development and application of label-free optical biosensors, the mathematical modeling of the relevant biological and biophysical processes. Building on their broad national and international collaborative network the group conducts research in the fields of instrument development, monitoring of cell secreted extracellular vesicles, development of protein-based functional coatings, adhesion studies on human cancer and immune cells, and theoretical modeling. In 2014, the application for an ERC Consolidator Grant by the head of the research group received qualification category "A (fully meets the ERC excellence criteria and should be funded if sufficient funds are available)" after the interview in Brussels, but the funding line did not reach this proposal due to budgetary constraints. However, using this achievement the Group could successfully apply for funding from NKFIH in the framework of the ERC_HU call. In the framework of this project they aim single cell manipulation and label-free sensing.

Biophysical characteristics of proteins and living cells exposed to the green tea polyphenol epigallocatecin-3-gallate (EGCg): Review of recent advances from molecular mechanisms to nanomedicine and clinical trials

(Lendület LP2012-26/2012)

B. Péter, Sz. Bősze (ELTE), and R. Horváth

Traditionally, tea was drunk to eliminate toxins, to improve blood flow and resistance to diseases, so its habitual consumption has long been associated with health benefits. Among natural compounds and traditional Chinese medicines, the green tea polyphenol epigallocatechin gallate (EGCg) is one of the most studied active substance. Tea catechins, especially (-)-EGCg, have been shown to have various health benefits, for example anti-metastasis, anti-cardiovascular, anti-cancer, antiinflammatory and antioxidant effects (Fig. 1).

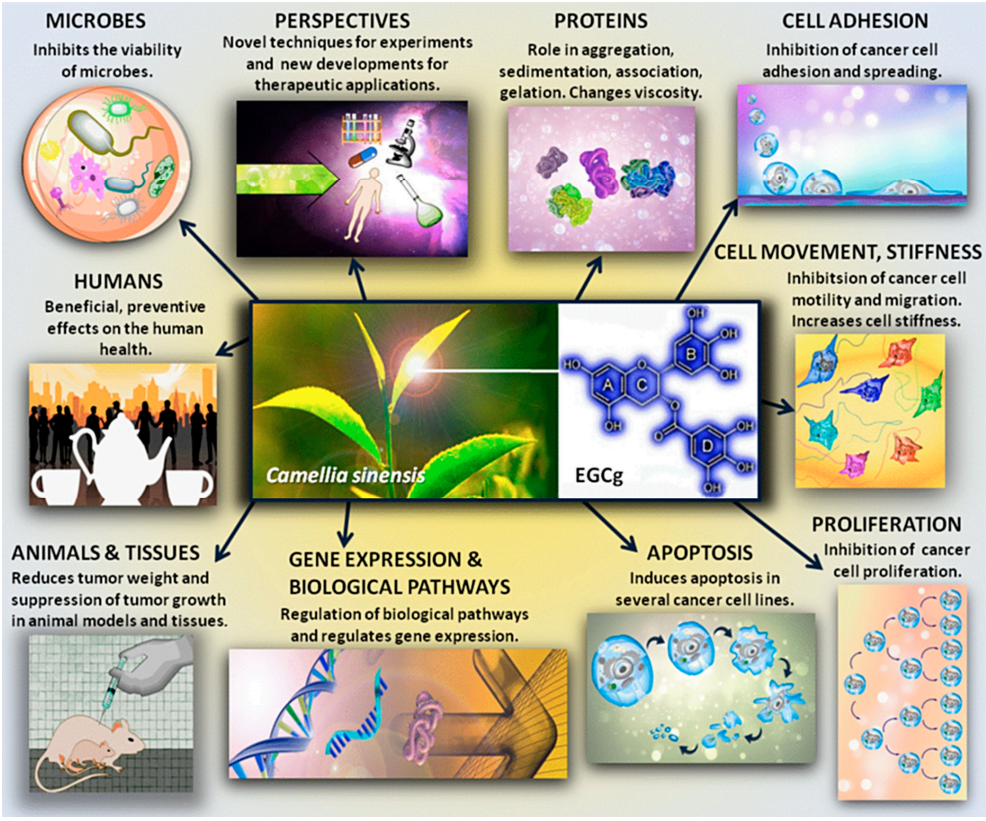

Figure 1 *Diversified effects of EGCg [98].*

In 2015 we focused on the molecular scale interactions between proteins and EGCg with special focus on its limited stability and antioxidant properties, the observed biophysical effects of EGCg on 112 various cell lines and cultures. The alteration of cell adhesion, motility, migration, stiffness, apoptosis, proliferation, as wells as the different impacts on normal and cancer cells are all summarised in our prospective review article. We also handled the works performed using animal models, microbes and clinical trials. Novel ways to develop its utilization as therapeutic purposes in the future are discussed too, for instance, using nanoparticles and green tea polyphenols together to cure illnesses, and the combination of EGCg and anticancer compounds to intensify their effects. In this review we summarize the experiments and results of the past few years. The limitations of the employed experimental models and the criticisms on the interpretation of the obtained experimental data are summarized as well. We also pointed out some inaccuracies in the literature.

Green tea polyphenol tailors cell adhesivity of RGD displaying surfaces: multicomponent models monitored optically

(Lendület LP2012-26/2012)

B. Péter, E. Farkas, E. Forgács, A. Saftics, B. Kovács, S. Kurunczi, I. Székács, A. Csampai, Sz. Bősze (ELTE), and R. Horváth

A wide range of experimental methods are available to measure cell adhesion and cell–surface interactions, however, most of them have serious disadvantages when a multicomponent model of cell adhesion has to be quantitatively investigated in a reasonable time frame. (For example, labeling techniques use fluorescent markers that may affect normal cell behavior and the imaging time is often limited by the bleaching of the marker). In contrast, we highlighted the remarkable potentials of high-throughput resonant waveguide gratings in studying multicomponent model systems of cell–surface interactions. The interaction of the anti-adhesive, antifouling coating, PLL-g-PEG and its RGD (Arg-Gly-Asp) functionalized form, PLL-g-PEG-RGD, with the green tea polyphenol, EGCg was in situ monitored. Right after, cellular adhesion on the EGCg exposed coatings was recorded in real-time (Fig.1). The plate based sensor configuration allowed following the above processes with different surface coatings, EGCg states and concentrations in a single run, on the same biosensor plate. Despite the reported excellent antifouling properties of the above polymer coatings, EGCg strongly interacted with them, and affected their cell adhesivity in a concentration dependent manner. The differences between the effects of the freshly prepared and oxidized EGCg solution could be also first demonstrated. The measured interactions were significantly stronger for the oxidized EGCg solution, highlighting the importance of storage conditions of EGCg solutions, often overlooked in present literature. Using a semiempirical quantumchemical method we showed that EGCg binds to the PEG chains of PLL-g-PEG and PLL-g-PEG-RGD by

hydrogen bonds. Moreover, the calculations illuminated the differences in binding affinity between the fresh and oxidized EGCg, well supporting the experimental findings. Our work lead to a new model of polyphenol action on cell adhesion ligand accessibility and matrix rigidity.

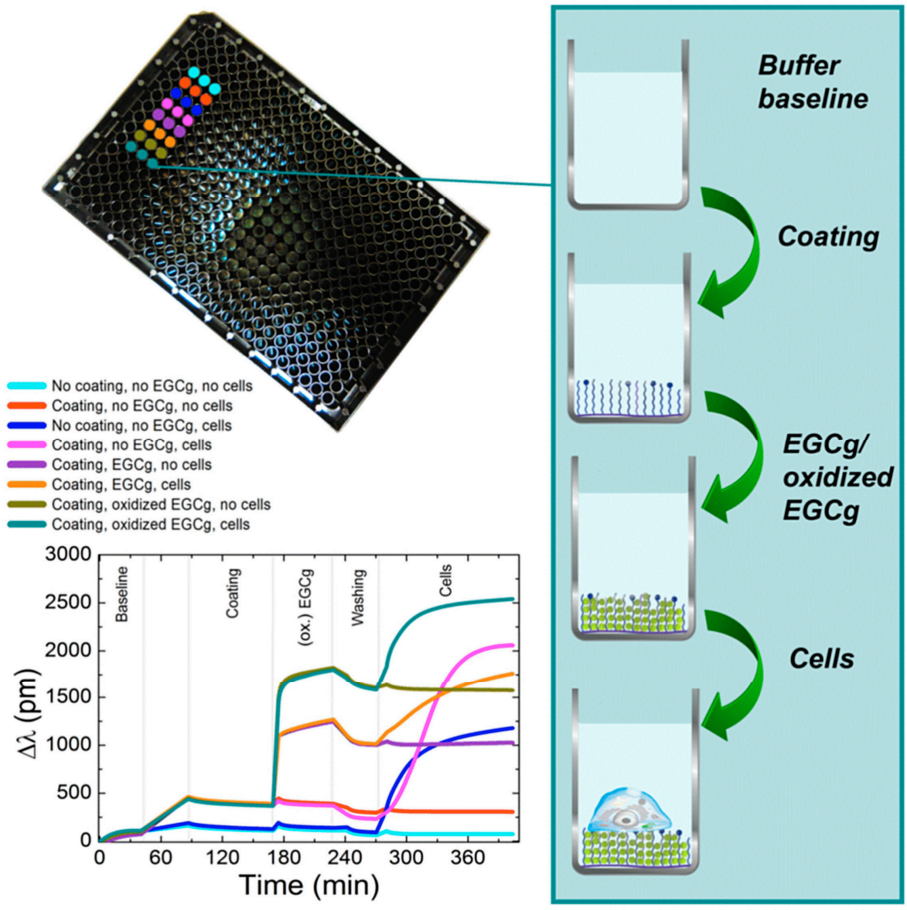

Figure 1 *In situ kinetic curves recorded by the Epic BT instrument. A 384-well plate used in the experiment is also shown, together with the manipulation steps in a typical well (right scheme). Typical experimental curves are plotted (bottom left corner) for PP:PPR coating, and 500 µg/ml EGCg concentration. The detailed experimental conditions corresponding to the various kinetic curves are indicated above the graph [99].*

Label-free optical biosensor for on-line monitoring the integrated response of human B cells upon the engagement of stimulatory and inhibitory immune receptors

(Lendület LP2012-26/2012)

I. Kurucz, B. Péter, A. Prosz, I. Székács, R. Horváth, and A. Erdei (ELTE)

The majority of current cell-based assays relies on the measurement of a single event at a predetermined time point in a specifically chosen signaling path-way, let it be second messenger release, reporter-gene production or target translocation. These measurements require the use of labeled compounds, sometimes the modification of cells to express the target in larger amount or to produce a reporter molecule to be able to monitor receptor engagement. The mentioned manipulations can be toxic for the cells and can interfere with normal cellular physiology of the target receptors or their environment and the applied fluorescence and colored compounds may induce elevated background. Consequently, functional cellular assays which can report from different signaling events in real time without the application of molecular engineering (in providing the suitable cellular partner) and without the use of labelling would be of high value for both theoretical and practical studies even if they are more complex and less specific than cell-based biochemical assays.

To be able to obtain holistic pictures about B cell responses to complex interlocking stimulations Epic BT optical biosensor was applied and set to establishing the method using human B cell lines, derived from Burkitt's lymphomas. We successfully immobilized non-adherent B cells on the surface of the biosensors, without the ligation of any specific receptors or adhesion molecules. This way we were able to demonstrate that engagement of the antigen specific B cell receptors (BCR) induced reproducible dynamic mass redistribution (DMR) inside the cells as a measure of receptor activation (see Fig.1). The initiated DMR response proved to be specific, since only antibodies recognizing the BCR could generate the response; neither the assay-buffer, nor high concentration of indifferent proteins or non-specific antibodies had any effect. The measure of cell activation was sensitive, concentration dependent, and specifically and dose-dependently inhibited by the Syk inhibitor BAY 61-3606. The BCR-triggered DMR response was evoked from three human Epstein-Barr virus (EBV) negative B cell lines, but could not be elicited in two EBV-positive BL cell lines, where the presence of the EBV-derived LMP2A protein desensitizes the cells' response to the BCR-induced signaling.

Therefore, our work opens new avenues to study complex signaling events and to decipher interactions within the signaling network during B cell activation.

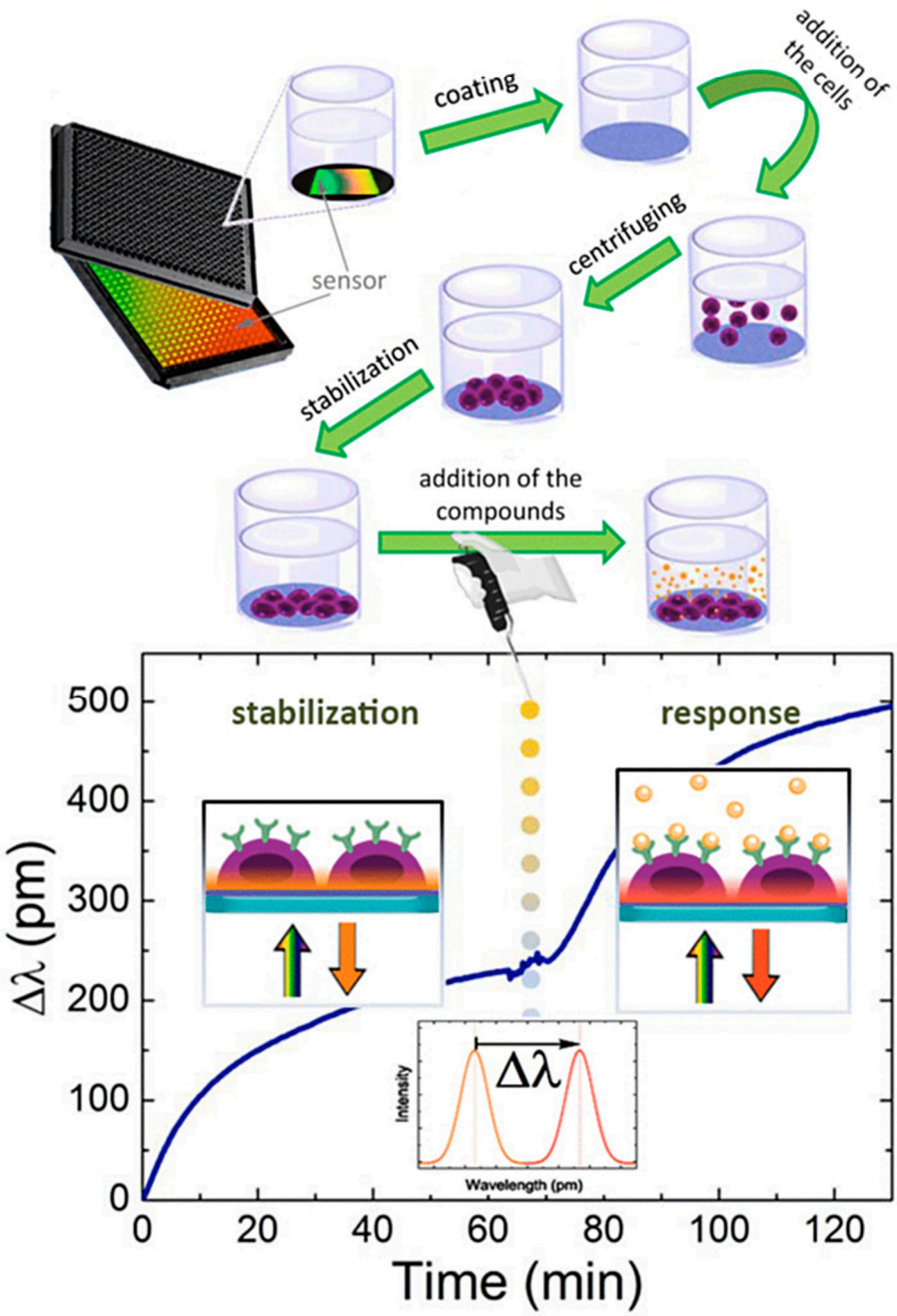

Figure 1 *Experimental setup to perform real-time measurement of dynamic mass redistribution (DMR) using B-cell lines (A); and schematic illustration of the principle of DMR detection (B) [66].*

Fabrication and characterization of ultrathin and spin-coated (thick) dextran layers (Hydrogel film fabrication for biosensing)

(Lendület LP2012-26/2012)

A. Saftics, S. Kurunczi, B. Türk, E. Agócs, B. Kalas, P. Petrik, M. Fried, A. Sulyok, Sz. Bősze (ELTE), and R. Horváth

Fabrication of a stable and reproducible surface with the required chemical functions are one of the major challenge in the development of label-free biosensors. Polysaccharide dextran interface layers are able to improve the sensitivity of biosensors, owing to the anti-fouling property and the high receptor immobilization capacity of the dextran chains.

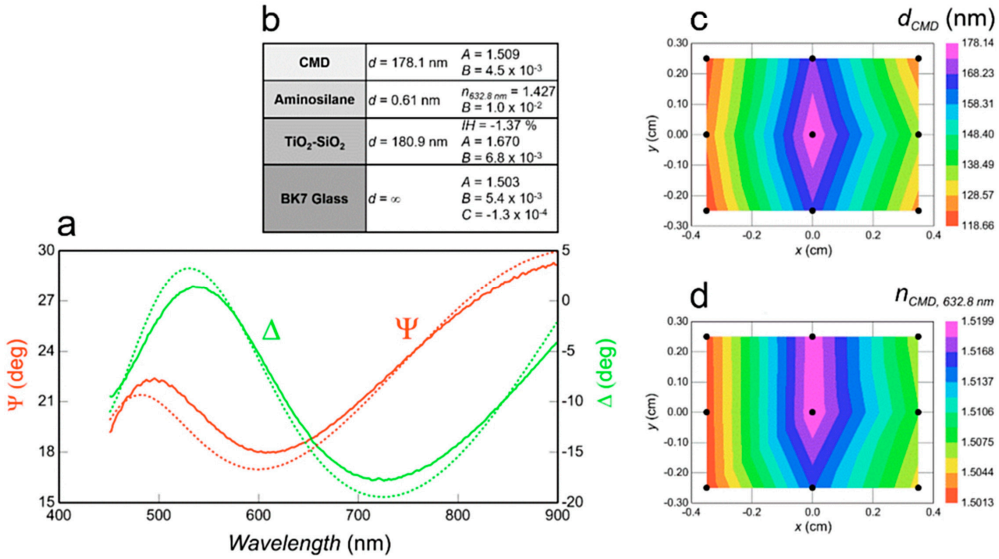

Figure 1 *Ψ (—) and Δ (—) spectra measured for the determination of the thickness and refractive index of CMD on the TiO_2-SiO_2 waveguide (a). The solid lines refer to the measured spectra, the dashed lines (- - - and - - -) to the fitted curves (MSE = 20). The spectra were recorded at the center point (x = 0 cm, y = 0 cm) of the sample fabricated by spin coating of the CMD at 3000 rpm rotational speed. Details about the optical model were also put on the figure (b). Additional figures: thickness (d_{CMD}) (c) and refractive index (n_{CMD}, 632.8 nm) (d) map of the CMD. The refractive index was calculated from the Cauchy equation at the wavelength of 632.8 nm.*

Carboxymethyl-dextran (CMD) was synthetized in our laboratory from the native dextran. Grafting methods based on covalent coupling to aminosilane- and epoxysilane-functionalized surfaces were applied to obtain thin CMD layers. The carboxyl moiety of the CMD was coupled to the aminated surface by EDC (Ethyl-3-(3-dimethylaminopropyl)-carbodiimide hydrochloride) and NHS (N-hydroxy-

succinimide) reagents, while CMD coupling through epoxysilane molecules was performed without any additional reagents. The surface analysis following the grafting procedures consisted of x-ray photoelectron spectroscopy (XPS), attenuated total reflection infrared spectroscopy (ATR-IR), as well as atomic force microscopy (AFM), which proved the presence and the 1 - 2 nm thickness of the CMD layer, and verified its covalent grafting to the surface. The in situ optical waveguide lightmode spectroscopy (OWLS) measurements were suitable to devise the structure of the interfacial dextran layers by the evaluation of the optogeometrical parameters.

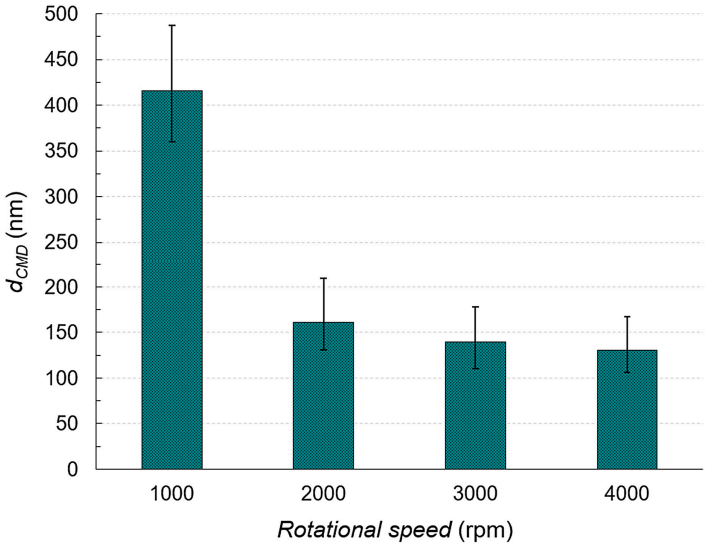

Figure 2 *The effect of the rotational speed on the thickness of the spin coated CMD layer (dCMD). The data were collected from the thickness maps of multiple parallel samples. The map values for the individual samples, as well as these data for each parallel sample were averaged. The bars on the columns represent the minimum and maximum values of the measured thicknesses at the corresponding rotational speeds [116].*

Beside the ultrathin films, we also fabricated thicker CMD layers in the thickness range of around 150 - 400 nm using spin-coating technique. The dependence of the layer thickness on the rotational speed as a technical parameter of the fabrication process, was investigated by spectroscopic ellipsometry. Optical model for the evaluation of the ellipsometric data was developed and the refractive index dispersion (Cauchy B parameter) of the CMD layer was determined based on our high sensitivity measurements on gold substrate. The ellipsometric data showed high rotational speed dependence on the CMD layer thickness comparing the thickness values at 1000 and 2000 rpm. However, varying the rotational speeds to 3000 and 4000 rpm did not cause significant difference in the CMD layer thickness. The mapping measurements also provided details about the extent of the inhomogeneity in the thickness and refractive index of the CMD layers.

Bacteria repellent layer made of flagellin

(Lendület LP2012-26/2012)

B. Kovács, D. Patkó, A. Klein (University of Pannonia), B. Kakasi (University of Pannonia), A. Saftics, S. Kurunczi, F. Vonderviszt (University of Pannonia), and R. Horváth

The development of bacteria repellent surface coatings is critical in various fields ranging from biosensing to health care, biotechnology and food production. In the present study we exploit that the protein flagellin rapidly forms a dense and oriented monolayer on hydrophobic surfaces upon adsorption from aqueous solution. This oriented layer mimics the surface of bacterial flagellar filaments and has excellent E. coli bacteria repellent properties. Quantitative cell adhesion data were obtained by employing fluorescent microscopy and a label-free surface sensitive optical biosensor, OWLS (Optical Waveguide Lightmode Spectroscopy). During the biosensor experiments, injection of the bacterial solution resulted in an almost negligible signal increase on the flagellin covered OWLS chip (Fig. 1). The adhered cells were also visualized by fluorescent microscopy and the formed protein film was characterized by AFM (Atomic Force Microscopy).

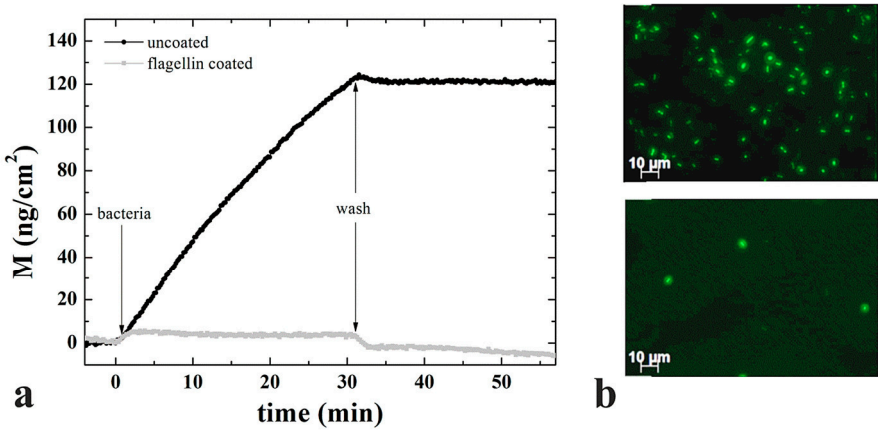

Figure 1 *[a] Calculated surface mass densities from the in situ OWLS measurements on the uncoated (black curve) and flagellin coated (grey curve) surfaces in representative experiments. [b] Representative fluorescent microscopic images of adhered bacteria on the uncoated (upper) and flagellin coated (bottom) surfaces. The images were recorded right after the biosensor measurements. (Reference: B. Kovacs, et al., Sensors Actuators B Chem. 257, 839–845 (2018))*

In parallel control experiments, the adherence of bacteria was measured on bare hydrophobic surfaces as well. The bacteria adhered irreversibly onto the uncoated surface, but reversibly onto the flagellin coated chip. Both OWLS and microscopy results well confirmed that the flagellin coating drastically reduced the adhesion of E. coli cells. Therefore, a novel type of bacteria repellent layer made of flagellin is

demonstrated. The great advantage of the flagellin-based surface coatings is that this protein can be easily produced in large amounts in a cost-effective way. The introduced flagellin-based coatings offer a general toolbox for controlling the surface adhesion of living cells.

Receptor specific adhesion assay for the quantification of integrin–ligand interactions in intact cells using a microplate based, label-free optical biosensor

(Lendület LP2012-26/2012)

I. Székács, N. Orgován, B. Péter, B. Kovács, and R. Horváth

Integrins are transmembrane heterodimers, a group of plasma membrane receptors that mediate adhesion of cells to the extracellular matrix (ECM). Integrins bind to ECM proteins mainly via the Arg-Gly-Asp (RGD) sequence motif and are crucially involved in many physiological events, including immune responses, cell growth and differentiation, and tissue morphogenesis. In addition, integrins are associated with pathophysiological conditions (e.g., thrombosis, some genetic and autoimmune diseases, and metastatic development), and thus, represent important therapeutic target structures. Disruption of binding to integrin receptors is an important topic in drug discovery, comprising the design, synthesis and biomedical applications of new integrin-targeting drugs. In this proof of principle study, we examine the feasibility of using the resonant waveguide grating technology for analysis of integrin–ligand interactions by measuring the kinetics of cell adhesion. As a model, the smallest known natural disintegrin – echistatin from Echis carinatus – was chosen for inhibition of integrin-mediated cell adhesion. By coating the sensor surfaces with an RGD displaying polymer film, and using different concentrations of echistatin to block the cell adhesion molecules in the cell suspensions transferred onto the sensing surfaces, inhibition of binding was determined using a biosensor assay that uses intact cells, does not require ligand labeling, or isolation of receptors.

Figure 1 illustrates schematically the working principle of the introduced label-free cell adhesion assay. First, surface coating of the Corning Epic sensor microplate was created by incubation with 250 µg/ml PLL-g-PEG-RGD for 30 min at room temperature. After washing out the excess of reagent by rinsing the surface with 20 mM HEPES HBSS (pH 7.0), biosensor plate was placed into the Epic instrument and a baseline was recorded for 1 h in 30 µL 20 mM HEPES HBSS (pH 7.0) per each well. After the stable baselines had been established for all wells, detached HeLa cells were mixed with the inhibitor solutions at varying concentrations of the investigated cell adhesion ligand and then 30 µl (containing 8000 cells) of obtained suspensions were seeded into the wells and biosensor responses were recorded for 2 h. The higher inhibitor concentration was applied, the lower the biosensor response was obtained (see the kinetic curves in Fig. 1).

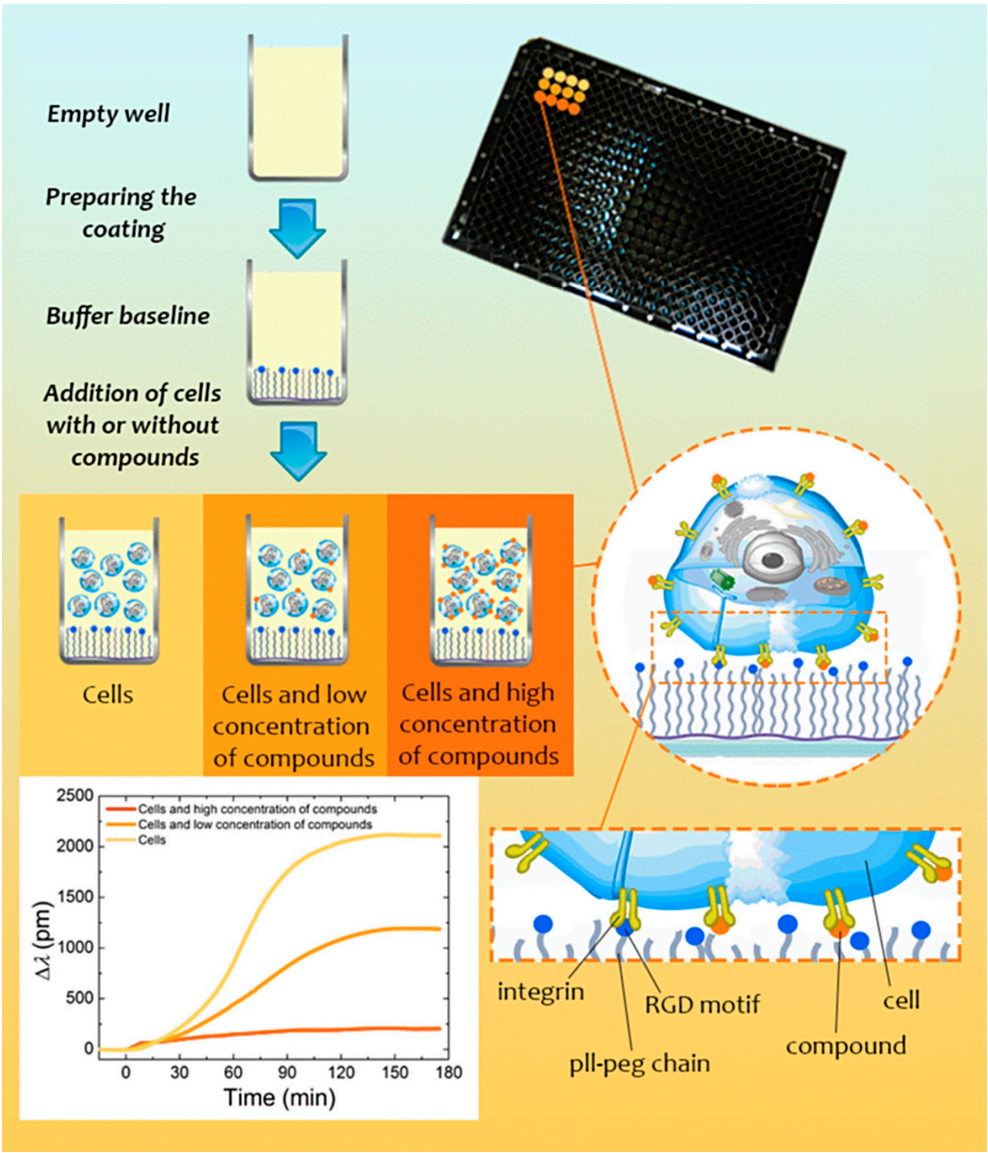

Figure 1 *Schematic illustration of the working principle of the measurement of integrin–ligand interactions by detecting cell adhesion with the Epic BT biosensor. Prior to measurement, the bottom of the biosensor wells is covered with a synthetic polymer layer displaying the integrin ligands. Ligand molecules added to the cell suspensions block integrins on the surface of the adhering cells, therefore weaken the cell adhesion on the ligand displaying sensing surfaces. Representative cell spreading curves for low concentration, high concentration, and without any integrin ligands in the employed cell suspension are shown. (Reference: I. Székács, et al., Sensors Actuators B Chem. 256, 729–734 (2018))*

Using this novel methodology, the half maximal inhibitory concentration (IC_{50}) for echistatin in living cancer cells was determined to be in the range of 20-40 nM, which is in agreement with data in the literature. Although this method detects a combined signal of the number of the adhered cells, it is applicable for rapid, label-free screening of potential pharmaceutical compounds. Moreover, the present methodology uses intact cells so there is no need to isolate or label the integrin receptors involved in binding. In addition, by down-regulating given types of integrins by RNA silencing or by blocking their action with specific antibodies or RGD peptides, the binding assay could be used to study the number of various integrins on the cell surfaces, the integrin-specific affinity of the ligand, as well as processes that are initiated by these integrins. Finally, this methodology has potential application for screening natural, as well as newly developed synthetic molecules that prevent survival mechanisms of tumor cells.

Antibiotic-Induced Release of Small Extracellular Vesicles (Exosomes) with Surface-Associated DNA

(Lendület LP2012-26/2012)

A. Németh (SOTE), N. Orgovan, B. W. Sódar (SOTE), X. Osteikoetxea (SOTE), K. Pálóczi (SOTE), K. É. Szabó-Taylor (SOTE), K. V. Vukman (SOTE), Á. Kittel (MTA KOKI), L. Turiák (MTA TTK), Z. Wiener (SOTE), S. Tóth (SOTE), L. Drahos (MTA TTK), K. Vékey (SOTE), R. Horvath, and E. I. Buzás (SOTE)

Recently, biological roles of extracellular vesicles (which include among others exosomes, microvesicles and apoptotic bodies) have attracted substantial attention in various fields of biomedicine. Here we investigated the impact of sustained exposure of cells to the fluoroquinolone antibiotic ciprofloxacin on the released extracellular vesicles. Ciprofloxacin is widely used in humans against bacterial infections as well as in cell cultures against Mycoplasma contamination. However, ciprofloxacin is an inducer of oxidative stress and mitochondrial dysfunction of mammalian cells. Unexpectedly, here we found that ciprofloxacin induced the release of both DNA (mitochondrial and chromosomal sequences) and DNA-binding proteins on the exofacial surfaces of small extracellular vesicles referred to in this paper as exosomes. Furthermore, a label-free optical biosensor analysis revealed DNA-dependent binding of exosomes to fibronectin (Fig.1). DNA release on the surface of exosomes was not affected any further by cellular activation or apoptosis induction. Our results reveal for the first time that prolonged low-dose ciprofloxacin exposure leads to the release of DNA associated with the external surface of exosomes.

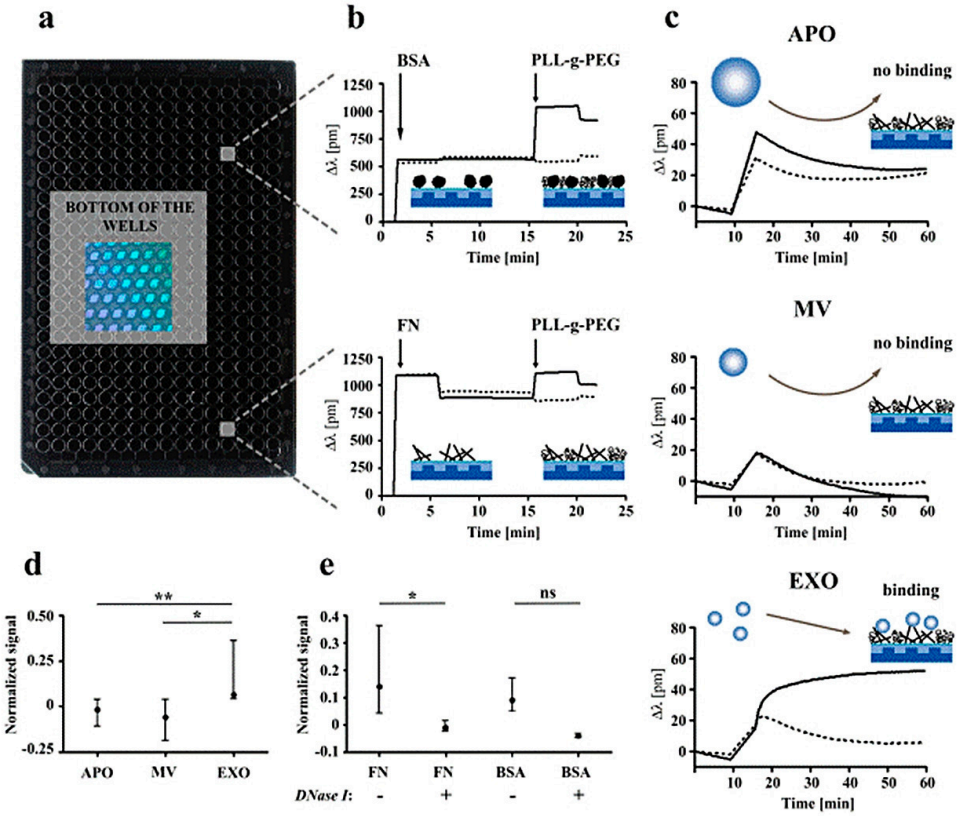

Figure 1 *Label-free optical biosensor analysis of surface adhesion of extracellular vesicles (EVs). (a) Photograph of an Epic microplate (384-well) is shown containing biosensors (b)Microplate wells were coated with bovine serum albumin (BSA) as a control protein or with fibronectin (FN) resulting in a shift in the resonant wavelength (Δλ). Microplate wells were equilibrated with PBS, then BSA or FN were added to the wells (indicated by the first arrows). PLL-g-PEG was used in order to block the non-specific binding sites of wells. After 30 min incubation with PLL-g-PEG, Δλ was recorded for another 5 min (starting points are indicated by the second arrows), and finally PLL-g-PEG was changed to PBS. (c) Adsorption of apoptotic bodies (APOs), microvesicles (MVs) and exosomes (EXOs) onto FN+PLL-g-PEG surfaces (continuous lines) or onto surfaces with adsorbed PLL-g-PEG only (dashed lines). (d) The Δλ values of EV adsorption onto PLL-g-PEG were subtracted from adsorption values onto FN+PLL-g-PEG, and were divided by the Δλ value of EV adsorption onto bare surfaces (as a straightforward normalization with the mass concentrations of various samples) [85].*

Complex Systems Department

Head: György Szabó D.Sc., scientific advisor

Research Staff

- Borsos István
- Juhász Zoltán PhD.
- Ódor Géza D.Sc., scientific advisor
- Szolnoki Attila D.Sc., scientific advisor

Ph.D. students / Diploma workers

- Balázs Király (BME, PhD student)
- Kinga Bodó (BME, MSc student)
- Kristóf Hódsági (BME, BSc-MSc student)
- Gergely Bunth (BME, BSc-MSc student)
- Vince Varga (BME, BSc student)

Researchers at the Complex Systems Laboratory use the methods of statistical physics to investigate evolutionary game theoretic models and dynamic phenomena on various lattices and graphs. These models offer a general mathematical background to multidisciplinary research areas (biology, economics, behavior research, etc.). They extended the analysis of relatedness of folk music and genetics of various ethnical groups in directions that allow the joint investigation of spatial and temporal processes.

In evolutionary game theory they use mathematical models to pursue investigations to explore processes, strategies and relationship systems that develope between selfish individuals, which support cooperation advantageous for the community. Among the punitive strategies they have found variations that efficiently help the prevalence of a behavior representing the common interest in spatial "Tragedy of the commons" games. Model studies also justified the communal usefulness of exchanging information that comes at a cost, if a sufficient number of players willing to sacrifice are present in the community.

In evolutionary game theoretic models depth analysis is based on the ability to decompose interactions described in matrix form into the linear combination of four basic games. Systematic investigation of the coordination components cast light on the existence of social trap situations which are similar to phase-changes known in solid-state physics. At the level of pair interactions, mathematical analysis of the components causing the tragedy of commons clearly indicate that the frequency (and with it the significance) of the separation of individual and collective interests grows with the increase of the number of strategies in the case of potential games, which represent a significant subset of matrix games strongly related to physics.

They studied numerically the size distribution of avalanche-like failures in real-world electric networks with the use of models developed earlier for the synchronization of oscillation in statistical physics. Models suitable to describe the spread of infection were used in modular networks to quantify the effect of the topological features of networks on the speed of very slowly converging processes (Griffith's phase).

They continued to develop self-learning algorithms suitable to identify clusters observable in the space of folk music tunes and hereditary genetic codes characterizing ethnic groups, and to more accurately quantify the measure of relatedness. The continuous expansion of the folk music and genetic databases and their completion by archaeological data may even provide a background for the historical analysis of the migration of peoples.

Effects of Heterogeneity in Power-Grid Network Models

G. Ódor and B. Hartmann

Power-grids are becoming more and more heterogeneous as renewable small (solar, wind, geothermic) suppliers are connected. Therefore, the danger of desynchronization may increase. We have studied the effects of topological and intrinsic (node connection strength) disorder on the second order Kuramoto model with respect to simple homogeneous lattices. Our aim was to provide a description of the desynchronization transition, determine the fluctuations and the heavy tailed failure avalanche distributions, reported in several large blackout events. We have planned to explore possible Griffiths phases and to provide a measure of danger as the function of stochastic elements connected.

We have compared the phase synchronization transition of the second order Kuramoto model, a basic model describing AC electric networks, on 2D lattices and on large synthetic power-grid networks, generated from real data. While admittance matrix of the transmission network is based on a real-life example (the Hungarian power system), matrix of the distribution network is the result of synthetic grid modeling.

Equations of the second order Kuramoto model for the phases Θ_i and the global coupling control parameter K have been analyzed numerically, using 4^{th} order Runge-Kutta differential solvers. Here we introduced quenched heterogeneities, via the A_{ij} intrinsic frequencies of the N nodes, connected via the A_{ij} admittance matrix. For the inertia parameter we used α=1,3 and we also considered the of Gaussian as well as exponentially distributed noise terms. We have measured the global phase synchronization order-parameter and determined the static/dynamic phase transition behavior. We have also determined the distribution of the duration times from fully synchronous (R = 1) to disordered ($R = 1/N^{0.5}$) states, by random sample averaging.

Due to the inertia the transition is of first order type, contrary to the simple Kuramoto model, exhibiting hysteresis at certain global coupling parameter K (see Fig. 1). Heterogeneity cannot round the transition to a critical behavior type, the order parameter fluctuations do not depend on the network size (Fig. 2.). In case of the real power-grid the synchronization is weaker, but breaks down at a smaller K, than in case of lattices. The desynchronization duration distributions exhibit scale-free (heavy) tails below the transition without the assumption of self-organized criticality conjectured for power-grids. The control parameter dependent power-laws (Fig. 3.)

suggest Griffiths phases, but identification of rare-region effects has not been achieved yet [https://arxiv.org/abs/1801.09492].

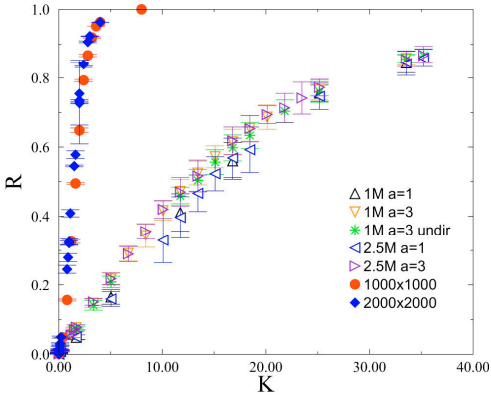

Figure 1 *Comparison of the steady-state order parameter for different networks: 1000x1000, 2000x2000 lattices, powergrids 1,4,5 and US high voltage grid.*

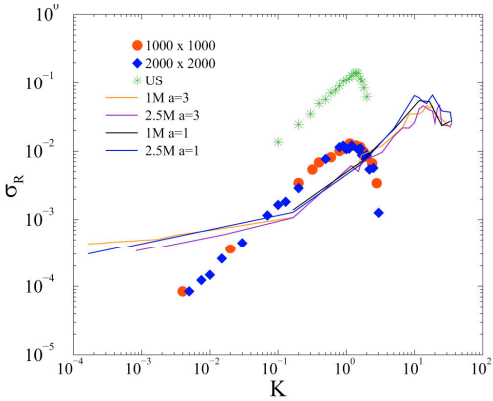

Figure 2 *Fluctuation of the steady-state order parameter for different networks.*

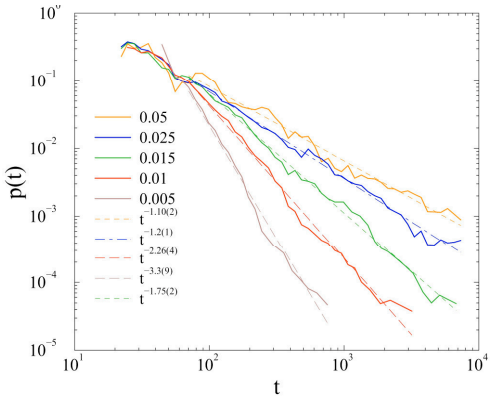

Figure 3 *Avalanche duration distribution for power grid 1 at different control parameters. Dashed lines: power-law fits.*

Second-order freeriding on antisocial punishment restores the effectiveness of prosocial punishment

(OTKA K 120785)

A. Szolnoki, and M. Perc

Economic experiments have shown that punishment can increase public goods game contributions. However, the effectiveness of punishment is challenged by second-order free-riding and antisocial punishment. The latter implies that non-cooperators

punish cooperators, while the former implies unwillingness to shoulder the cost of punishment. While the threat of punishment has the proven ability to deter would-be defectors, the associated costs challenge its evolutionary stability. Antisocial punishment, the deplorable consequence of which is that non-cooperators punish cooperators, is likewise an important impediment to the viability of punishment. But just as prosocial punishment breeds second-order free-riders -- cooperators who refuse to shoulder the cost of punishment -- so does antisocial punishment. Defectors who do not punish cooperators, and are thus second-order free-riding on antisocial punishment, provide the missing link that enables a successful coevolution of cooperation and punishment, even when antisocial punishment is present.

We extend the theory of cooperation in the spatial public goods game by considering four competing strategies, which are traditional cooperators (C) and defectors (D) , as well as cooperators who punish defectors (P_C) and defectors who punish cooperators (P_D). We show that if the synergistic effects are high enough to sustain cooperation based on network reciprocity alone, antisocial punishment does not deter public cooperation. Conversely, if synergistic effects are low and punishment is actively needed to sustain cooperation, antisocial punishment does act detrimental, but only if the cost to fine ratio is low. This behavior is summarized in *Fig. 1*. For relatively large cost cooperation again dominates as a result of spatial pattern formation. Counterintuitively, defectors who do not punish cooperators, and are thus effectively second-order free-riding on antisocial punishment, form an active layer around punishing cooperators, which protects them against defectors that punish cooperators. A representative evolution is illustrated in *Fig. 2*. A stable three-strategy phase that is sustained by an induced cyclic dominance is also possible via the same mechanism. Our results reveal an unlikely evolutionary escape from adverse effects of antisocial punishment, and they provide a rationale for why second-order free-riding is not always an impediment to the evolutionary stability of punishment. All it needs is acknowledging that we live in networks, that is, that interactions among us are not random, but organized [Phys. Rev. X 7, 041027 (2017)].

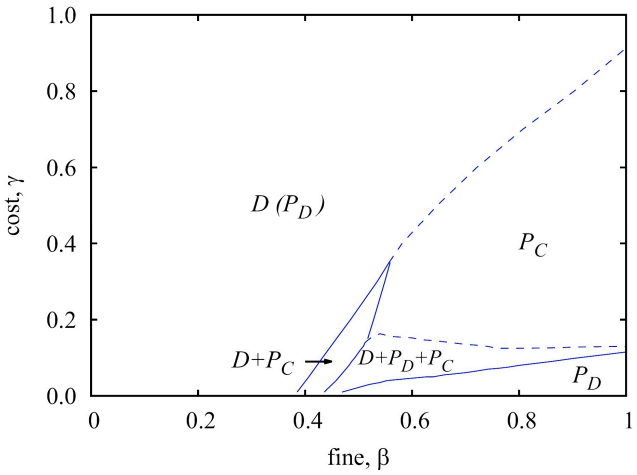

Figure 1 *Full fine - cost phase diagram of the spatial public goods game with prosocial and antisocial punishment, as obtained for r = 3.0. Solid lines denote continuous phase transitions while dashed lines denoted discontinuous phase transitions.*

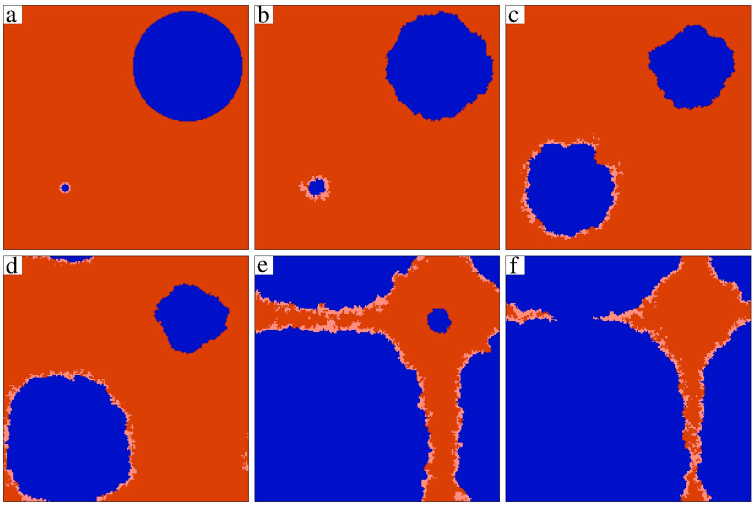

Figure 2 *An illustration of how second-order free-riding on antisocial punishment restores the effectiveness of prosocial punishment. A small domain of PC players (dark blue), surrounded by a thin layer of D players (light red) is inserted into the sea of PD players (dark red) in the bottom left corner of the lattice (a). Similarly, a sizable domain of PC players, but without the protective D layer, is inserted into the sea of PD players in upper right corner of the lattice (a). While the large PC domain without the protective layer shrinks over time, the small PC domain with the protective D layer grows (b-f). The absorbing PC phase is reached after 2000 MCS (not shown).*

Study of the effect of prehistoric Human migration processes to the recent mitochondrial and Y-chromosomal haplogroup distributions using a new correlation-based self-learning algorithm

Z. Juhász and H. Pamjav

We present a new self-learning computational method searching for footprints of early migration processes determining the genetic compositions of recent Human populations. The data being analyzed are 26- and 18-dimensional mitochondrial and Y-chromosomal haplogroup distributions representing 50 recent and 34 ancient populations in Eurasia and America. The algorithms search for associations of haplogroups jointly propagating in a significant subset of these populations. Joint propagations of Hgs are detected directly by similar ranking lists of populations derived from Hg frequencies of the 50 Hg distributions. The method provides us the most characteristic associations of mitochondrial and Y-chromosomal haplogroups, and the set of populations where these associations propagate jointly. In addition, the typical ranking lists characterizing these Hg associations show the geographical

distribution, the probable place of origin and the paths of their protection. Comparison to ancient data verifies that these recent geographical distributions refer to the most important prehistoric migrations supported by archaeological evidences.

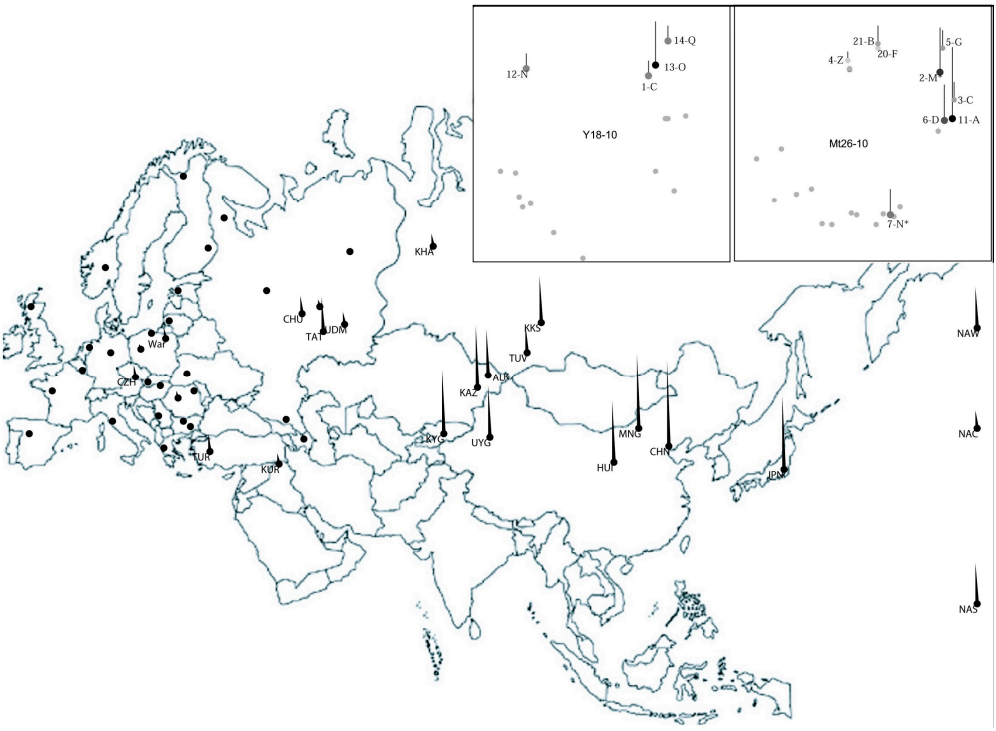

Figure 1 *Geographical distribution of the Hg association shown in the right upper part of the figure (Y: Y-chromosomal, Mt: mitochondrial). The Hg association propagates from East- and Inner Asia (CHI, HUI-Chinese, MON-Mongolian, UYG-Uyghur, KAZ-Kazakh, TUV-Tuvan, KHK-Khakass, KYG-Kyrghyz) to Eastern Europe (CHU-Chuvash,TAT-Tatar,UDM-Udmurt) and to the Native Americans (NAS-South, NAC-Central, NAW-North-Western).*

MFA Publications in 2017

1. **Agócs E**, Kozma P, Nádor J, Hámori A, Janosov M, Kalas B, Kurunczi S, Fodor B, Ehrentreich-Förster E, Fried M, Horváth R, Petrik P: "Grating coupled optical waveguide interferometry combined with in situ spectroscopic ellipsometry to monitor surface processes in aqueous solutions", *Appl Surf Sci 421: pp.289-294. (2017)*
2. **Agócs E**, Zolnai Zs, Rossall AK, van den Berg JA, Fodor B, Lehninger D, Khomenkova L, Ponomaryov S, Gudymenko O, Yukhymchuk V, Kalas B, Heitmann J, Petrik P: "Optical and structural characterization of Ge clusters embedded in ZrO_2", *Appl Surf Sci 421: pp.283-288. (2017)*
3. **Amaral MA**, Perc M, Wardil L, Szolnoki A, da Silva JEJ, da Silva JKL: "Role-separating ordering in social dilemmas controlled by topological frustration", *Phys Rev E-Stat Nonlin 95:(3) Paper 032307. 9 p. (2017)*
4. **Aslam Z**, Lozano JG, Nicholls RJ, Koós AA, Dillon F, Sarahan MC, Nellist PD, Grobert N: "Direct visualization of electrical transport-induced alloy formation and composition changes in filled multi-wall carbon nanotubes by in situ scanning transmission electron microscopy", *J Alloys and Compounds 721: pp.501-505. (2017)*
5. **Babenko V**, Lane G, Koós AA, Murdock AT, So K, Britton J, Meysami SS, Moffat J, Grobert N: "Time dependent decomposition of ammonia borane for the controlled production of 2D hexagonal boron nitride", *Scientific Reports 7:(1) Paper 14297. (2017)*
6. **Balázs R**, Kovács-Kis V, Sipos P, Németh T: "Sorption of lead and copper in hydromorphic soils: Influence of clay and iron mineralogy on metal retention", *In: Galindo AL (Eds.) XVI International Clay Conference - ICC 2017: Scientific Research Abstracts - Volume 7. Granada, Spain, 2017.07.17-2017.07.21. Bari: Digilabs, 2017. p.60. 1 p. (ISBN:978-88-7522-089-1)*
7. **Balázsi Cs**, Fogarassy Zs, Tapasztó O, Kailer A, Schröder C, Parchoviansky M, Galusek D, Dusza J, Balázsi K: "Si_3N_4/graphene nanocomposites for tribological application in aqueous environments prepared by attritor milling and hot pressing", *J Eur Ceramic Soc 37:(12) pp.3797-3804. (2017)*
8. **Balázsi K**, Fogarassy Zs, Schröder C, Kailer A, Balázsi Cs: "Study of Si_3N_4/Graphene for Tribological Applications", In: *Göller G, Gürmen S, Sahin F, Yücel O, Keles Ö, Akin Ö, Yavas B (Eds.) Int Materials Technologies and Metallurgy Conference 2017. Istanbul, Turkey, 2017.10.26-2017.10.27. Istanbul Teknik Üniversitesi, pp.55-58.*
9. **Bali K**, Sáfrán G, Pécz B, Mészáros R: "Preparation of Gold Nanocomposites with Tunable Charge and Hydrophobicity via the Application of Polymer/Surfactant Complexation", *ACS Omega 2:(12) pp.8709-8716. (2017)*
10. **Bálint Zs**, Heath A, Katona G, Kertész K, Sáfián Sz: "Male secondary sexual characters in Aphnaeinae wings (Lepidoptera: Lycaenidae)", *Opuscula Zoologica (Budapest) 48:(1) pp.27-34. (2017)*
11. **Bányász I**, Nagy GUL, Havranek V, Vosecek V, Agócs E, Fried M, Rakovics V, Pelli S: "Recent progress in ion beam fabrication of integrated optical elements", In: *Jaworski M, Marciniak M (Eds.) 19th International Conf on Transparent Optical Networks, ICTON 2017. Girona, Spain, 2017.07.02-2017.07.06. Washington: IEEE Computer Society,*

2017. Paper 8024871. 2 p. (International Conference on Transparent Optical Networks) (ISBN:9781538608586)

12. **Bársony I**: "Szilícium technológia - és amit neki köszönhetünk", Bársony I: Ordinary Member of the HAS, Academic Inaugural Lecture, *2017.01.18 (2017)*
13. **Beke D**, Károlyházy G, Czigány Zs, Bortel G, Kamarás K, Gali A: "Harnessing no-photon exciton generation chemistry to engineer semiconductor nanostructures", *Scientific Reports 7:(1) Paper 10599. 6 p. (2017)*
14. **Bereczk-Tompa E**, Vonderviszt F, Horváth B, Szalai I, Pósfai M: "Biotemplated synthesis of magnetic filaments", *Nanoscale 9:(39) pp.15062-15070. (2017)*
15. **Bíró F**, Dücső C, Radnóczi GyZ, Baji Z, Takács M, Bársony I: "ALD nano-catalyst for micro-calorimetric detection of hydrocarbons", *Sensors and Actuators B-Chemical 247: pp.617-625. (2017)*
16. **Bíró F**, Hajnal Z, Dücső C, Bársony I: "The critical impact of temperature gradients on Pt filament failure", *Microelectron Reliability 78: pp.118-125. (2017)*
17. **Bódis E**, Cora I, Balázsi Cs, Németh P, Zoltán K, Klébert Sz, Fazekas P, Keszler AM, Szépvölgyi J: "Spark plasma sintering of graphene reinforced silicon carbide ceramics", *Ceramics International 43:(12) pp.9005-9011. (2017)*
18. **Braeckman BR**, Misják F, Radnóczi Gy, Caplovicova M, Djemia PH, Tetard F, Belliard L, Depla D: "The nanostructure and mechanical properties of nanocomposite N_{b-x}-CoCrCuFeNi thin films", *Scripta MaterIALIA 139: pp.155-158. (2017)*
19. **Cora I**, Mezzadri F, Boschi F, Bosi M, Caplovicová M, Calestani G, Dódony I, Pécz B, Fornari R: "The real structure of ε-Ga_2O_3 and its relation to κ-phase", *CrystEngComm 19:(11) pp.1509-1516. (2017)*
20. **Csanády Á**, Gábor J, Jenei P, Gubicza J, Szabó PJ, Fábián R, Radnóczi Gy, Tóth AL, Langer G, Krafcsik HO, Verő B: "Secrets of Abraham Ganz's Train Wheels Enlightened by Materials Science Methods", *Materials Science Forum 885: pp.55-60. (2017)*
21. **Daróczi CsS** (mfa) (Eds.): "MTA EK MFA Yearbook 2016", *Budapest: MTA Műszaki Fizikai és Anyagtudományi Kutatóintézet (MFA), 2017. 128 p.*
22. **Deokar G**, Rajput NS, Vancsó P, Ravaux F, Jouiad M, Vignaud D, Cecchet F, Colomer JF: "Large area growth of vertically aligned luminescent MoS_2 nanosheets", *Nanoscale 9:(1) pp.277-287. (2017)*
23. **Dózsa L**, Galkin NG, Pécz B, Osváth Z, Zolnai Zs, Németh A, Galkin KN, Chernev IM, Dotsenko SA: "Mg_2Sn heterostructures on Si(111) substrate", *Appl Surf Sci 405: pp.111-118. (2017)*
24. **El-Tahawy M**, Gubicza J, Huang Y, Choi H, Choe H, Lábár JL, Langdon TG: "The Influence of Plastic Deformation on Lattice Defect Structure and Mechanical Properties of 316L Austenitic Stainless Steel", *Materials Science Forum 885: pp.13-18. (2017)*
25. **El-Tahawy M**, Huang Y, Choi H, Choe H, Lábár JL, Langdon TG, Gubicza J: "High temperature thermal stability of nanocrystalline 316L stainless steel processed by high-pressure torsion", *Mat Sci Eng A Struct 682: pp.323-331. (2017)*
26. **El-Tahawy M**, Huang Y, Um T, Choe H, Lábár JL, Langdon TG, Gubicza J: "Stored energy in ultrafine-grained 316L stainless steel processed by high-pressure torsion", *Journal of Materials Research and Technology 6:(4) pp.339-347. (2017)*

27. **Farkas E**, Srankó D, Kerner Zs, Bartosz S, Zbigniew S, Wieslaw M, Horváth R, Lukasz S, Pap JS: "A Layer-By-Layer technika alkalmazása heterogén katalizátor rétegek építésére vízoxidációra képes, elágazó láncú Cupeptid/polielektrolit párokból", *"Tavaszi Szél" conference, Miskolc, 2017.03.31-04.02., oral presentation (2017)*
28. **Farkas E**, Székács A, Horváth R, Székács I: "Real-time label-free monitoring of cytotoxicity of xenobiotics", *Ph.D. Summer School: Micro- and Nano Sensors, Copenhagen, 2017.14-25., poster and oral presentation (2017)*
29. **Farkas E**, Székács A, Kovács B, Horváth R, Székács I: "Study of the effects of xenobiotics on attached mammalian cell line by label free biosensor", *ICONAN conference, Barcelona, 2017.09.25-27., oral presentation (2017)*
30. **Fekete Z**, Csernai M, Kocsis K, Horváth ÁCs, Pongrácz A, Barthó P: "Simultaneous in vivo recording of local brain temperature and electrophysiological signals with a novel neural probe", *J Neural Engineering 14:(3) Paper 034001. 9 p. (2017)*
31. **Fekete Z**, Pongrácz A: "Multifunctional soft implants to monitor and control neural activity in the central and peripheral nervous system: a review", *Sensors and Actuators B-Chemical 243C: pp.1214-1223. (2017)*
32. **Fodor B**, Defforge T, Agócs E, Fried M, Gautier G, Petrik P: "Spectroscopic ellipsometry of columnar porous Si thin films and Si nanowires", *Appl Surf Sci 421: pp.397-404. (2017)*
33. **Fogarassy Zs**, Petrik P, Duta L, Mihailescu IN, Anastasescu M, Gartner M, Antonova K, Szekeres A: "TEM and AFM studies of aluminium nitride films synthesized by pulsed laser deposition", *Appl Phys A-Mater 123:(12) Paper 756. 12 p. (2017)*
34. **Fornari R**, Pavesi M, Montedoro V, Klimm D, Mezzadri F, Cora I, Pécz B, Boschi F, Parisini A, Baraldi A, Ferrari C, Gombia E, Bosi M: "Thermal stability of ε-Ga_2O3 polymorph", *Acta Materialia 140: pp.411-416. (2017)*
35. **Furkó M**, Balázsi K, Balázsi Csaba: "Amerikai és európai perspektívák a kerámiák és üvegek ipari alkalmazásaira", *Anyagok Világa XIV:(1) pp.1-21. (2017)*
36. **Furkó M**, Fazekas É, Fábián RE, Balázsi Cs: "Electrochemical and Morphological Characterization of Silver Doped Bioceramic Layer on Metallic Implant Materials for Orthophedic Application", *Materials Science Forum 885: pp.7-12. (2017) X. Országos Anyagtudományi Konferencia. Balatonalmádi, Hungary: 2015.10.11-2015.10.13.*
37. **Furkó M**, Havasi V, Kónya Z, Grünewald A, Detsch R, Boccaccini AR, Balázsi Cs: "Development and characterization of multi-element doped hydroxyapatite bioceramic coatings on metallic implants for orthopedic applications", *Boletin De La Sociedad Espanola De Ceramica Y Vidrio, 11 p. (2017)*
38. **Galkin NG**, Galkin KN, Dotsenko SA, Chernov IM, Maslov AM, Dozsa L, Pecz B, Osváth Z, Cora I, Migas DB, Kudrawiec R, Misiewicz J: "$Mg(2)Si_{(x)}Sn_{(1-x)}$ heterostructures on Si(111) substrate for optoelectronics and thermoelectronics", *Proc SPIE - Int Soc Optical Eng 10176: Paper UNSP 1017604. 13 p. (2017)*
39. **Ghegin E**, Rodriguez P, Pasquali M, Sagnes I, Labar JL, Delaye V, Card T, Da Fonseca J, Jany C, Nemouchi F: "CMOS-Compatible Contacts to n-InP", *IEEE T Electron Devices 64:(11) pp.4408-4414. (2017)*
40. **Ghegin E**, Rodriguez Ph, Lábár JL, Menyhárd M, Favier S, Sagnes I, Nemouchi F: "Phase formation sequence in the Ti/InP system during thin film solid-state reactions", *J Appl Phys 121:(24) Paper 245311. 9 p. (2017)*

41. **Giannazzo F**, Fisichella G, Greco G, La Magna A, Roccaforte F, Pécz B, Yakimova R, Dagher R, Michon A, Cordier Y: "Graphene integration with nitride semiconductors for high power and high frequency electronics", *Phys Status Solidi A-Applications Materials Science 214:(4) Paper 1600460. (2017)*

42. **Greco G**, Giannazzo F, Fiorenza P, Di Franco S, Alberti A, Iucolano F, Cora I, Pécz B, Roccaforte F: "Barrier Inhomogeneity of Ni Schottky Contacts to Bulk GaN", *Phys Status Solidi A-Applications Materials Science 2017: Paper 1700613. 6 p. (2017)*

43. **Gyulai J**, Battistig G, Kiss ÁZ, Szilágyi E: "Georges Amsel (Amsel György) 1933–2017", *Fizikai Szemle 67:(4) pp.110-114. (2017)*

44. **Gyulai J**: "FROM Ion Beam Techniques To Nanostructures", *Academia Europaea Section Initiated Workshop - Inagural Lectures by New Members of Physics and Engineering Sciences, Academia Europaea Inaugural Session, Budapest, 2017.09.03, oral presentation (2017)*

45. **Hagymási I**, Vancsó P, Pálinkás A, Osváth Z: "Interaction effects in a chaotic graphene quantum billiard", *Phys Rev B 95:(7) Paper 075123. 8 p. (2017)*

46. **Heczel A**, Kawasaki M, Lábár JL, Jang Jae-il, Langdon TG, Gubicza J: "Defect structure and hardness in nanocrystalline CoCrFeMnNi High-Entropy Alloy processed by High-Pressure Torsion", *J Alloys and Compounds 711: pp.143-154. (2017)*

47. **Hoang Luong N**, Thanh Trung T, Phuong Loan T, Hoang Nam N, Jenei P, Lábár JL, Gubicza J: "Structure and Magnetic Properties of Nanocrystalline $Fe_{55}Pd_{45}$ Processed by Sonoelectrodeposition", *J Electronic Materials 46:(6) pp.3720-3725. (2017)*

48. **Holczer E**, Fürjes P: "Effects of embedded surfactants on the surface properties of PDMS; applicability for autonomous microfluidic systems", *Microfluidics and Nanofluidics 21:(5) Paper 81. 14 p. (2017)*

49. **Holczer E**, Hakkel O, Fürjes P: "Fabrication of Hybrid Microfluidic System on Transparent Substrates for Electrochemical Applications", In: *Jean-Paul Viricelle, Christophe Pijolat, Mathilde Rieu (Eds.) Eurosensors 2017, Paris, France, 2017.09.03-2017.09.06. MDPI AG, Paper 326. 4 p.14*

50. **J Kelling**, Ódor Gé, S Gemming: "Local Scale-Invariance of the 2+1 dimensional Kardar-Parisi-Zhang model", *J Physics A-Mathematical and Theoretical 50:(12) Paper 12LT01. 9 p. (2017)*

51. **Justh N**, Firkala T, László K, Lábár JL, Szilágyi IM: "Photocatalytic C60-amorphous TiO_2 composites prepared by atomic layer deposition", *Appl Surf Sci 419: pp.497-502. (2017)*

52. **Kalas B**, Nádor J, Agócs E, Saftics A, Kurunczi S, Fried M, Petrik P: "Protein adsorption monitored by plasmon-enhanced semi-cylindrical Kretschmann ellipsometry", *Appl Surf Sci 421: pp.585-592. (2017)*

53. **Kalas B**, Pollakowski B, Nutsch A, Streeck C, Nádor J, Fried M, Beckhoff B, Petrik P: "Ellipsometric and X-Ray Spectrometric Investigation of Fibrinogen Protein Layers", *Phys Status Solidi C-Curr T Solid State Phys 14:(12) Paper 1700210. (2017)*

54. **Károlyi J**, Németh M, Evangelisti C, Sáfrán G, Schay Z, Horváth A, Somodi F: "Carbon dioxide reforming of methane over Ni–In/SiO_2 catalyst without coke formation", *J Ind Eng Chemistry X: p. AiP. (2017)*

55. **Kelling J**, Ódor Gé, Gemming S: "Suppressing correlations in massively parallel simulations of lattice models", *Computer Physics Communications 220: pp. 205-211. (2017)*

56. **Kertész K**, Piszter G, Horváth ZE, Bálint Zs, Biró LP: "Changes in structural and pigmentary colours in response to cold stress in Polyommatus icarus butterflies", *Scientific Reports 7:(1) Paper 1118. 12 p. (2017)*

57. **Király B**, Szabó Gy: "Evolutionary games combining two or three pair coordinations on a square lattice", *Phys Rev E-Stat Nonlin: Covering Statistical Nonlinear Biological And Soft Matter Physics 96: Paper 042101. 7 p. (2017)*

58. **Király B**, Szabó Gy: "Evolutionary games with coordination and self-dependent interactions", *Phys Rev E-Stat Nonlin 95:(1) Paper 012303. 7 p. (2017)*

59. **Kotsilkova R**, Ivanov E, Todorov P, Petrova I, Volynets N, Paddubskaya A, Kuzhir P, Uglov V, Biró I, Kertész K, Márk GI, Biró LP: "Mechanical and electromagnetic properties of 3D printed hot pressed nanocarbon/poly(lactic) acid thin films", *J Appl Phys 121:(6) Paper 064105. 8 p. (2017)*

60. **Kovács B**, Székács I, Kakasi B, Kurunczi S, Vonderviszt F, Horváth R: "Élő sejtek adhéziójának nyomon követése jelölésmentes optikai bioszenzorokkal genetikailag módosított flagellinrétegeken", In: *MKE (Eds.) MKE Meeting 2017: MKE Electronics and Sensorics Group, Budapest, Hungary, 2017.11.10 Budapest: Magyar Kémikusok Egyesülete (MKE), 2017. p. 12. ("MKE előadói ülés 2017, Az MKE Elektroanalitikai és Szenzorikai szakcsoport szervezésében") (ISBN:978-963-9970-84-7)*

61. **Kovács B**, Székács I, Kakasi B, Kurunczi S, Vonderviszt F, Horváth R: "Genetikailag módosított flagellinrétegeken élő sejtek adhéziójának nyomon követése jelölésmentes optikai bioszenzorokkal", *A Magyar Biofizikai Társaság XXVI. Kongresszusa, Szeged, 2017-08-22-25, oral presentation (2017)*

62. **Kovács B**, Székács I, Kurunczi S, Kakasi B, Vonderviszt F, Horváth R: "Biomimetic coatings from genetically engineered flagellin variants to control cell adhesion", *Biological Surfaces and Interfaces: Interface Dynamics, Spain, Sant Feliu de Guixols, July 2-7 (2017)*

63. **Kovács TN**, Pokol G, Gáber F, Nagy D, Igricz T, Lukács IE, Fogarassy Zs, Balázsi K, Szilágyi IM: "Preparation of iron tungstate ($FeWO_4$) nanosheets by hydrothermal method", *Materials Research Bulletin 95: pp.563-569. (2017)*

64. **Kovács Zs**, Ezzeldien M, Chinh Nguyen Q, Radnóczi György, Lendvai J: "Nanoindentation measurements on a torsionally deformed $Zr_{44}Ti_{11}Cu_{10}Ni_{10}Be_{25}$ bulk metallic glass", *J Alloys and Compounds 708: pp.301-307. (2017)*

65. **Kovács-Kis V**, Czigány Zs, Németh T: "Nanostructural investigation of slightly altered rhyolitic volcanic glass", *Materials Characterization 127: pp.121-128. (2017)*

66. **Kurucz I**, Péter B, Prosz A, Szekács I, Horváth R, Erdei A: "Label-free optical biosensor for on-line monitoring the integrated response of human B cells upon the engagement of stimulatory and inhibitory immune receptors", *Sensors and Actuators B-Chemical 240: pp.528-535. (2017)*

67. **Lábár JL**, Das Partha P: "Pattern Center and Distortion Determined from Faint, Diffuse Electron Diffraction Rings from Amorphous Materials", *Microscopy and Microanalysis 23:(3) p.647-660. (2017)*

68. **Liu L**, Chen X, Szolnoki A: "Competitions between prosocial exclusions and punishments in finite populations", *Scientific Reports 7: Paper 46634. 8 p. (2017)*

69. **Lohner T**, Serényi M, Szilágyi E, Zolnai Zs, Czigány Zs, Khánh NQ, Petrik P, Fried M: "Spectroellipsometric detection of silicon substrate damage caused by radiofrequency sputtering of niobium oxide", *Appl Surf Sci 421: pp.636-642. (2017)*

70. **Makra I**, Brajnovits A, Jágerszki Gy, Fürjes P, Gyurcsányi RE: "Potentiometric sensing of nucleic acids using chemically modified nanopores", *Nanoscale 9:(2) pp.739-747. (2017)*

71. **Mark GI**, Fejer GR, Vancsó P, Lambin P, Biró LP: "Electronic Dynamics in Graphene and MoS2 Systems", *Phys Status Solidi B-Basic Research 254:(11) Paper 1700179. (2017)*

72. **McColl J**, Horváth R, Yakubov GE, Ramsden JJ: "Surface rearrangement of adsorbed EGCG–mucin complexes on hydrophilic surfaces", *Int J Biol Macromolecules 95: pp.704-712. (2017)*

73. **Mónika F**, Balázsi K, Balázsi Cs: "Comparative Study on Preparation and Characterization of Bioactive Coatings for Biomedical Applications-A Review on Recent Patents and Literature", *Reviews on Advanced Mater Sci 48:(1) pp.25-51. (2017)*

74. **Morgenstern M**, Freitag N, Nent A, Nemes-Incze P, Liebmann M: "Graphene Quantum Dots Probed by Scanning Tunneling Microscopy", *Annalen Der Physik 529:(11) Paper 1700018. 9 p. (2017)*

75. **Murdock AT**, van Engers CD, Britton J, Babenko V, Meysami SS, Bishop H, Crossley A, Koós AA, Grobert N: "Targeted removal of copper foil surface impurities for improved synthesis of CVD graphene", *Carbon 122: pp.207-216. (2017)*

76. **Nádas J**, Rakovics V, Réti I, Dücső Cs, Battistig G: "Spatially and spectrally stable semiconductor light sources for near infrared spectroscopy", *Materials Today - Proc 4:(7) pp.7107-7113. (2017), NanoFIS 2016. Graz, Austria: 2016.06.27-2016.06.29.*

77. **Nádas J**, Rakovics V, Réti I: "Bandwidth widening in NIR LEDs and opportunities in visible range", In: *Matej B Kobav (Eds.), Proc Lux Europa 2017. Ljubljana, Slovenia, 2017.09.18-2017.09.20. Ljubljana: Lighting Engineering Society of Slovenia, 2017. pp.669-674. (ISBN:978-961-93733-4-7)*

78. **Nádas J**, Rakovics V: "Fehér LED a közeli infravörös tartományban", *Fizikai Szemle 67:(1) pp.2-6. (2017)*

79. **Nádas J**, Rakovics V: "High Intensity Broad Spectrum LEDs in the Near Infrared Range", *Materials Science Forum 885: pp.141-146. (2017)*

80. **Nádor J**, Kalas B, Saftics A, Illés L, Moldovan C, Gartner M, Fried M, Vonderviszt F, Petrik P: "Bevonatok létrehozása genetikailag módosított bakteriális filamentumokból vízszennyező anyagok detektálására alkalmas érzékelőfelületekhez", *A Magyar Biofizikai Társaság XXVI. Kongresszusa, Szeged, 2017-09-22-25, poster presentation (2017)*

81. **Nádor J**, Saftics A, Kalas B, Illés L, Kovács B, Moldovan C, Romanenko A, Gartner Mariuca, Fried M, Vonderviszt F, Petrik P: "Fabrication of genetically modified bacterial filament coatings to develop sensor surfaces for detecting water pollution", *5th Conference on Sustainable Energy Brasov, 19-21. October 2017, oral presentation. (2017)*

82. **Nádor J**, Saftics A, Kalas B, Illés L, Moldovan C, Gartner M, Kovács B, Kurunczi S, Fried M, Tóth É, Vonderviszt F, Petrik P: "Sensor surface preparation using genetically

modified bacterial filaments", *E-MRS Fall Meeting, Warsaw, Poland, 18-21 September 2017, poster presentation. (2017)*

83. **Nagy HK**, Misják F: "Integrált áramköri alkalmazásra szánt Cu-Mn vékonyrétegek mikroszerkezete és mechanikai tulajdonságai", *BKL Kohászat 2017:(6) pp.44-47. (2017)*
84. **Nemes-Incze P**, Kukucska G, Koltai J, Kurti J, Hwang C, Tapasztó L, Biró LP: "Preparing local strain patterns in graphene by atomic force microscope based indentation", *Scientific Reports 7: Paper 3035. 7 p. (2017)*
85. **Németh A**, Orgován N, Sódar WB, Osteikoetxea X, Pálóczi K, Szabó-Taylor KÉ, Vukman KV, Kittel Á, Turiák L, Wiener Z, Tóth S, Drahos L, Vékey K Horváth R, Buzás EI: "Antibiotic-induced release of small extracellular vesicles (exosomes) with surface-associated DNA", *Scientific Reports 7: Paper 8202. 16 p. (2017)*
86. **Németh M**, Srankó D, Károlyi J, Somodi F, Schay Z, Sáfrán G, Sajó I, Horváth A: "Na-promoted Ni/ZrO_2 dry reforming catalyst with high efficiency: details of Na_2O-ZrO_2-Ni interaction controlling activity and coke formation", *Catalysis Sci Techn 7: p. AiP. (2017)*
87. **Németh T**, Kovács-Kis V, Sipos P, Dódony I: "Modeling water - swelling clay mineral interactions in soils and their effects on sorption characteristics", In: *Galindo AL (Eds.) XVI International Clay Conference - ICC 2017: Scientific Research Abstracts - Volume 7. Granada, Spain, 2017.07.17-2017.07.21. Bari: Digilabs, 2017. p.575. 1 p. (ISBN:978-88-7522-089-1)*
88. **Neparáczki E**, Juhász Z, Pamjav H, Fehér T, Csányi B, Zink A, Maixner F, Pálfi G, Molnár E, Pap I, Kustár Á, Révész L, Raskó I, Török T: "Genetic structure of the early Hungarian conquerors inferred from mtDNA haplotypes and Y-chromosome haplogroups in a small cemetery", *Molecular Genetics and Genomics 292:(1) pp.201-214. (2017)*
89. **Ódor Gé**: "Kritikus dinamika egy nagy emberi konnektomon", *Fizikai Szemle 67:(7-8) pp.227-231. (2017)*
90. **Oláh N**, Furkó M, May Z, Sulyok A, Balázsi K: "Mechanical characterization and corrosion behavior of protective TiC/amorphous c nanocomposite coating as surface thin film", *Resolution and Discovery 2:(1) Paper 43. 10 p. (2017)*
91. **Ormándi Sz**, Cora I, Dallos Zs, Kristály F, Dódony I: "Structural study of mordenite from Mátra Mts. (N-Hungary): dachiardite moduls reduce channel size in Mordenite", *Resolution and Discovery 2:(1) Paper 45. 4 p. (2017)*
92. **Pálinkás A**, Molnár Gy, Magda GZs, Hwang C, Tapasztó L, Samuely P, Szabó P, Osváth Z: "Novel graphene/Sn and graphene/SnO_x hybrid nanostructures: Induced superconductivity and band gaps revealed by scanning probe measurements", *Carbon 124: pp.611-617. (2017)*
93. **Papp K**, Holczer E, Kecse-Nagy C, Szittner Z, Lóránd V, Rovero P, Prechl J, Fürjes P: "Multiplex determination of antigen specific antibodies with cell binding capability in a self-driven microfluidic system", *Sensors and Actuators B-Chemical 238: pp.1092-1097. (2017)*
94. **Papp M**, Szabó P, Srankó D, Sáfrán G, Kollar L, Skoda-Foldes R: "Mono- and double carbonylation of aryl iodides with amine nucleophiles in the presence of recyclable palladium catalysts immobilised on a supported dicationic ionic liquid phase", *RSC Advances 7:(70) pp.44587-44597. (2017)*

95. **Park DG**, Kishore MB, Lee DH, Kim JY, Jacobs LJ, Vértesy G, Son D: "A study of microstructural analysis for nondestructive evaluation of thermal annealing using magnetic properties", *NDT E International 89: pp.14-18. (2017)*

96. **Pászti Z**, Hakkel O, Szíjjártó GP, Tompos A: "Adsorption and transformations of ethanol over ceria based model catalysts", *Catalysis Today, in press: 9 p. (2017)*

97. **Perc M**, Jordan JJ, Rand DG, Wang Z, Boccaletti S, Szolnoki A: "Statistical physics of human cooperation", *Physics Reports-Review Section of Physics Letters 687: pp.1-51. (2017)*

98. **Péter B**, Bosze S, Horváth R: "Biophysical characteristics of proteins and living cells exposed to the green tea polyphenol epigallocatechin-3-gallate (EGCg): review of recent advances from molecular mechanisms to nanomedicine and clinical trials", *European Biophysics Journal 46:(1) pp.1-24. (2017)*

99. **Péter B**, Farkas E, Forgács E, Saftics A, Kovács B, Kurunczi S, Székács I, Csampai A, Bosze Sz, Horváth R: "Green tea polyphenol tailors cell adhesivity of RGD displaying surfaces: multicomponent models monitored optically", *Scientific Reports 7: Paper 42220. 16 p. (2017)*

100. **Péter B**, Farkas E, Forgács E, Saftics A, Kovács B, Kurunczi S, Székács I, Csámpai A, Bősze Sz, Horváth R: "Zöld tea polifenol (EGCg) és a sejtadhéziós mátrix kölcsönhatásainak vizsgálata jelölésmentes optikai bioszenzorokkal", In: *MKE (Eds.) MKE előadói ülés 2017: Az MKE Elektroanalitikai és Szenzorikai szakcsoport szervezésében. Budapest, Hungary, 2017.11.10 Budapest: Magyar Kémikusok Egyesülete (MKE), 2017. p. 11. ("MKE előadói ülés 2017, Az MKE Elektroanalitikai és Szenzorikai szakcsoport szervezésében") (ISBN:978-963-9970-84-7)*

101. **Péter B**, Farkas E, Forgács E, Saftics A, Kovács B, Kurunczi S, Székács I, Csámpai A, Bősze Sz, Horváth R: "Zöld tea polifenol (EGCg) és a sejtadhéziós mátrix kölcsönhatásainak vizsgálata jelölésmentes optikai bioszenzorokkal", In: *Zimányi L (Eds.) A Magyar Biofizikai Társaság XXVI. Kongresszusa. Szeged, Hungary, 2017.08.22-2017.08.25. Szeged: Magyar Biofizikai Társaság, 2017. p. 47. (ISBN:978-963-12-9447-7)*

102. **Petrik P**, Agócs E, Kalas B, Fodor B, Lohner T, Nádor J, Saftics A, Kurunczi S, Novotny T, Perez-Feró E, Nagy R, Hamori A, Horváth R, Hózer Z, Fried M: "Nanophotonics of biomaterials and inorganic nanostructures", *J Physics Conference Series 794:(1) Paper 012004. 10 p. (2017)*

103. **Petrik P**, Sulyok A, Novotny T, Perez-Feró E, Kalas B, Agócs E, Lohner T, Lehninger D, Khomenkova L, Nagy R, Heitmann J, Menyhárd M, Hózer Z: "Optical properties of Zr and ZrO_2", *Appl Surf Sci 421: pp.744-747. (2017)*

104. **Pósa L**, El Abbassi M, Makk P, Sánta B, Nef C, Csontos M, Calame M, Halbritter A: "Multiple Physical Time Scales and Dead Time Rule in Few-Nanometers Sized Graphene–SiO_x-Graphene Memristors", *Nano Letters 17:(11) pp.6783-6789. (2017)*

105. **Pothorszky Sz**, Zámbó D, Szekrényes D, Hajnal Z, Deák A: "Detecting patchy nanoparticle assembly at the single-particle level", *Nanoscale 9:(29) pp.10344-10349. (2017)*

106. **Rachid Ben Zine H**, Cinar Sahin F, Horváth ZE, Czigány Zs, Horváth Á, Balázsi K, Balázsi Cs: "Effect of Si_3N_4 addition on the morphological and structural properties of the

316L stainless steel for nuclear applications", *Resolution and Discovery 2:(1) 55, pp.23-30. (2017)*

107. **Rachid Ben Zine H**, Horváth A, Balázsi K, Balázsi Cs: "Submicron Sized Sintered Ods Steels Prepared by High Efficient Attrition Milling and Spark Plasma Sintering", *Courrier du Savoir 24: pp.93-100. (2017)*
108. **Rácz AS**, Kerner Z, Németh Á, Panjan P, Peter L, Sulyok A, Vértesy G, Zolnai Zs, Menyhárd M: "Corrosion Resistance of Nanosized Silicon Carbide-Rich Composite Coatings Produced by Noble Gas Ion Mixing", *ACS Appl Materials Interfaces 9:(51) pp.44892-44899. (2017)*
109. **Rácz AS**: "Szilícium-Karbidban Gazdag Nano-Védőréteg Előállítása Nemesgázokkal Történő Ionkeveréssel", In: *Keresztes G (Eds.) Tavaszi Szél = Spring Wind 2017 [tanulmánykötet] 2. . 570 p. Miskolc, Hungary, 2017.03.31-2017.04.02. Budapest: Doktoranduszok Országos Szövetsége, 2017. pp.120-129., 1-3. kötet közös ISBN-je:978-615-5586-18-7 Irodalomtudomány Kémia- és környezettudomány Kommunikáció- és médiatudomány Közgazdaságtudomány Közigazgatás-tudomány Matematika- és informatikai tudomány*
110. **Radnóczi Gy**, Bokányi E, Erdélyi Z, Misják F: "Size dependent spinodal decomposition in Cu-Ag nanoparticles", *Acta Materialia 123: pp.82-89. (2017)*
111. **Radnóczi GyZ**, Knez D, Hofer F, Frangis N, Vouroutzis N, Stoemenos J, Pécz B: "Inclusions in Si whiskers grown by Ni metal induced lateral crystallization", *J Appl Phys 121:(14) Paper 145301. 7 p. (2017)*
112. **Radó J**, Battistig G, Pap AE, Fürjes P, Földesy P: "Thermal Noise Limited, Scalable Multi-Piezoresistor Readout Architecture", In: *Jean-Paul Viricelle, Christophe Pijolat, Mathilde Rieu (Eds.) Eurosensors 2017. Paris, France, 2017.09.03-2017.09.06. MDPI AG, Paper 598. 4 p.14*
113. **Radó J**, Dücső Cs, Földesy P, Szebényi G, Nawrat Z, Rohr K, Fürjes P: "3D force sensors for laparoscopic surgery tool", *Microsystem Technologies in press: p. in press. 7 p. (2017)*
114. **Rakovics V**, Nádas J, Réti I, Dücső Cs, Battistig G: "Growth and characterization of broad spectrum infrared emitting GaInAsP/InP heterostructures", *J Crystal Growth 468: pp.572-575. (2017)*
115. **Rigó I**, Veres M, Fürjes P: "SERS Active Periodic 3D Structure for Trapping and High Sensitive Molecular Analysis of Particles or Cells", In: *Jean-Paul Viricelle, Christophe Pijolat, Mathilde Rieu (Eds.) Eurosensors 2017. Paris, France, 2017.09.03-2017.09.06. MDPI AG, Paper 560. 4 p.14*
116. **Saftics A**, Kurunczi S, Türk B, Agócs E, Kalas B, Petrik P, Fried M, Sulyok A, Bősze Sz, Horváth R: "Spin Coated Carboxymethyl Dextran Layers On TiO_2-SiO_2 Optical Waveguide Surfaces", *Revue Roumaine De Chimie 62:(10) pp. 775-781. (2017)*
117. **Saftics A**, Kurunczi S, Türk B, Horváth R: "Development of dextran interface layer for label-free biosensing", *oral presentation, European Advanced Materials Congress, Stockholm (2017)*
118. **Saftics A**, Nádor J, Kalas B, Türk B, Vonderviszt F, Kurunczi S, Horváth R, Petrik P, Fried M: "Ellipsometric characterization of carbohydrate and protein layers for biosensor applications", *oral presentation, Conference for Sustainable Energy, Brasov (2017)*

119. **Saftics A**, Türk Barbara, Sztilkovics M, Székács I, Kurunczi S, Horváth R: "Dextrán alapú felületi rétegek fejlesztése bioszenzorikai alkalmazásokhoz", In: *MKE (Eds.) MKE előadói ülés 2017: Az MKE Elektroanalitikai és Szenzorikai szakcsoport szervezésében. Budapest, Hungary, 2017.11.10 Magyar Kémikusok Egyesülete (MKE), 2017. p. 8. ("MKE előadói ülés 2017, Az MKE Elektroanalitikai és Szenzorikai szakcsoport szervezésében") (ISBN:978-963-9970-84-7)*

120. **Sautner E**, Papp K, Holczer E, Tóth EL, Ungai-Salánki R, Szabó B, Fürjes P, Prechl J: "Detection of red blood cell surface antigens by probe-triggered cell collision and flow retardation in an autonomous microfluidic system", *Scientific Reports 7:(1) Paper 1008. 9 p. (2017)*

121. **Serényi M**, Frigeri C, Csik A, Khanh NQ, Németh Á, Zolnai Zs: "On the mechanisms of hydrogen-induced blistering in RF-sputtered amorphous Ge", *CrystEngComm 19:(11) pp.1486-1494. (2017)*

122. **Sipos P**, Balázs R, Kovács-Kis V, Németh T: "Comparison of single element and competitive sorption of heavy metals on soil clay and iron-oxyhydroxide particles in soils", In: *Galindo AL (Eds.) XVI International Clay Conference - ICC 2017: Scientific Research Abstracts - Volume 7. Granada, Spain, 2017.07.17-2017.07.21. Bari: Digilabs, 2017. p. 708. 1 p. (ISBN:978-88-7522-089-1)*

123. **Sipos P**, Kovács-Kis V, Balázs R, Németh T: "Role of smectites and smectite-iron oxide associations in metal sorption by soils", *Geophysical Research Abstracts 19: Paper EGU2017-7351. (2017)*

124. **Szabó Gy**, Bodó KS, Samani KA: "Separation of cyclic and starlike hierarchical dominance in evolutionary matrix games", *Phys Rev E-Stat Nonlin 95:(1) Paper 012320. 7 p. (2017)*

125. **Székács I,** Farkas E, Székács A, Horváth R: "A label-free high-throughput optical biosensor for cytotoxicity studies", *Spain, Sant Feliu de Guíxols, 2017-07-02-2017-07-07 poster presentation (2017)*

126. **Székács I**, Farkas E, Székács A, Horváth R: "Nagy áteresztő képességű optikai bioszenzor sejttoxicitás jelölésmentes vizsgálataihoz", In: *Zimányi László (Eds.) A Magyar Biofizikai Társaság XXVI. Kongresszusa. Szeged, Hungary, 2017.08.22-2017.08.25. Szeged: Magyar Biofizikai Társ., 2017. p. 110. (ISBN:978-963-12-9447-7)*

127. **Szívós J**, Serényi M, Pothorszky S, Deák A, Vértesy G, Sáfrán G: "A technique for nanopatterning diverse materials", *Surface and Coatings Technology 313: pp.115-120. (2017)*

128. **Szolnoki A**, Chen X: "Alliance formation with exclusion in the spatial public goods game", *Phys Rev E-Stat Nonlin 95:(5) Paper 052316. 8 p. (2017)*

129. **Szolnoki A**, Perc M: "Second-Order Free-Riding on Antisocial Punishment Restores the Effectiveness of Prosocial Punishment", *Phys Rev X 7: Paper 041027. 11 p. (2017)*

130. **Takács M**, Dücső Cs, Pap AE: "Nano-structured WO_3 layers sensitized with ALD Pt for quick detection of H_2S", *J Mater Sci Mater Electronics 28:(22) pp.17148-17155. (2017)*

131. **Takahashi S**, Kobayashi S, Tomás I, Dupre L, Vértesy G: "Comparison of magnetic nondestructive methods applied for inspection of steel degradation", *NDT E International 91: pp.54-60. (2017)*

132. **Tapajna M**, Stoklas R, Gregusová D, Gucmann F, Huseková K, Hascík S, Fröhlich K, Tóth Laa, Pécz B, Brunner F, Kuzmík J: "Investigation of 'surface donors' in Al_2O_3/AlGaN/GaN metal-oxide-semiconductor heterostructures: Correlation of electrical, structural, and chemical properties", *Appl Surf Sci 426: pp.656-661. (2017)*

133. **Tapajna M**, Válik L, Gucmann F, Gregusová D, Fröhlich K, Hascík S, Dobrocka E, Tóth Laa, Pécz B, Kuzmík J: "Low-temperature atomic layer deposition-grown Al_2O_3 gate dielectric for GaN/AlGaN/ GaN MOS HEMTs: Impact of deposition conditions on interface state density", *J Vacuum Science and Technology B-Nanotechnology and Microelectronics 35:(1) Paper 01A107. 8 p. (2017)*

134. **Tapasztó O**, Balko J, Puchy V, Kun P, Dobrik G, Fogarassy Zs, Horváth ZE, Dusza J, Balázsi K, Balázsi Cs, Tapasztó L: "Highly wear-resistant and low-friction Si_3N_4 composites by addition of graphene nanoplatelets approaching the 2D limit", *Scientific Reports 7:(1) Paper 10087. 8 p. (2017)*

135. **Tóth AB**, Holczer E, Hakkel O, Tóth EL, Kristóf I, Fürjes P: "Modelling and Characterisation of Droplet Generation and Trapping in Cell Analytical Two-Phase Microfluidic System", In: *Jean-Paul Viricelle, Christophe Pijolat, Mathilde Rieu (Eds.) Eurosensors 2017. Paris, France, 2017.09.03-2017.09.06. MDPI AG, Paper 526. 4 p.14*

136. **Udvardi P**, Radó J, Straszner A, Ferencz J, Hajnal Z, Soleimani S, Schneider M, Schmid U, Révész P, Volk J: "Spiral-Shaped Piezoelectric MEMS Cantilever Array for Fully Implantable Hearing Systems", *Micromachines 8:(10) Paper 311. 13 p. (2017)*

137. **Vancsó P**, Hagymási I, Tapasztó L: "A magnetic phase-transition graphene transistor with tunable spin polarization", *2D Materials 4:(2) Paper 024008. 16 p. (2017)*

138. **Vértesy G**, Balassa P, Gasparics A, Tomás I, Mészáros I: "Inspection of diesel engine injectors by several electromagnetic nondestructive methods", *Int J Appl Electromagnetics and Mechanics 54:(3) pp.449-459. (2017)*

139. **Vértesy G**, Bálint B, Bingler A, Gyimóthy Sz, Bilicz S, Pávó J: "Simulation of magnetic flux distribution for the measurement of the local thinning of ferromagnetic plates", *Int J Appl Electromagnetics and Mechanics 57: pp.597-612. (2017)*

140. **Vértesy G**, Uchimoto T, Takagi T, Tomás I, Kage H: "Graphite structure and magnetic parameters of flake graphite cast iron", *J Magnetism and Magnetic Materials 442: pp.397-402. (2017)*

141. **Weiszburg TG**, Gherdan K, Ratter K, Zajzon N, Bendo Z, Radnóczi Gy, Takács A, Véczi T, Varga G, Szakmány G: "Medieval Gilding Technology of Historical Metal Threads Revealed by Electron Optical and Micro-Raman Spectroscopic Study of Focused Ion Beam-Milled Cross Sections", *Analytical Chemistry 89:(20) pp.10753-10760. (2017)*

142. **Zátonyi A**, Borhegyi Z, Cserpán D, Somogyvári Z, Srivastava M, Kisvárday Z, Fekete Z: "Optical Imaging of Intrinsic Neural Signals and Simultaneous MicroECoG Recording Using Polyimide Implants", *Proceedings 1: Paper 610. 4 p. (2017)*